Generation of emulsion droplets and micro-bubbles in microfluidic devices

Thesis by

Jiaming Zhang

In Partial Fulfillment of the Requirements

For the Degree of

Doctor of Philosophy

King Abdullah University of Science and Technology, Thuwal,

Kingdom of Saudi Arabia

April, 2016

The thesis of Jiaming Zhang is approved by the examination committee

Committee Chairperson: Mohammed Younis

Committee Member: Sigurdur Thoroddsen

Committee Member: Khaled Salama

Committee Member: Michael Breadmore

ABSTRACT

Generation of emulsion droplets and micro-bubbles in microfluidic devices

Jiaming Zhang

Droplet-based microfluidic devices have become a preferred versatile platform for various fields in physics, chemistry and biology to manipulate small amounts of liquid samples. In addition to microdroplets, microbubbles are also needed for various processes in the food, healthcare and cosmetic industries. Polydimethylsiloxane (PDMS) soft lithography, the mainstay for fabricating microfluidic devices, usually requires the usage of expensive apparatus and a complex manufacturing procedure. In addition, current methods have the limited capabilities for fabrication of microfluidic devices within three dimensional (3D) structures. Novel methods for fabrication of droplet-based microfluidic devices for the generation microdroplets and microbubbles are therefore of great interest in current research.

In this thesis, we have developed several simple, rapid and low-cost methods for fabrication of microfluidic devices, especially for generation of microdroplets and microbubbles. We first report an inexpensive full-glass microfluidic devices with assembly of glass capillaries, for generating monodisperse multiple emulsions. Different types of devices have been designed and tested and the experimental results demonstrated the robust capability of preparing monodisperse single, double, triple and multi-component emulsions.

Second, we propose a similar full-glass device for generation of microbubbles, but with assembly of a much smaller nozzle of a glass capillary. Highly monodisperse microbubbles with diameter range from 3.5 to 60 microns have been successfully produced, at rates up to 40 kHz. A simple scaling law based on the capillary number and liquid-to-gas flow rate ratio, successfully predicts the bubble size.

Recently, the emergent 3D printing technology provides an attractive fabrication technique, due to its simplicity and low cost. A handful of studies have already demonstrated droplet production through 3D-printed microfluidic devices. However, two-dimensional (2D) flow structures are still used and the advantage of 3D-printing technique has not been fully exploited. Therefore, we apply 3D printing technology to fabricate 3D-miniaturized fluidic device for droplet generation (single emulsion) and droplet-in-droplet (double emulsion) without the need for surface wettability treatment of the channel walls, by utilizing 3D geometry design and fabrication. A scaling law is formulated to predict the drop size generated in the device. Furthermore, magnetically responsive microspheres are also produced with our emulsion templates, demonstrating the potential applications of this 3D emulsion generator in chemical and material engineering.

Finally, we design and 3D-print a hybrid "plug-and-play" microfluidic droplet generator, which involves a 3D-printed channel chamber and commercial tubings and fittings. By combination of 3D-printed part and market-available parts, this device can be easily assembled and disassembled, which provides a great flexibility for different demands. A scaling law has been proposed for prediction of drop size generated in the device. Furthermore, a 3D-printed concentration gradient generator and a droplet merging device based on the droplet generator have been developed to demonstrate the great scalability of 3D-printing technology.

ACKNOWLEDGEMENTS

Fist and foremost, I would like to express my deepest thanks and appreciation to my advisor, Prof. Sigurdur Thoroddsen, for his support and guidance on my research. I am grateful to him for his patience, encouragement and suggestions throughout my PhD studies. His enthusiasm and diligence as a scientific researcher inspire me a lot to do the research.

The research in my thesis is supported by KAUST's baseline funding, which also provided me cherish opportunities to attend several international conferences.

I appreciate that research stuff in core lab and microfluidics lab offer valuable advice and support for my research.

I also thank the whole group in High-speed imaging fluids lab to support me during my PhD studies.

Finally, I would like to thank my family for their love, support and encouragement.

TABLE OF CONTENTS

LIST OF FIGURES

LIST OF TABLES

Chapter 1

Introduction

1.1 Droplet-based Microfluidics

Microfluidics is the science and technology of systems that process or manipulate small amount of fluids in a confined channel systems with dimensions on the order of tens to hundreds of microns [1]. Microfluidic technology has been continuously growing due to its large potential in scientific research as well as in chemical, biological and medical applications [2, 3, 4, 5]. This multidisciplinary technology involves fundamental concepts in a broad range of fields from physics to bioscience.

One of the most important subcategory of microfluidics is droplet-based microfluidics [6, 7]. Droplet-based microfluidics involves the generation and manipulation of discrete droplets inside microfluidic devices. This application can produce highly monodisperse droplets with nanoliter volume, at rates of up to tens of thousands per second [8].

Due to the size reduction in microfluidics, the surface area to volume ratio becomes larger and thus surface related physics dominate over the volumetric phenomena. This specialty has offered new approaches to conducting research and fabrication which is not possible to accomplished at macroscale. For example, several reaction parameters in microreactors based on droplets can be controlled independently on the small scale including quantity of reagents [9], mixing rate [10] and residence time [11]. In addition,

independent control of each droplet is allowed in this technology, thus the results from droplet microreactors can be individually analyzed [12, 13]. Resulting from the high frequency of generation, large data sets can be acquired very efficiently. Together with the inherent low material consumption required, droplet-based microfluidics enables high-throughput screening of chemical and biological libraries [14, 15, 16].

Thanks to a lot of beneficial uses of microparticles based on droplet-based microfluidics, synthesis of such engineer particles based on this technology, has undergone rapid development of use in various fields, including polymer particles [17, 18], microcapsules [19, 20], nanoparticles [21, 22], quantum dots [23, 24], *etc.*

In recent years, an impressing success of droplet-based microfluidics is the generation of multiple emulsions [25]. Multiple emulsions can provide a highly-controlled and complex emulsion-based templates utilized for the formation of functional microparticles for encapsulation or controlled-release applications such as drug delivery [26].

All of above applications are based on droplet-based microfluidics, which originates from the droplet generation. So a variety of research and studies are being conducted for producing stable microfluidic droplet generators, which will be more fully introduced in the next section.

1.2 Microdroplet Generation Methods

1.2.1 Conventional Methods

There are several conventional methods for droplet generation utilized in industry. Briefly, conventional emulsification techniques apply high-shear forces to break up immiscible liquids to produce emulsions in a big container with various valves and rotor-stator dispersing machines (stirring vessel, colloid mills, toothed disc dispersing machine, etc.) [27, 28, 29]. These methods require large viscous stresses and high

mechanical energy. Using these methods, it is difficult to guarantee narrow droplet size distribution because of large variation in the strength of the shear stress occuring in a turbulent flow. The drop size distribution can be measured by their coefficient of variation (C_v), which is defined as the ratio between standard deviation (δ) and mean diameter (d_{av}) as depicted in eqn 1.1. If the variation of the drop sizes is small ($C_v < 5\%$), the droplet generated can be said to be monodisperse [30]. Using the above conventional methods, droplet sizes are generated in the range of 0.1 to 100 μm diameter, usually with a wide size distribution ($C_v \sim 30\%$).

$$C_v = \delta / d_{av} \times 100\% \tag{1.1}$$

1.2.2 Alternative Methods

Membrane emulsification techniques were developed after the conventional methods [31, 32, 33]. The disperse phase is driven through a porous membrane with controllable pore size to enter into the continuous phase. The final droplet size depends on membrane pore characteristics (pore size, pore distribution, porosity and surface conditions), surfactant choice and fluid viscosity. The droplet sizes are generated in the range of 0.1 to 100 μm diameter, with a smaller size variation ($C_v \sim 10\% - 20\%$) [34], compared to the conventional methods.

A similar method as membrane emulsification, named microchannel emulsification was later reported [35, 36]. It replaces the porous membrane with microgrooves. The disperse phase is driven through these grooves into the continuous phase. The droplet size mainly depends on the microchannel dimensions, and is not affected by the continuous flow rate. Thus droplets with narrow size range can be produced, with the C_v reduced to below 5%.

Recently another variation of microchannel emulsification technique was proposed [37], through which monodisperse droplets can be produced. The generation of

droplets mainly depends on geometry constriction of microchannel, not affected by fluid flow. Therefore, droplet formation is relatively slow.

Ink-jet printing is another technique to produce emulsions [38]. Monodisperse droplets can be generated using this technique, but it requires additional devices such as piezo-driven nozzles, printing head and pulse generator, therefore it increases the whole system complexity which hinders its application in engineering or lab use.

1.2.3 Microfluidic Methods

In the last decade, new microfluidic methods have emerged to generate emulsions [39]. Compared to aforementioned methods, microfluidic techniques have several significant advantages. They can produce droplets with high degree of monodispersity ($C_v < 5\%$) and at high frequency ($\sim 10^4 s^{-1}$). It also has added the benefits of allowing further manipulation of the individual droplets such as merging [40, 41], sorting [42, 43], screening [44, 45], *etc.* Thus using microfluidic devices, it is much easier for researchers to integrate subsequent multi-functional analysis after generation of droplets. This allows fabricate a complete functional chip for commercial use.

First, planar microfluidic droplet generators were developed. T-junctions and flow-focusing structures are the two primary types of flow structures reported for droplet production. T-junction structures are shown in Fig. 1.1(a, b) for producing droplets and were first introduced due to their simplicity [46, 47, 48, 49, 50, 51]. Both shear stresses generated by the continuous phase and pressure difference of emerging droplets cause the tip of the disperse phase to stretch into the main channel before pinch-off of the disperse phase happens [52]. The modified T-junction as shown in Fig. 1.1(b) was reported later by Wang *et al.* [53]. They insert a capillary into the T-junction to form droplets and bubbles, where the depth of the capillary inserted can be tuned so more shear force can be acquired due to the increase of local flow velocity in the gap. During the same period, cross junction structure as shown in

Fig. 1.1(c) was utilized to produce droplets [54, 55]. The disperse phase breaks into droplets when its jet becomes too thin to persist in the continuous phase. If two different liquids are injected into the two opposite inlets, cross junction can produce droplets with alternating composition as shown in Fig. 1.1(d) [56, 57]. Steegmans *et al.*[58] used Y-junction, as shown in Fig. 1.1(e) to produce droplets. The disperse phase flow rate and viscosity have no influence on droplet size in Y-junction, which is different from T-junction.

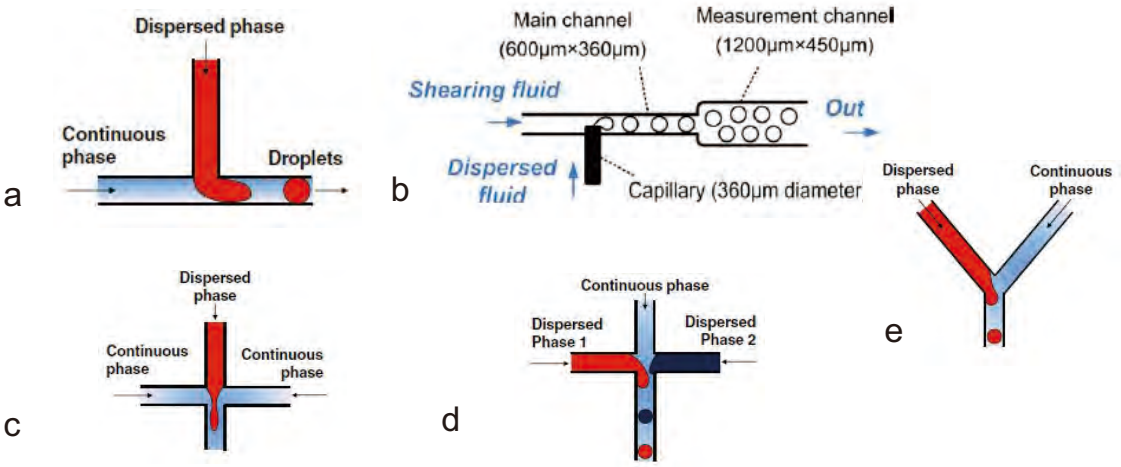

Figure 1.1: Various structures for generating droplets in microchannels [34]. (a) T-junction [46]. (b) Modified T-junction [53]. (c) Cross-junction [55]. (d) Cross-junction with alternating droplets [57]. (e) Y-junction [58].

Standard flow focusing structures were first introduced by Anna *et al.*[59] as depicted in Fig. 1.2(a). The disperse phase is injected into the middle channel while the continuous phase is injected into two side channels. The continuous phase introduces pressure and shear forces that make the disperse phase form a narrow thread, which then breaks into droplets downstream of the orifice. Afterwards, several researchers modified the geometry of flow-focusing structure as shown in Fig. 1.2(b), others investigated the mechanism of drop formation in this type of structure and realize a variety of applications by using such flow-focusing devices [60, 61, 62, 63, 64].

Secondly, three-dimensional axisymmetric microfluidic devices for drop formation

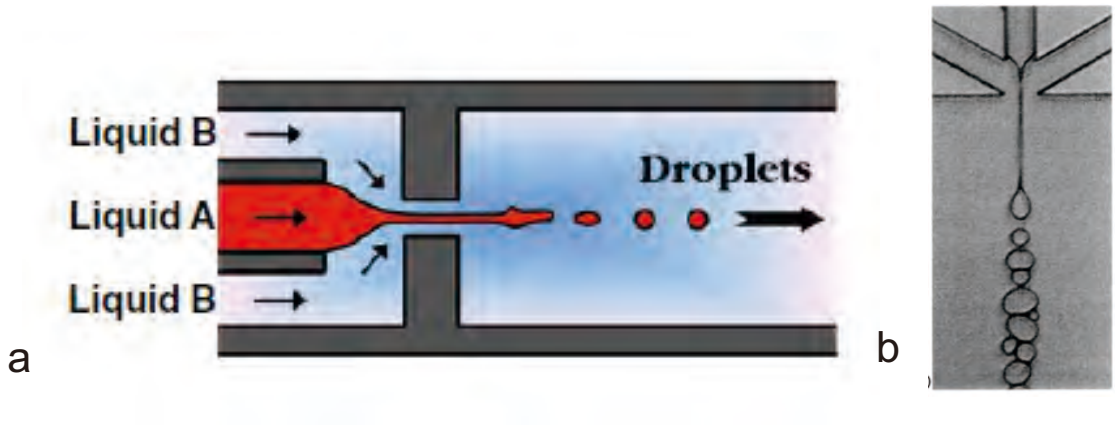

Figure 1.2: Flow-focusing structures. (a) Standard flow-focusing structure [34]. (b) Modified flow-focusing structure [53].

are attracting researchers more and more researchers' attention instead of planar microfluidic devices. This is important because in planar microfluidic devices, droplets inevitably contact the channel walls, which may lead to breakup of droplets when they touch and wet or stick to the walls [65]. While in an axisymmetric microfluidic devices, the disperse phase is completely surrounded by the continuous phase. Therefore, the disperse phase does not have a chance to contact any of the channel walls so that the droplet breakup or wetting problems are suppressed.

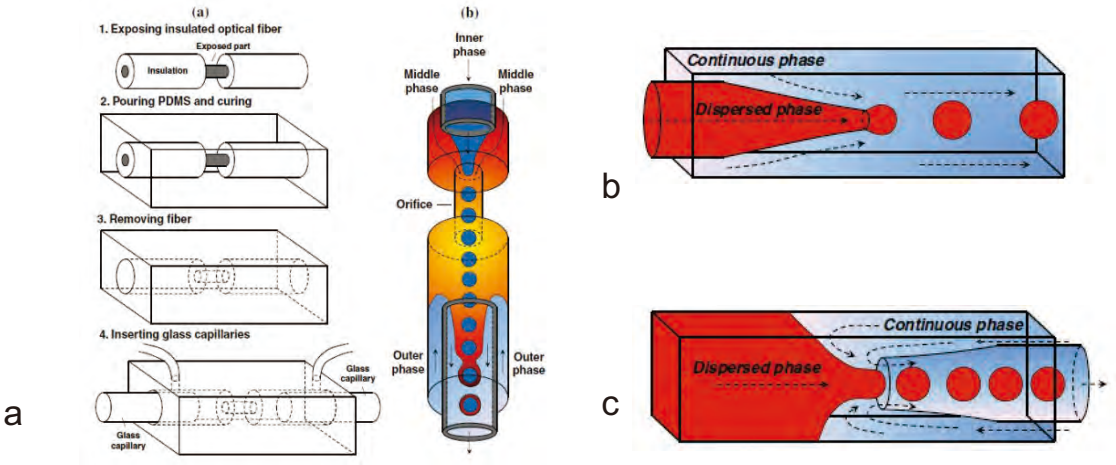

Figure 1.3: Three dimensional microfluidic devices taken from Ref. [34] (a) Circular channel fabricated by PDMS [65]. (b) Co-flow regime glass capillary microfluidic device [66]. (c) Flow-focusing regime glass capillary microfluidic device [67].

Several researchers first used Polydimethylsiloxane (PDMS) to fabricate an ax-

isymmetric flow focusing microfluidic device based on a three-dimensional templates as shown in Fig. 1.3(a) [65, 68, 69]. Later, glass capillary axisymmetric devices were invented and widely used. Compared to PDMS, glass is more chemically robust, does not swell, and can easily be surface treated to change its wettability [34]. It is more convenient and suitable for further applications to use axisymmetric glass capillary devices. There are two main flow structures, *i.e.* co-flow and flow focusing, used in such glass capillary axisymmetric devices. In co-flow regime as shown in Fig. 1.3(b), both the disperse phase and continuous phase flow in the same direction [66, 70, 71]. On the other hand, in the flow focusing regime, as shown in Fig. 1.3(c), the disperse phase flows from one direction and the continuous phase flows from the opposite direction. Then, both of them flow into the collection capillary and the disperse phase breaks into droplets in the collection capillary [67]. The benefit of flow focusing regime is that it can generate droplets with diameter smaller than the size of orifice.

1.3 Microbubble Generation Methods

Microbubbles are commonly used in medicine and pharmacuticals as carries of drugs and genes to thermally ablate tumors [72, 73], as building blocks for hierarchical materials with versatile functionalities [74], and as biosensors [75]. In addition, massive amounts of microbubbles are also needed in the food, healthcare and cosmetics industries [76].

One of the most important applications of microbubbles is as ultrasound contrast agents (UCAs) for ultrasound imaging. Ultrasound pulses are typically applied with a frequency near the resonance frequency of the microbubble and the microbubbles increase and decreases in diameter, producing strong echoes from regions of perfused tissue [77]. Ultrasound pulses with different frequency, phase and amplitude are analyzed to separate microbubble and tissue echoes, which will enhance the image

quality. Diameters of microbubbles should lie between 3 and 8 μm so that they can safely pass the smallest human capillaries. Highly polydisperse size distribution of microbubbles will increase the range of resonance frequencies, which will reduce the sensitivity of the imaging system [78]. Therefore, highly monodisperse microbubbles smaller than 10 μm are preferred and in great demand.

1.3.1 Conventional Methods

Conventional methods for producing microbubbles include sonication [79, 80] and high shear emulsification [81, 82]. Regarding to sonication method, the size of microbubbles depends on the frequency, power and pulse regime of the ultrasound. For high shear emulsification, researchers emulsify the polymer in an aqueous suspension by high shear stirring. The size distribution of microbubbles obtained by these two methods is quite broad and thus they require additional filtration process for removing larger bubbles which can result in an embolism [83].

An alternative way to produce microbubbles is membrane emulsification [83, 84]. Continuous gas phase as disperse phase is pressure-driven through the membrane to form microbubbles under the crossflow introduced by the continuous phase. The microbubble size strongly depends on the characteristics of the membrane (pore size distribution, wettability etc.) [31]. It is quite difficult to produce microbubbles with diameter less than 10 μm by using membrane emulsification method.

1.3.2 Microfluidic Methods

In recent years, microfluidic methods have been developed to produce microbubbles. The great benefits obtained by using microfluidic devices is that it can generate highly monodisperse microbubbles, which is very important for medical application such as ultra sonic imaging where microbubbles are used as contrast agents. The monodisperse microbubbles can provide better reflection signals. Monodispersity is also im-

portant for bubbles acting as carriers for drug delivery where highly monodisperse microbubbles can carry accurate dosage of drugs for patients.

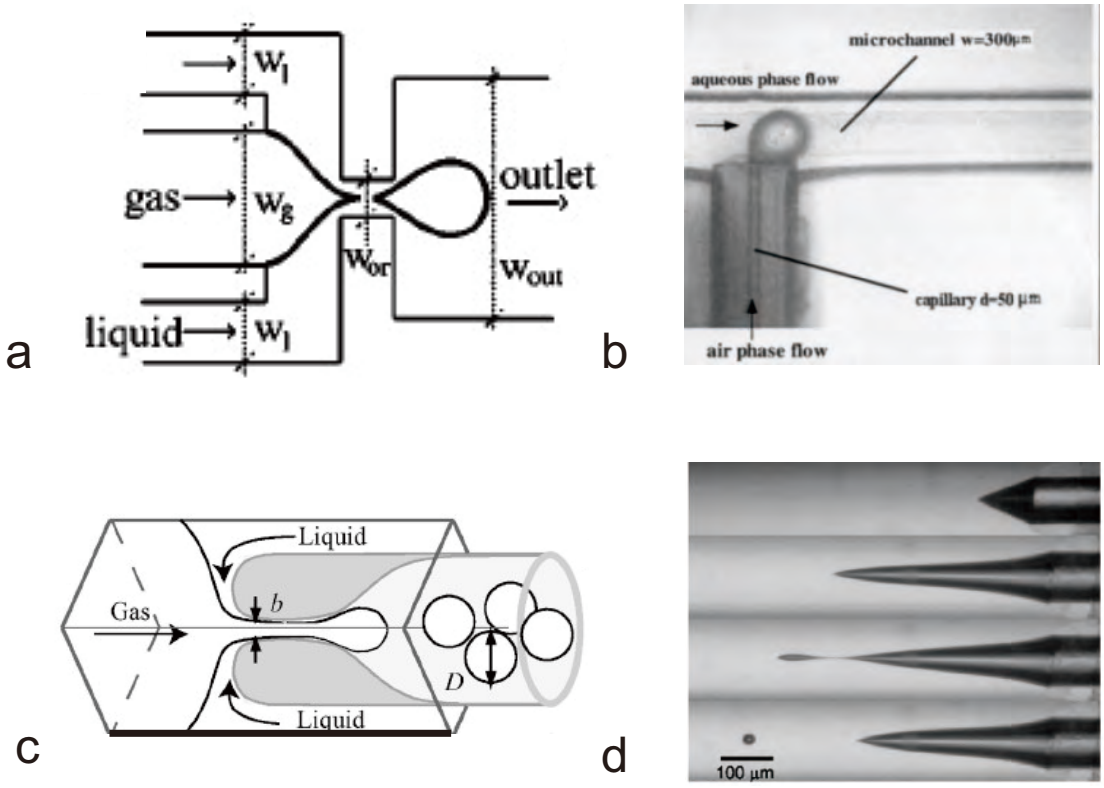

Figure 1.4: Various structures for generating microbubbles. (a) Flow-focusing structure [85]. (b) T-junction [86]. (c) Flow-focusing regime in glass capillary device [87]. (d) Co-flow regime in glass capillary device [88].

Similar to droplet generation, there are also two primary types of designs for microbubble generation: flow-focusing structure and T-junction. Here researchers replace the liquid disperse phase with gas phase for production of microbubbles. Planar flow focusing microfluidic devices as shown in Fig. 1.4(a) were first applied for generating monodisperse microbubbles [89, 85, 90, 91, 92]. The gas phase flows into the inner channel and the continuous phase flows into the outer channel. They flow together through an orifice and then the gas phase breaks into microbubbles at the orifice.

T-junction as shown in Fig. 1.4(b) is another common method used for producing

microbubbles [93, 86, 94] due to its simplicity. The gas phase injected into the side channel breaks into microbubbles in the main channel in which the continuous phase flows into. The generation of microbubbles below 10 μm has not yet been reported using T-junction.

Other than planar microfluidic devices, researchers have also started to make use of glass capillaries to get a three-dimensional axisymmetric microfluidic device for generating microbubbles. Lorenceau *et al.*[87] melted a cylindrical glass capillary to form a constricted structure as shown in Fig. 1.4(c). The inner gas phase is squeezed by outer liquid and then breaks into microbubbles. The disadvantage of this design is that liquids and gases flow through the restricted part, making it prone to blockage by dirt in the liquid phase. Ganan-Calvo *et al.*[95] used capillary together with a narrow orifice to generate monodisperse microbubbles. Lee *et al.*[96] uses three glass capillaries (injection capillary, collection capillary and outer capillary) to form nanoparticle-shelled microbubbles. Several researchers have arranged two coaxial cylindrical glass capillaries together as shown in Fig. 1.4(d) to construct a co-flow scheme for generating microbubbles [97, 88]. However, the generation of microbubbles with diameter less than 10 μm has not yet been reported using such glass capillary methods.

1.4 Fabrication Technique for Droplet-based Microfluidic Devices

A variety of methods have been reported for the fabrication of microfluidic devices. The choice of fabrication method is determined by several factors, such as availability of specialized fabrication equipment, cost, time requirements, feature size, and the preferred material substrate. The most common methods used for microfluidic devices will be introduced in the following subsections.

1.4.1 Micromachining of Silicon and Glass

Early microfluidic devices were fabricated using chip manufacturing techniques, which come from the semiconductor industry. These techniques mainly involve the use of wet and dry etching silicon [98, 99] and glass [100, 101]. Glass devices are still widely used in microfluidics due to the well-understood fabrication techniques, as well as for the beneficial optical properties, surface chemical stability, and solvent compatibility [102].

1.4.2 Soft Lithography

The term "soft lithography" was defined by Whitesides and coworkers [103], which refers to various techniques that encompass replica molding using an elastomeric material, specifically polydimethylsiloxane (PDMS), to fabricate microfluidic devices. The common procedure of this technique is shown in Fig. 1.5, consisting of the following steps: (1) Deposit photoresists such as SU-8 on the silicon wafer. (2) Expose the coating photoresists with ultraviolet (UV) light through a mask with desired pattern to obtain the master. (3) Pour PDMS with curing agent onto the master and keep the PDMS in an oven at 60°C for approximately 2 hours to cure the PDMS and transfer the channel pattern to the PDMS. (4) Bond PDMS replica with other substrates such as glass or another piece of PDMS to enclose channels.

1.4.3 Hot Embossing

Hot embossing is a technique using thermoplastic materials, typically flat sheets, which are patterned against a master using pressure and heat [104]. Thermoplastic will be reshaped when they are heated near the glass transition temperature of the material. Materials typically used include polymethylmethacrylate (PMMA), polycarbonate (PC), cyclic olefin copolymer (COC), polystyrene (PS), polyvinylchloride

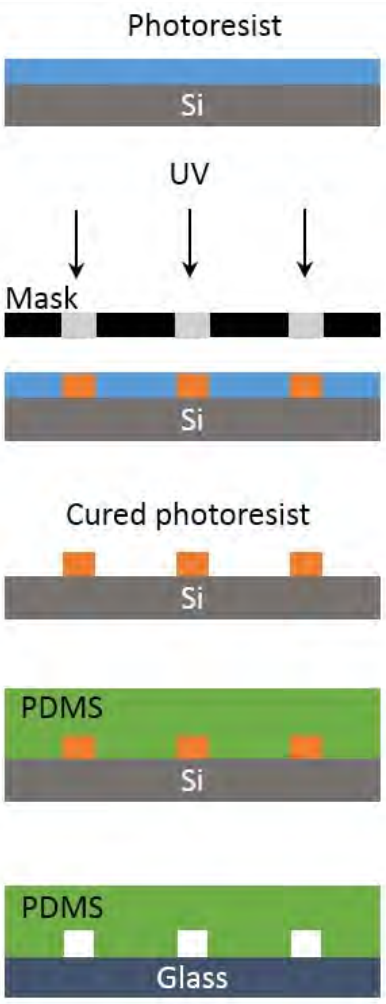

Figure 1.5: Soft lithography process for fabricating PDMS microchannels.

(PVC), and polyethyleneterephthalateglycol (PETG). Masters are usually made in either silicon or metal. The master and the thermoplastic are placed into a hydraulic press with heat and pressure. Then the pattern sheet is enclosed with another piece of thermoplastic.

1.4.4 Laser Ablation

Laser ablation involves the use of a high-powered pulsed laser to remove materials from a sheet of thermoplastic since most plastics absorb UV light [105]. Common plastics used for laser ablation include PMMA, PETG, PVC, PC and polyethyleneterephth-

thalate (PET). A pulse energy of a few hundred mJ can usually ablate approximately 0.5 μm of the material. The depth of channel also depends on the pulse rate and the absorption of the material. The width of channel mainly depends on the laser focusing optics. Recently, CO_2 lasers, with wavelengths in the infrared region, were also reported to be used for fabrication [106], typically with PMMA and PET substrates.

All the above fabrication methods summarized are currently widely used to fabricate microfluidic devices, which primarily produce planar microfluidic devices. With the rapid development of three-dimensional (3D) fabrication technique such as 3D printing technology, such systems have caught researchers attention that such methods could be utilized to fabricate 3D structure microfluidic devices. More details of 3D printing technology will be introduced in the next section.

1.5 3D Printing Technology

3D printing, also known as additive manufacturing or rapid prototyping, was first introduced in the 1980s [107]. 3D printer usually interprets a standard tessellation language (.STL) to print 3D objects. The .STL file stored the geometry information of the design, which is usually sliced into a certain number of two-dimensional (2D) sequential cross-sectional slices, depending on the resolution of the printer. Then the 3D object is printed in an additive, consecutive manner from these 2D cross-sectional slices until the whole 3D object is completed. The .STL format is usually converted into from the 3D model which is created using computer aided design software (CAD).

There are three primary types of 3D printing systems used for microfluidics fabrication: fused deposition modeling (FDM), stereolithography (SLA), and polyjet printing. Other 3D printing systems, such as selective laser sintering (SLS) and laminated object manufacturing (LOM) are not the main concern in this thesis, which will not be introduced in detail.

1.5.1 Fused Deposition Modeling (FDM)

FDM is one of the cheapest 3D printing technologies due to its simple mechanics of the printer and the low cost of the raw build materials. Therefore, FDM printers are widely used as personal desktop printers on the current market. FDM is based on the extrusion of melted bulk material through a heated nozzle [108], as seen in Fig. 1.6, The nozzle moves in the horizontal plane according to the design and semi-molten plastic is deposited on the stage and solidifies. The stage then moves down in the z-direction for the deposition of next layer. This process is repeated until the whole 3D object is completed. Due to the nature of the printing process, the resolution achievable is limited by the nozzle/stage stepper motor, the thickness of the filament, and the extrusion nozzle diameter. So the resolution of FDM technique is not as fin as that of other 3D printing technique. Available FDM printers on the market usually provide a resolution of in 250 μm XY and 50 μm in the Z direction. Furthermore, FDM printers have the ability of printing objects in many colors/materials by usage of multiple extrusion nozzles. Common materials used in the FDM process include acrylonitrile butadiene styrene (ABS), polylactic acid (PLA), and nylon.

1.5.2 Stereolithography (SLA)

SLA was invented by Chuck Hull in the 1980s [107]. As shown in Fig. 1.7, a UV laser is utilized to scan and trace over a certain pattern in a horizontal area to cure the photopolymer resin. The resin is hardened after being cured and the platform moves down in the z-direction for the next layer. A sweeping blade recoats the next layer of resin over the cross section of the object, which is then ready for laser scan of the next layer. This process is repeated until the whole object is completed. A variety of curing methods have been developed for use within commercially available SLA instruments, including laser raster scanning, laser vector scanning, and digital light processing (DLP) [109]. Early SLA printers mainly adopted the laser raster scanning

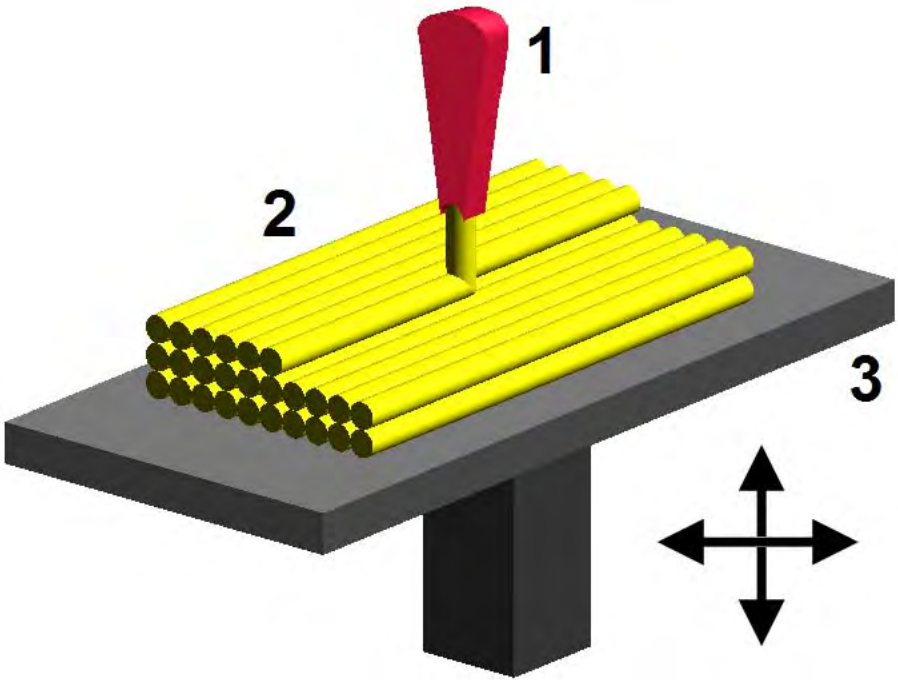

Figure 1.6: Schematic of FDM printing [108].

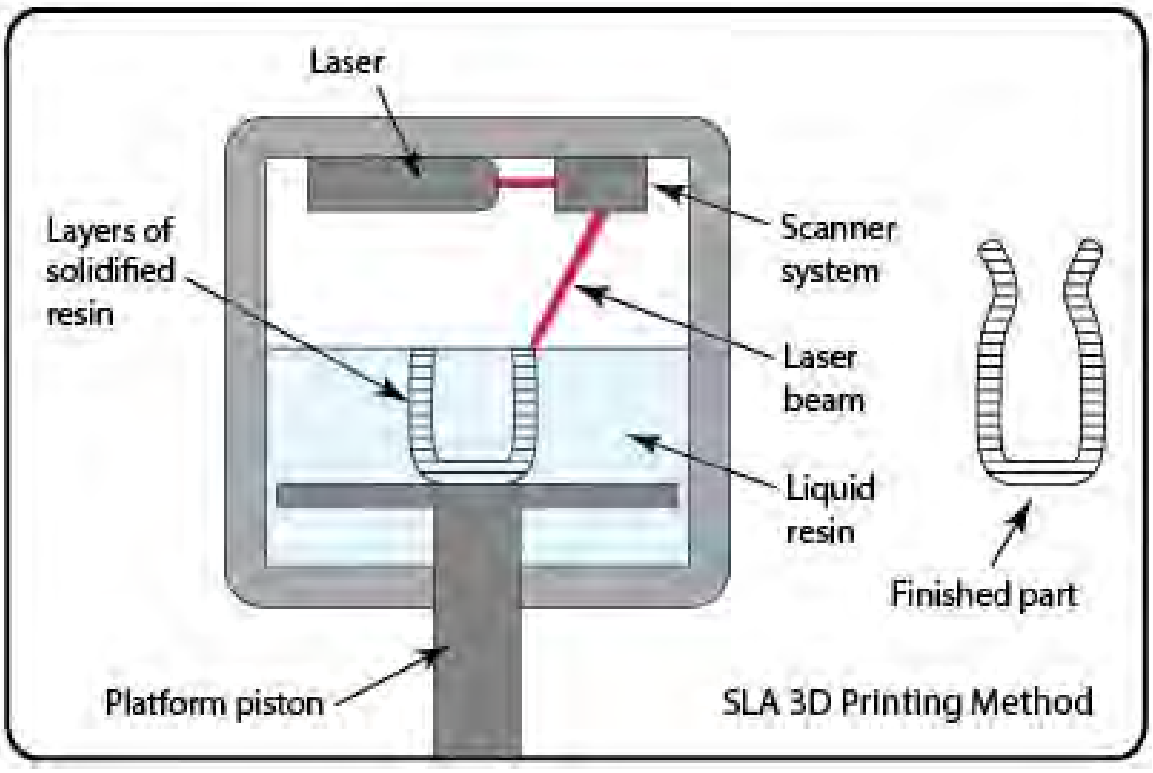

Figure 1.7: Schematic of SLA printing [107].

strategy. Later, the appearance of galvanometer-based vector scanning for the laser allowed for faster curing of resins and a reduction of the production times, which results in making SLA systems highly commercialized and the most widely used type of 3D printing machines [110].

Recently, digital projection systems (DLP) were developed which allow for curing one layer in one step, as shown in Fig. 1.8. These systems usually have a controllable digital mirror which can reflect the laser light in an entire plane. The printer based on this digital mirror device (DMD) print objects according to the images [111]. The .STL file is sliced and converted into a certain number of bitmap images which are black and white. When the image is projected onto the resin, only the white part can be exposed and cured. Once one layer is cured, the platform moves up in z-direction for the next layer curing. This process is repeated until the whole object is completed. Compared to the SLA process, DLP or DMD adapt a mask projection for curing a single layer in one step, which greatly reduces the production time.

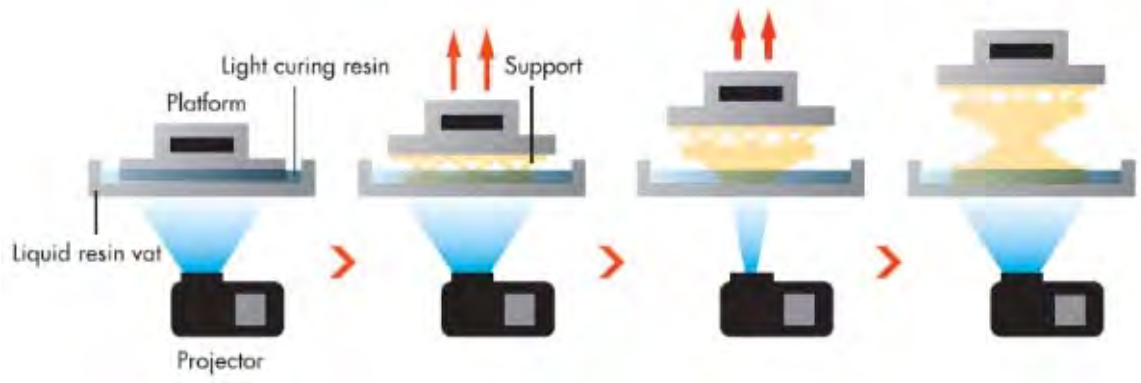

Figure 1.8: Schematic of DLP printing [111].

A major advantage of SLA fabrication is the high precision of the surface resolution, due to the process of photo-curable resin exposed by a UV laser. This makes SLA a particularly good candidate for fabrication of microfluidic devices since a smooth channel surface is crucial for the liquid flowing regularly inside the microchannel.

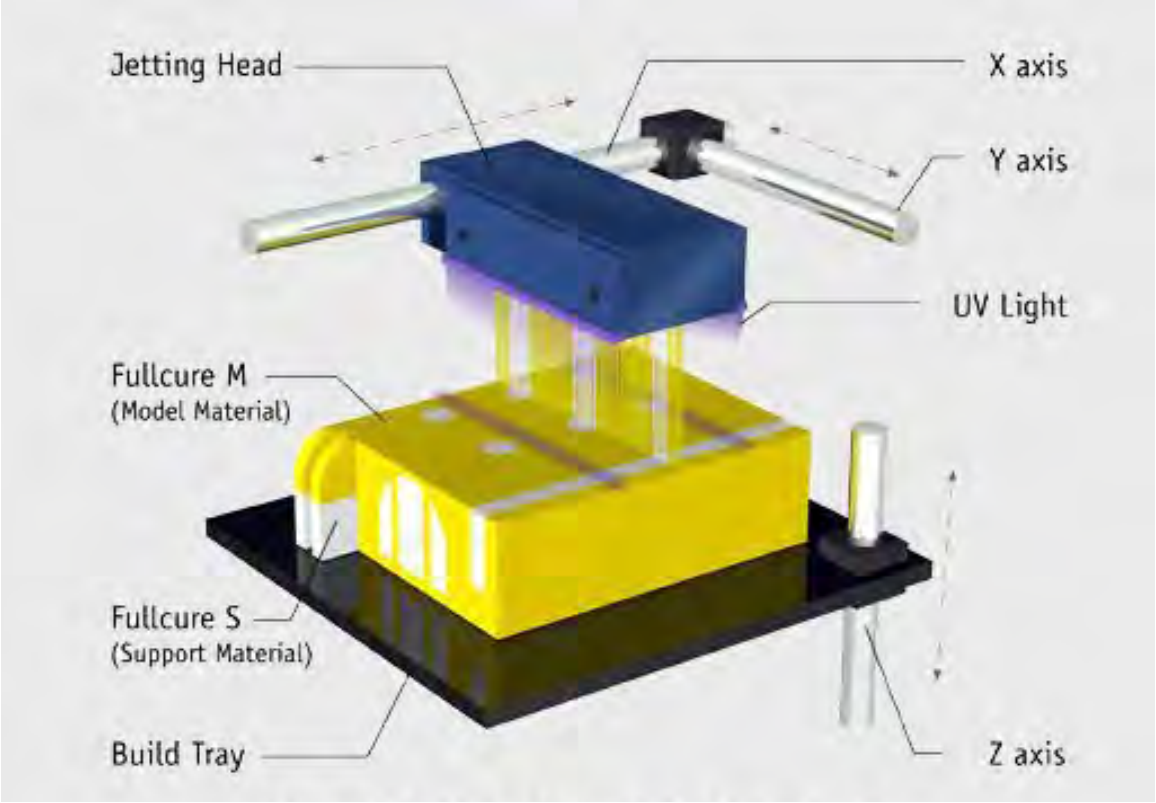

Figure 1.9: Schematic of polyjet printing [112].

1.5.3 Polyjet Printing

This technique is similar to the mechanics of a commercial inkjet printer, except that photopolymer resin or wax is jetted out instead of ink [112]. As shown in Fig. 1.9, the resin is jetted through a jetting head onto the platform and then is cured by UV light attached to the jetting head. Once one layer is cured, the platform moves down in the z-direction for the next layer curing. For models containing a void space such as the microchannels, the printer deposits support material to fill in the void space first. Then the support material can be removed by physical or chemical methods after the whole printing process is completed. The major advantages of this technique include high quality and resolution, fast printing speed and the ability of incorporating multiple materials to print. But for channel printing, the channel surface quality is limited due to incomplete removal of the support materials.

1.6 Dimensionless Numbers In Microfluidics

A wide variety of physical phenomena occur in microfluidic devices, the importance of which must be determined by comparing them against competing phenomena. Dimensionless numbers expressing the ratio of the forces associated with each of the physical phenomena give a sense for where a system sits in fluidic parameter space. Several dimensionless numbers related to the multiphase flow in droplet-based microfluidics are discussed here.

The Reynolds number (Re):

$$Re = \frac{\rho U D}{\mu} \tag{1.2}$$

where U and D are the characteristic velocity and length scale; ρ and μ are density and dynamic viscosity of the liquids, respectively. Re relates the importance of inertial forces with respect to viscous forces. Since the characteristic length scale in microfluidics is small ($\sim \mu$m), $Re < 1$. Viscous forces are usually dominant in microfluidics.

The capillary number (Ca):

$$Ca = \frac{\mu U}{\sigma} \tag{1.3}$$

with σ the interfacial tension between different liquid phases. Ca relates viscous forces to surface tension or interfacial tension forces. Since the characteristic velocity in microfluidics is small ($\sim$cm/s), $Ca < 1$. Interfacial tension forces are usually dominant in microfluidics which is the main difference from macrophysics: Surface related physics is important in microfluidics.

The capillary length (l_c):

$$l_c = \sqrt{\frac{\sigma}{\triangle\rho \times g}} \tag{1.4}$$

with $\triangle\rho$ the density difference between two phases and g the gravity acceleration. l_c identifies the droplet size where capillary effects to gravity effects are similar, and

Table 1.1: Comparison of the microfluidic device fabrication techniques

	Soft-lithography	Hot embossing/molding	Laser ablation	3D printing
Setup cost	$\sim$ \$ 80K	$>$ \$ 50K	$\sim$ \$ 20K	\$ 1K-20K
Material cost/per chip	High	Low	Low	Medium
Time-consuming/per chip	$\sim$ 1 week	$\sim$ 1 week	$\sim$ 1 day	1-2 hrs
3D capability	Poor	Poor	Poor	Excellent
Flexibility	Poor	Poor	Poor	Excellent
Throughput	Low	High	Medium	Medium
Manufacturability	Poor	Poor	Poor	Excellent

the length above which gravity effects dominate capillary effects. l_c is usually an order of $\sim$ mm depending on the liquids used in microfluidics, whereas the droplet size created and the channel dimensions in microfluidics are an order of 10^{-1} or 10^{-2} mm. Therefore, gravity usually does not influence the process of droplet generation, deformation and transportation in microfluidic devices.

1.7 Current Challenges and Research Objectives

Although there are a variety of fabrication methods for microfluidic devices, the process of fabrication is still relatively complicated and also the cost of the fabrication is still high, which hinder extension of microfluidics applications. The comparison of current fabrication techniques is listed in table 1.1 [113]. Researchers are still working on developing new fabrication technology of microfluidic devices aimed at allowing more wide use and providing more complex functionality.

Our work aims at developing simple, rapid and low-cost fabrication techniques for droplet-based microfluidic devices. We then demonstrate the feasibility of droplet or bubble generation in these novel devices. Scaling laws for prediction of droplet and microbubble sizes in our devices are also proposed and verified. This will help users to design microfluidic devices to produce droplets or microbubbles according to their individual requirements. Furthermore, some functional particles have been synthesized based on our droplet templates to demonstrate great potentials of droplet

microfluidics in engineering applications.

Chapter-2 and chapter-3 propose a new design and method based on current fabrication technique for generation of multiple emulsions and microbubbles. Chapter-4 and chapter-5 apply a new fabrication technique (3D printing) for fabrication of microfluidic devices for emulsion generation.

Chapter 2

Simple and inexpensive microfluidic devices for the generation of monodisperse multiple emulsions

2.1 Introduction

In chapter-1, we have reviewed the microfluidic methods for generation of droplets (single emulsion). In recent years, multiple emulsion generation techniques have become a hot topic in scientific research because it can provide an excellent platform for chemistry, bioscience, and medical applications. Two-step T-junction was first applied for producing double emulsions as shown in Fig. 2.1a [114, 115]. Two T-junctions are fabricated in series with different surface wettabilities. Later, two types of flow focusing structures were introduced for generation of double emulsions, as shown in Fig. 2.1b and Fig 2.1c. One is that the disperse phase is composed of two different immiscible fluids, which are squeezed by outer continuous phase to form double emulsion [116]. The other is that two flow focusing structures are fabricated in

series with different surface wettabilities [117]. Later on, consecutive cross junctions with different surface wettabilities were applied for producing double emulsion in one step or in two steps as shown in Fig. 2.1d and Fig. 2.1e [118, 119].

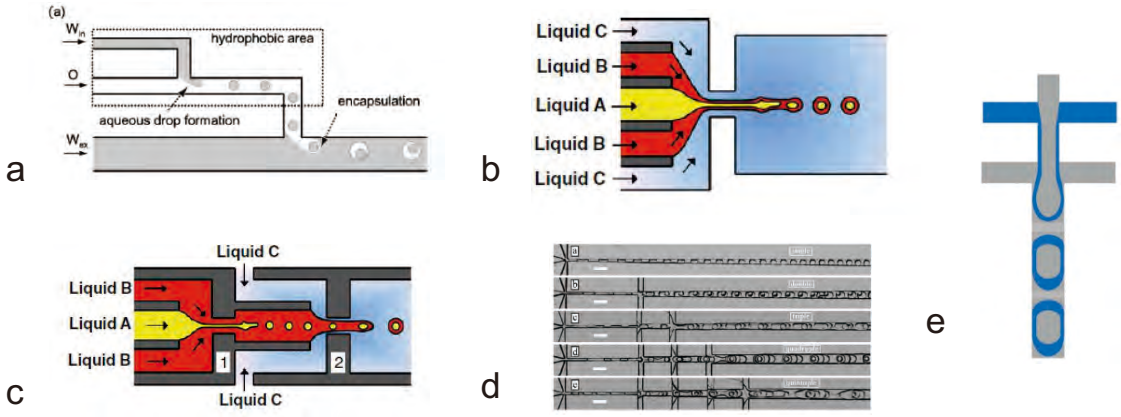

Figure 2.1: Multiple emulsions generated in planar microfluidic devices. (a) Double T-junctions [114]. (b) One-step double emulsion in flow-focusing structure [34]. (c) Two steps double emulsion in flow-focusing structure [34]. (d) Multi-step multiple emulsion in cross-junction structure [118]. (e) One-step double emulsion in cross-junction structure [119].

Recently, microfluidic devices based on axisymmetric glass capillaries show their diverse possibility in producing multiple emulsions. For these devices, the glass capillaries are pulled in a micro-pipette puller, where electric heater or laser melt the glass while pulling apart. First, they can generate core/shell droplets by carefully arranging three glass capillaries as shown in Fig. 2.2a [120, 121, 122, 123]. Two capillaries are arranged end-to-end as injection and collection within the same outer capillary. Secondly, it can generate multiple emulsions with a controlled number of inner drops as shown in Fig. 2.2b [124, 125]. The only change is that the injection capillary is inserted into a transition capillary. The transition capillary is also tapered and is inserted into a collection capillary. These three capillaries are all arranged inside an outer square capillary. One to seven inner drops inside the larger drops can be produced by this method. Higher-order emulsions can also be produced by adding another transition capillary. In addition, this setup can generate multiple emulsions

of inner drops with different compositions as shown in Fig. 2.2c [24, 126, 127]. The only difference from previous structures lies in that the injection capillary is replaced by a capillary with separate circular channels where different liquid components can flow in parallel.

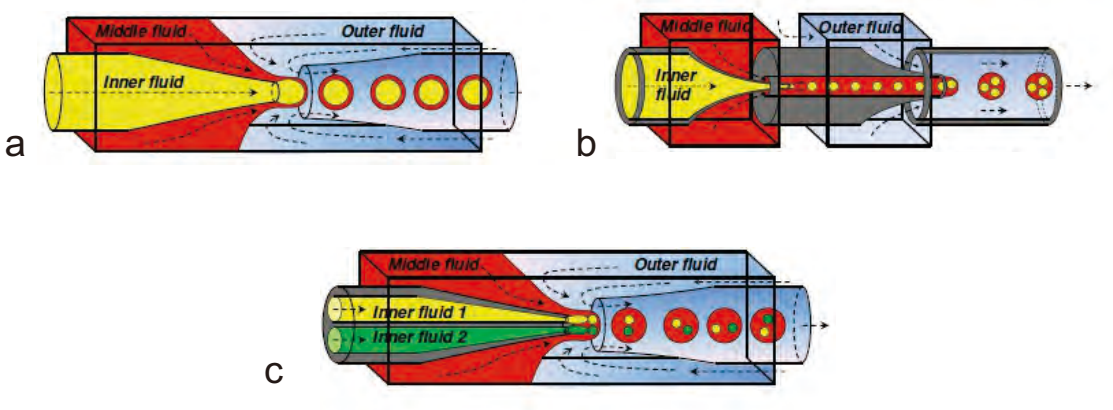

Figure 2.2: Multiple emulsions in glass capillary microfluidic devices [34]. (a) One-step double emulsion. (b) Multi-step double emulsion. (c) Multi-component emulsion.

Herein we report a design of this nature. It is a simple and inexpensive microfluidic device which is easy to align,and is based on microscope glass slides and glass capillaries. It can generate monodisperse single, double, triple and multi-component emulsions. The advantages of our approach lie in a simple fabrication and assembly process and no need for expensive fabrication equipment. This approach uses one tapered cylindrical glass capillary and four microscope slides to fabricate all-glass microfluidic devices that are capable of producing monodisperse double emulsion droplets of water-in-oil-in-water (W/O/W) or (O/W/O) phases. Triple emulsion droplets of water-in-oil-in-water-in-oil (W/O/W/O) or (O/W/O/W) phases also have been stably generated by adding a second cylindrical capillary next to the outlet of the first capillary. By carefully controlling the wettability of the inner surface of the first capillary outlet, multi-component emulsion droplets of (gas and water)-in-oil-in-water ((G+W)/O/W) phases can be stably produced. The relationship between the number and sizes of encapsulated droplets, and the flow parameters, has been

successfully modeled.

2.2 Methods

2.2.1 Fabrication of the microfluidic device

The microfluidic devices were designed and fabricated based on microscope glass slides and glass capillaries. The whole fabrication process is depicted in Fig. 4.1. Firstly, all the glass slides and capillaries were cleaned in an ultrasonic bath of acetone, isopropanol and ethanol in ten minute sequences. Then two glass slides (76.2 mm $\times$ 25.4 mm, thickness of 1 mm; or 60 mm $\times$ 24 mm, thickness of 150 μm) were fixed onto a bigger microscope glass slide (75 mm $\times$ 50 mm, thickness of 1 mm) by double-sided tape (Scotch permanent double sided tape), to form a channel. The double-sided tape should be spread onto the glass slides to avoid leaving air bubbles under the tape. It is also helpful to put the bonded slides under a weight ($\sim$ 0.2 kg/cm^2) for 30 minutes. A glass capillary is used as a baffle between these two glass slides, providing the channel with a desired width that equals to the OD of the capillary. Glass capillaries were heated and pulled by a micro-capillary puller (P-1000, Sutter Instrument), to form tapered ends with desired orifice sizes. The length of the pulled capillary can be controlled from 15 to 50 mm. The surface wettability modification of the capillaries and the channel was also carried out in this step. Commercial coating agent (FluoroPel PFC 801A, Cytonix Corporation; or Glaco Mirror Coat 'Zero', Soft 99 Co.) was used as the water repellent agent and the details of the treatment will be described in the section of "Results and discussion". Secondly, the tapered capillaries were bonded into the channel in a designed arrangement with epoxy (HP 250, ITW Devcon, Inc.). This both fixes them in place and separates the flow of the various liquids by forming an impenetrable barrier. Finally, a plexiglass or glass slide (76.2 mm $\times$ 25.4 mm, thickness of 1 mm), working as the cover of the microfluidic device,

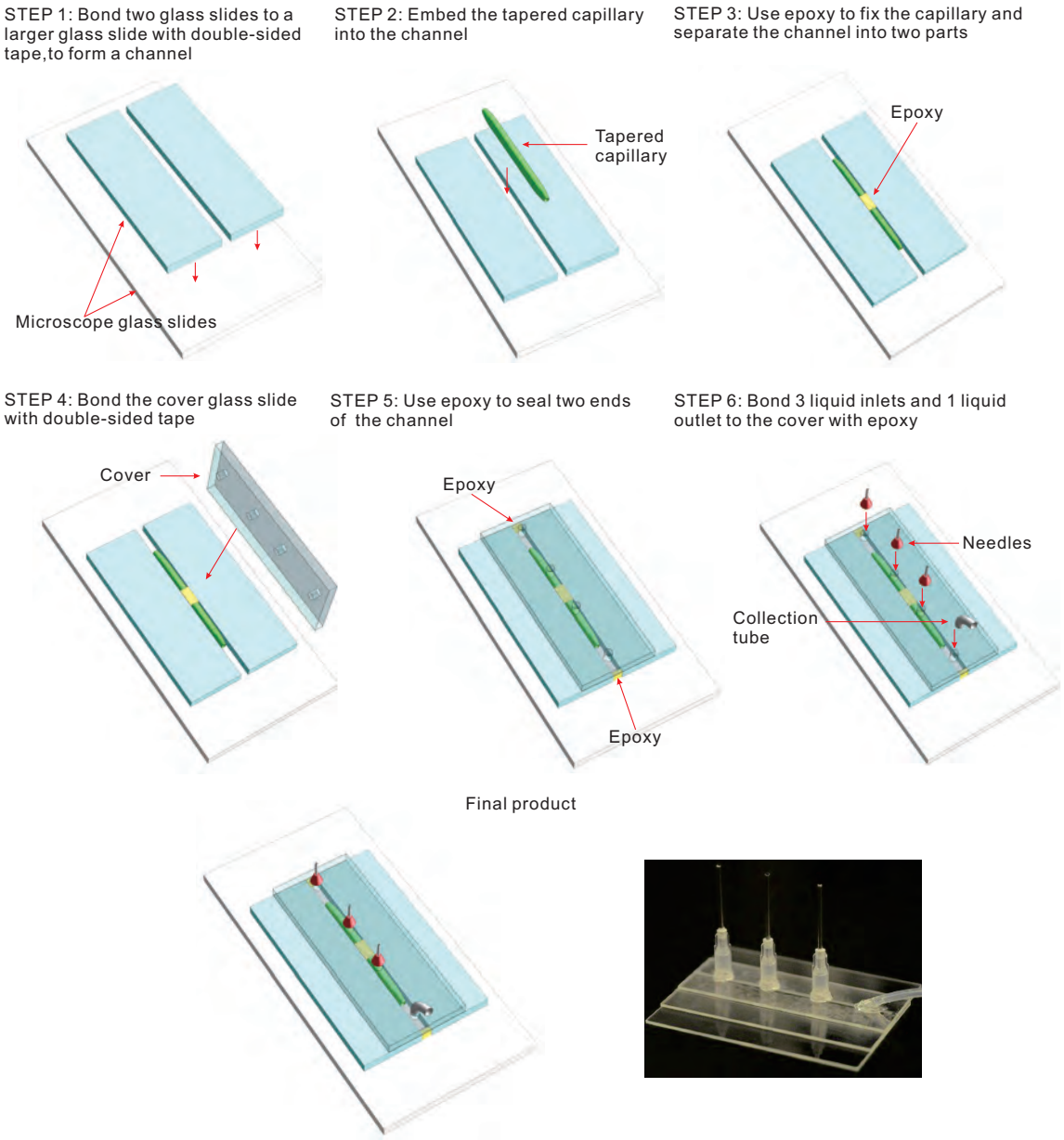

Figure 2.3: A schematic illustration of the fabrication of a microfluidic device based on microscope glass slides and a glass capillary. Step 1: Side walls are formed by bonding two glass slides onto a bigger glass platform, to form a channel. Step 2: The tapered capillary is embedded into the channel in the designated arrangement. Step 3: Epoxy is used to fix the capillary and separate the channel into two parts. Step 4: The cover glass slide is bonded on top of the channel, with double-sided tape. Step 5: Epoxy is used to seal the two ends of the channel. Step 6: Bond three liquid inlets and one liquid outlet (collection tube) attached to the cover with epoxy. The last two figures show a typical microfluidic device fabricated for preparing double emulsions. This device has three liquid inlets which are fed through separate syringe pumps.

was bonded onto the channel by double-sided tape. Syringe needles were bonded to the holes (1.7 mm in diameter) in the cover slide by epoxy, to form inlets and outlet. Diamond core drills (Eternal Tools) were used to fabricate liquid inlets and outlet when a glass cover was used.

The depth of the microchannels can be controlled from 290 μm to 1.2 mm, by using microscope glass slides with different thicknesses (1 mm for Cat. No. 12-544-1; 150 μm for Cat. No. 12-548-5P. Thermo Fisher Scientific Inc.) or even with stacked glass slides (the thickness of the double-sided tape is around 70 μm). The width of the microchannels can be controlled from 80 μm to 1 mm, by using glass capillaries (VitroCom, Inc.) with different OD, as the baffles.

This all-glass microfluidic device has good optical properties, chemical compatibility, as well as good mechanical strength. To prepare different kinds of emulsions mentioned earlier, six different types of microchannel designs have been tested. Each design and the corresponding surface treatment will be discussed individually in the following sections.

2.2.2 Microfluidic preparation of different monodisperse emulsions

Silicone oils (Sigma-Aldrich Corp.) of different viscosities were used as the oil phases, whereas glycerin aqueous solutions of different viscosities were used as the aqueous phases. Span 80 (Sigma-Aldrich Corp.) and Sodium dodecyl sulfate (SDS, Life Technologies Corp.) were used as lipophilic and hydrophilic surfactants respectively, and their concentrations were kept constant at 0.25% (v/v) and 0.25% (w/v), respectively. Up to four syringe pumps (Fusion 200, Chemyx, Inc.) were used for driving fluids into the microchannels. The formation process of the emulsion droplets was observed and recorded with a high-speed CMOS video camera Photron SA-5, or a SA-3 for color images. The camera was equipped with long-distance microscope objectives with

magnifications of 5, 10 and 20× (Mitutoyo Corporation). The elongated geometry allows frame rates up to ∼ 50 kfps (for SA-5, and 5 kfps for SA-3) at resolution of 128 × 1,024 pixel. Backlighting was accomplished with a 350 W metal-halide lamp (Sumita Optical Glass, Inc.), which was shone onto a diffuser. The size and size distribution of the emulsion droplets were analyzed using a Matlab program. All the experiments were carried out at room temperature (22 °C).

2.3 Results and discussion

2.3.1 Preparation of monodisperse W/O and O/W emulsions with a single tapered cylindrical glass capillary

Water-in-oil In the first step of the device fabrication process, after a channel was formed by fixing two glass slides onto a bigger microscope glass slide, 0.2 mL of commercial coating agent (FluoroPel PFC 801A, Cytonix Corporation; or Glaco Mirror Coat 'Zero', Soft 99 Co.) was dripped into the channel. The solution contains 99% of fluorosolvent and wets glass surfaces completely. Few seconds after the solution fully spread into the channel, the residue solution was removed by a forced air stream. A thin film then dries in minutes at room temperature to a surface energy of about 0.01 N/m, providing a uniform hydrophobic channel surface [128]. Similar process was also applied to the cover plate, while magic tape (Scotch) was used to protect the cover slide surface from contamination, by only leaving a strip (corresponding to the channel area) exposed to the PFC 801A solution. The tapered capillary was also dipped into the same PFC 801A solution for a few seconds, and cleaned by an air stream to remove any residual solution.

The above processes ensure that the surfaces of the channel, the outer and inner surfaces of the capillary are hydrophobic, as shown in Fig. 4.2(a). To generate monodisperse W/O emulsions, 50 cP (μ_I) water-glycerin solution containing

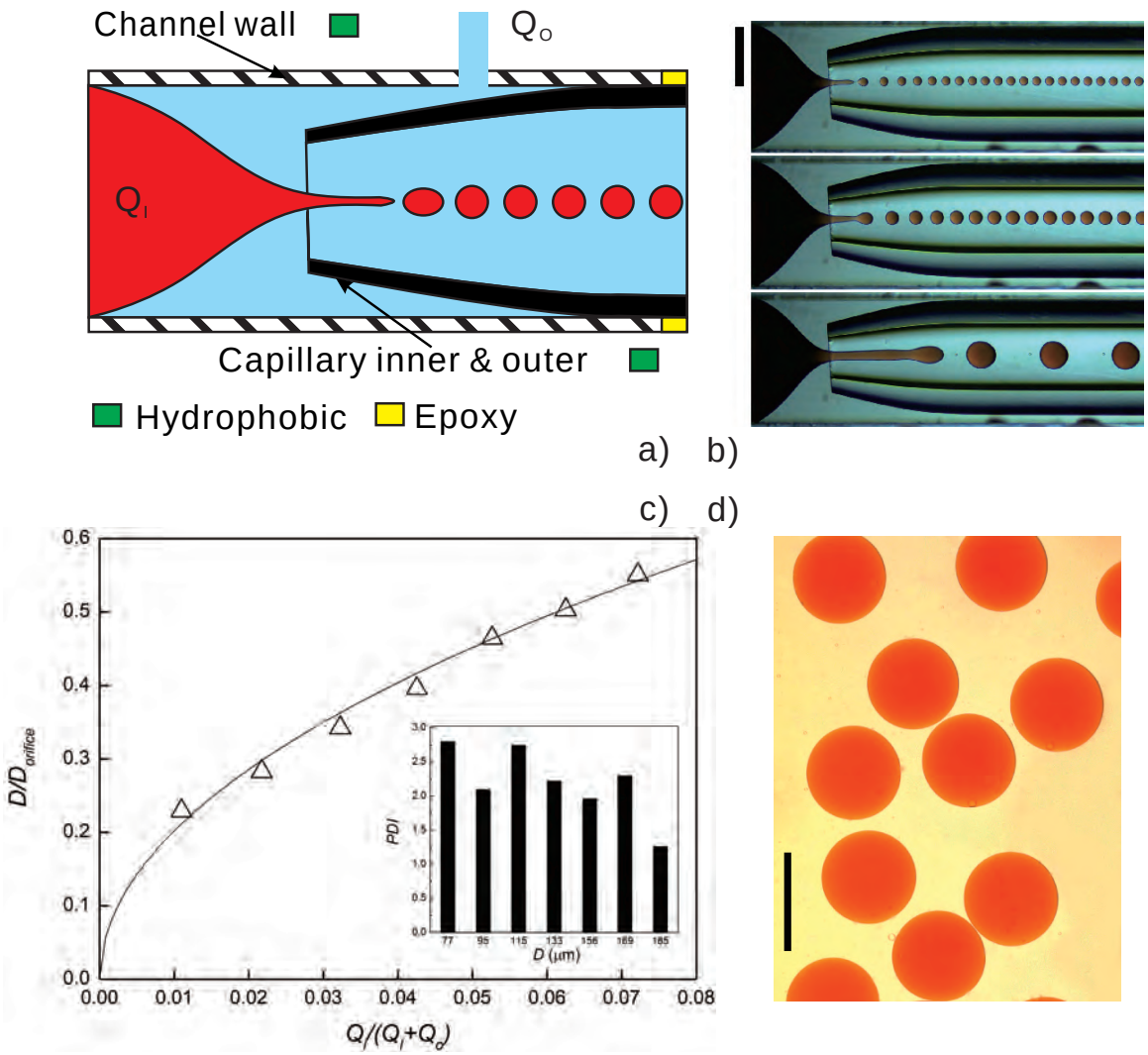

Figure 2.4: (a) Schematic of a flow-focusing microfluidic device for the formation of monodisperse W/O emulsions, in which, the dispersed phase is 50 cP water-glycerin solution (with 0.25% (w/v) SDS) and the continuous phase is 500 cSt silicone oil (with 0.25% (v/v) Span 80). (b) High-speed video frames of the generation of W/O emulsions with different flow rates, in which all the oil phase flow rates are 90 μL min^{-1}, and the aqueous phase flow rates are 1, 4 and 10 μL min^{-1} respectively, from top to bottom. Scale bar is 500 μm. (c) Experimentally measured droplet diameter D ($\triangle$) scaled by $D_{orifice}$ as a function of $Q_I/(Q_I+Q_O)$. The curve is the model prediction of eqn (2.3) with no adjustable constants. The inset shows the calculated PDI values. (d) Photomicrographs of the W/O emulsion. Scale bar is 250 μm.

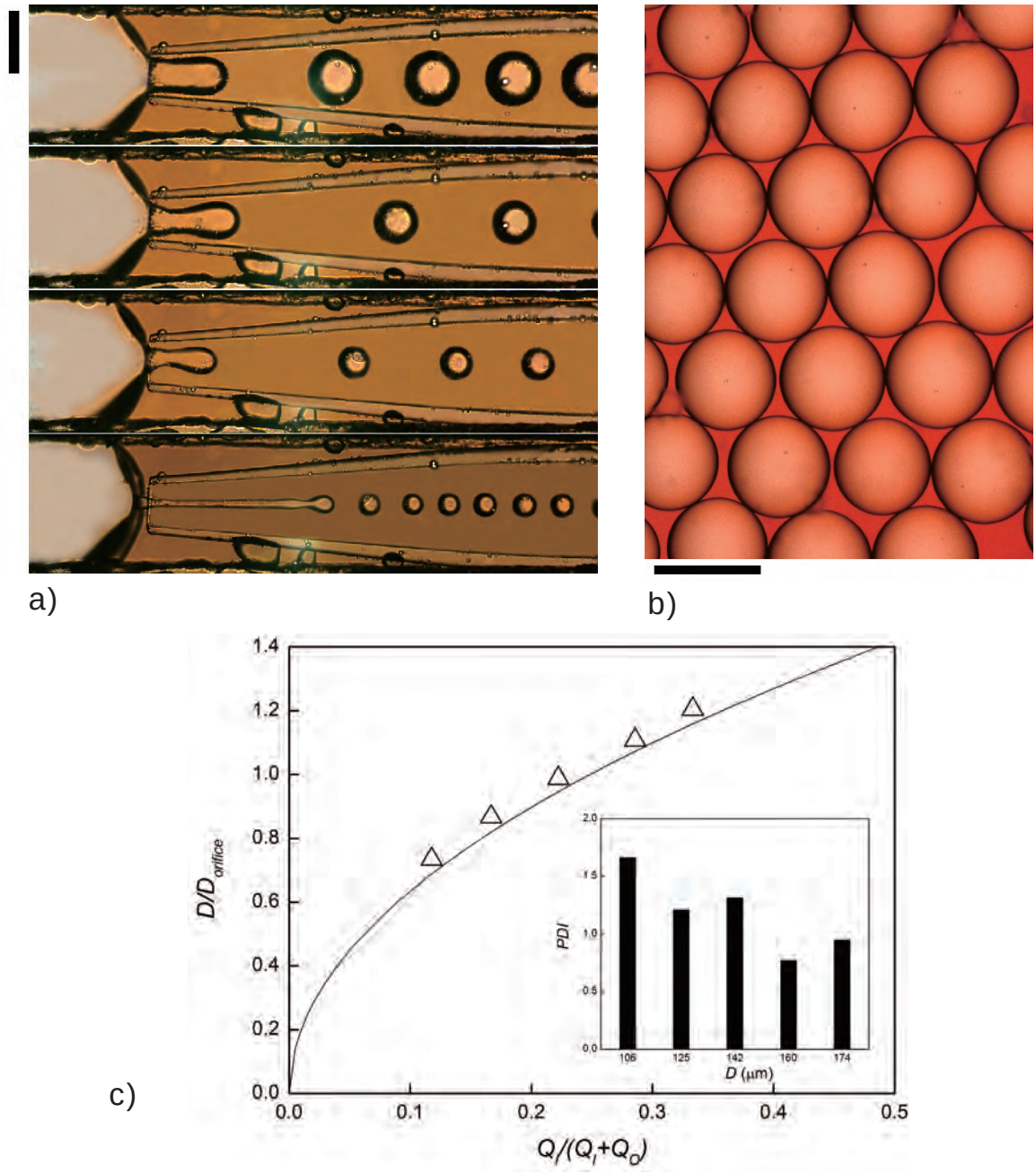

Figure 2.5: (a) High-speed video frames of the generation of O/W emulsions with different flow rates, in which all the oil phase flow rates are 2 μL min^{-1}, and the outer aqueous phase flow rates are 5, 7, 15 and 60 μL min^{-1}, from top to bottom. The dispersed phase is 20 cSt silicone oil (with 0.25% (v/v) Span 80) and the continuous phase is 100 cP water-glycerin solution (with 0.25% (w/v) SDS). (b) Photomicrographs of the O/W emulsion. (c) Experimentally measured droplet diameter D ($\triangle$) scaled by $D_{orifice}$ as a function of $Q_I/(Q_I + Q_O)$. The solid line represents the calculated results from eqn (2.3) with no adjustable constants. The inset in (c) shows the calculated PDI values. Both scale bars are 200 μm.

hydrophilic surfactant (0.25% (w/v) SDS) and 500 cSt (μ_O) silicone oil containing lipophilic surfactant (0.25% (v/v) Span 80) were used as disperse and continuous phases respectively, as shown in Fig. 4.2(b) The flow structure here is similar to that in a typical flow-focusing device [129, 130]. However, our device differs in that there is no injection tube for guiding the disperse fluid into the collection tube (the capillary in Fig. 4.2(b)). This focusing is accomplished by the flow itself. The location and shape of the interface (or the cap formed by the disperse phase) between disperse and continuous phases therefore are greatly affected by the flow parameters. As shown in Fig. 4.2(b), initial dripping occurs at low flow rates of the inner fluid Q_I and is characterized by the periodic formation of monodisperse droplets that form very close to the capillary inlet. Furthermore, the droplet sizes D increase with Q_I (first two images in Fig. 4.2(b)). With further increase of Q_I, a transition from dripping to jetting occurs and droplets are formed downstream (last image in figure 2(b)). Dripping is generally preferred as it leads to a more monodisperse size distribution. According to Utada *et al.* [25], in the dripping regime, mass flux is approximately proportional to cross-sectional area, which gives

$$\frac{Q_I}{Q_O} = \frac{\pi R_{jet}^2}{\pi R_{orifice}^2 - \pi R_{jet}^2} \tag{2.1}$$

where R_{jet} is the radius of the liquid thread measured near the capillary inlet, and $R_{orifice}$ is the inlet radius of the capillary orifice. Meanwhile, the droplet volume Ω, is approximately equal to $\pi R_{jet}^2 \lambda$, where λ is the wavelength of the fastest growing mode of the Rayleigh-Plateau instability, for a static liquid cylinder surrounded by another immiscible liquid. This λ is a function of viscosity ratio $\alpha = \mu_I/\mu_O$, and is expressed by $\lambda = kR_{jet}$ [131]. This gives

$$\Omega = \frac{4}{3}\pi \left(\frac{D}{2}\right)^3 = \pi R_{jet}^2 \lambda = k\pi R_{jet}^3 \tag{2.2}$$

Solving eqn (4.1) and (4.2) gives the normalized droplet diameter

$$\frac{D}{D_{orifice}} = \frac{1}{2}(6k)^{1/3}\left(\frac{Q_I}{Q_I + Q_O}\right)^{1/2} \tag{2.3}$$

Here the viscosity ratio is $\alpha = \mu_I/\mu_O = 0.10$, giving $k = 10.96$. (See Ref. [131]) Fig. 4.2(c) shows that this model (solid line) is in excellent agreement with the experimental data with no adjustable constants. Equation (2.3) shows that the droplet sizes D can be simply controlled by adjusting the flow rate ratios Q_O/Q_I and it can be used as a guideline for preparing emulsions with a desired size.

The size distribution of the produced water droplets can be expressed with the polydispersity index (PDI), which is defined as $\delta/d_{av} \times 100\%$, where δ is the standard deviation and d_{av} is the average water droplet size. For each fluid condition ($Q/(Q_I + Q_O)$), the PDI was calculated for over 200 droplets, and was drawn vs. the average droplet diameter, as shown in the inset in Fig. 4.2(c). As we can see, the PDI values are always below 3%, indicating highly monodisperse water droplet generation.

Oil-in-water To prepare O/W emulsions, hydrophilic surfaces are preferred. After being cleaned in an ultrasonic bath of acetone, isopropanol and ethanol in 10 minute sequences, all the glass slides were directly used to fabricate the microfluidic device. Then 20 cSt (μ_I) silicone oil containing lipophilic surfactant (0.25% (v/v) Span 80) and 100 cP (μ_O) water-glycerin solution with hydrophilic surfactant (0.25% (w/v) SDS) were used as disperse and continuous phases respectively to produce monodisperse O/W emulsions. Fig. 2.5(a) shows that in the dripping regime, droplets are highly monodisperse and droplet diameter D increases as the outer flow rate, Q_O, decreases. Dripping to jetting transition occurs when D becomes approximately equal to $2R_{jet}$ [132], which here corresponding to $Q_O/Q_I \approx 8$. Here $\alpha = \mu_I/\mu_O = 0.2$, giving $k = 10.78$ [131]. Again, we can use eqn (2.3) to calculate droplet diameter D in this dripping regime. Fig. 2.5(c) shows good agreement between the calculated results

(solid line) with the experimental data. Furthermore, the inset in Fig. 2.5(c) shows that the calculated *PDI* values are always below 2%, indicating highly monodisperse oil droplet generation. In the jetting regime, the droplets are not as monodisperse as that in the dripping regime.

2.3.2 Preparation of monodisperse W/O/W and O/W/O emulsions

As has been described above, the surface treatment for the microfluidic devices designed in this study was carried out before the combination of the main channel and the cover slide. This allows us to design devices with more flexibility in surface modification. To further demonstrate this flexibility, as well as the robustness of our microfluidic devices, W/O/W and O/W/O emulsions were also prepared here.

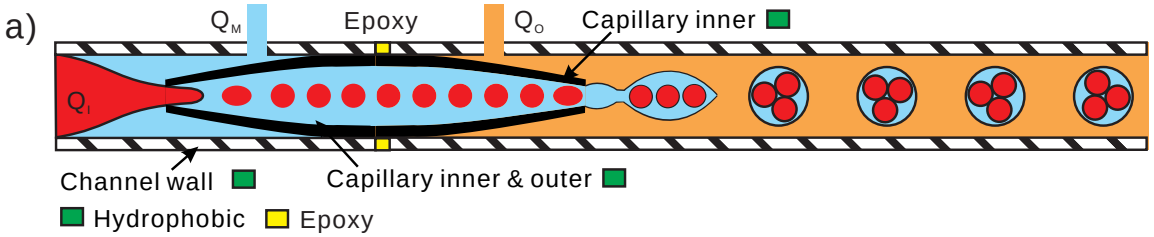
a)
Q_M
Epoxy
Q_O
Capillary inner
Q_I
Channel wall
Capillary inner & outer
Hydrophobic
Epoxy

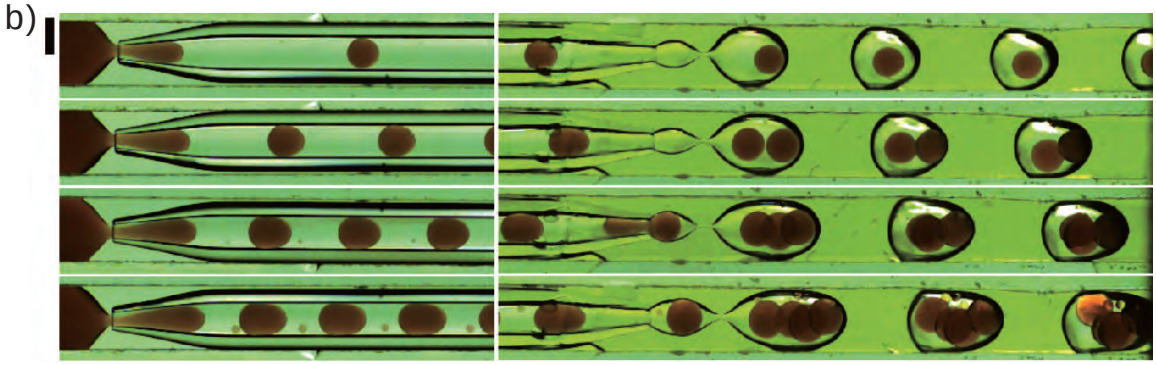
b)

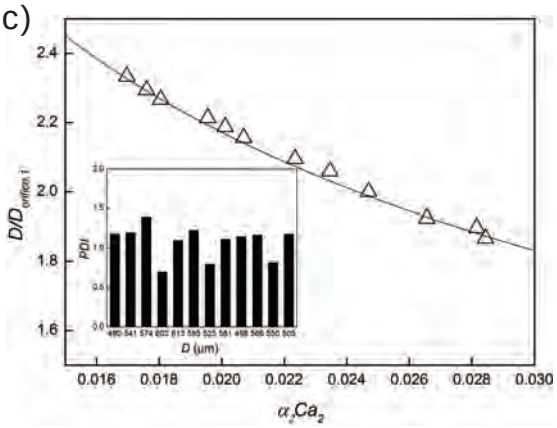
c)
$D/D_{orifice,1}$
PDI
D (μm)
$\alpha_2 Ca_2$

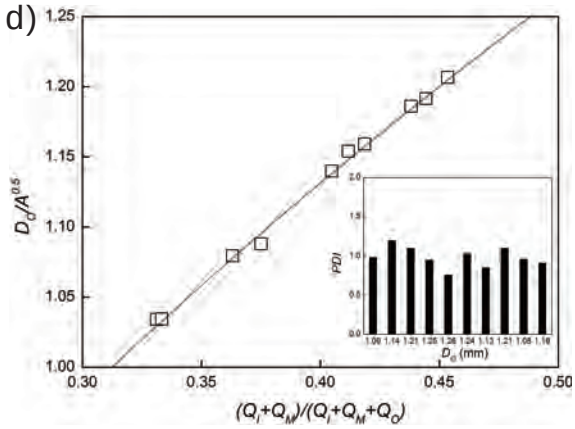
d)
$D_d/A^{0.5}$
PDI
D_d (mm)
$(Q_I+Q_M)/(Q_I+Q_M+Q_O)$

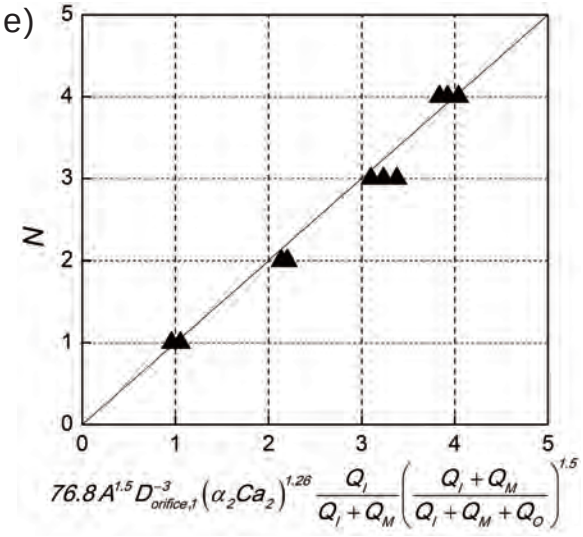
e)
N
$76.8A^{1.5}D_{orifice,1}^{-3}(\alpha_2 Ca_2)^{1.26}\frac{Q_I}{Q_I+Q_M}\left(\frac{Q_I+Q_M}{Q_I+Q_M+Q_O}\right)^{1.5}$

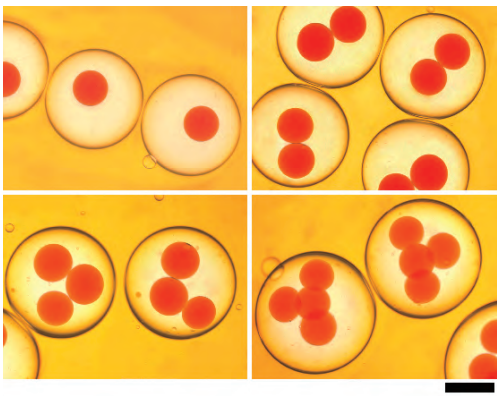
f)

Figure 2.6: (a) Schematic of a microfluidic device for the formation of monodisperse W/O/W emulsions, in which, the inner phase is 20 cP water-glycerin solution (with 0.25% (w/v) SDS), the middle phase is 100 cSt silicone oil (with 0.25% (v/v) Span 80) and the outer phase is 500 cP water-glycerin solution (with 0.25% (w/v) SDS). (b) High-speed video frames of the generation of W/O/W emulsions with different flow rates, in which the middle (Q_M) and outer (Q_O) phase flow rates are fixed as 45 and 100 μL min^{-1} respectively, while the inner flow rate (Q_I) varies as 4.5, 15, 25 and 35 μL min^{-1} from top to bottom. (c) Experimentally measured encapsulated droplet diameter D (Δ) scaled by $D_{orifice,1}$ as a function of $\alpha_2 Ca_2$. The solid line represents the calculated results from eqn (2.5). Inserted figure shows the calculated PDI values. (d) Experimentally measured double emulsion droplet diameter D_O($\square$) scaled by $A^{0.5}$ as a function of $(Q_I+Q_M)/(Q_I+Q_M+Q_O)$. The solid line represents the calculated results from eqn (2.7). The inset shows the calculated PDI values. (e) Comparison of predicted ($\blacktriangle$) and experimental measured number of encapsulated core droplets. (f) Photomicrographs of the W/O/W emulsion, in which the inner (Q_I) and middle (Q_M) phase flow rates are fixed as 4.5 and 45 μL min^{-1} respectively, while the outer phase flow rates (Q_O) are varying as 250, 125, 100 and 85 μL min^{-1}, respectively (left to right, top to bottom). Both scale bars are 500 μm.

Water-in-oil-in-water To prepare W/O/W emulsions with one tapered glass capillary (tapered at both ends), the device was designed as follows: monodisperse W/O single emulsion droplets were produced in the first flow-focusing section (inlet of the capillary) as described in previous section. Then these oil droplets were encapsulated by external aqueous phase in the second co-flow section (outlet of the capillary), forming monodisperse W/O/W double emulsions. The corresponding surface treatment of the device is marked in Fig. 2.6(a): the left half channel inner wall is hydrophobic while the right half is hydrophilic; the left half capillary outer surface is hydrophobic while the right half outer is hydrophilic; the whole capillary inner surface is hydrophobic. For the channel inner wall, this surface modification was achieved by dripping one drop of epoxy at the location corresponding to the center of the capillary, thereby splitting it in half. Then 0.2 mL of FluoroPel PFC 801A solution (or Glaco Mirror Coat) was dripped into the left half of the channel to make it hydrophobic, while the right half was kept hydrophilic. For the capillary, this surface modification was achieved by dipping half of the capillary into the PFC 801A solution, so only down-

stream half of the capillary outer surface will become hydrophobic. Due to capillary rise, the PFC 801A solution will climb along the capillary inner wall and make the whole capillary inner surface hydrophobic. After drying of the PFC 801A solution (in minutes), the capillary was bonded into the channel in the designed arrangement. When the epoxy goes dry, it then separates the channel chamber into two parts, as shown in Fig. 2.6(a).

For the generation of monodisperse W/O/W double emulsions, 20 cP (μ_I) water-glycerin solution with 0.25% (w/v) SDS, 100 cSt (μ_M) silicone oil with 0.25% (v/v) Span 80, and 500 cP (μ_O) water-glycerin solution with 0.25% (w/v) SDS were used as the inner, middle and outer phases respectively, as shown in Fig. 2.6(a) and 2.6(b). As was mentioned before, there is no injection tube for guiding the inner phase, thus the location and shape of the cap that forms on the inner phase is greatly affected by the flow parameters. It is worth noting that this cap can touch the edge and intermittently close the inlet of the capillary, provided the flow rate of the inner phase is high enough compared to that of the middle phase. Accordingly, the flow path of the middle phase becomes significantly obstructed, and the inner phase is greatly squeezed by the middle phase, experiencing a large acceleration, followed by a later pinching stage and breakup This droplet formation process is clearly different from that of dripping or jetting in the above two sections (we define it as "plug" here), but is similar to the "dripping" regime defined by Cubaud and Mason [133] who study the formation of threads and droplets by hydrodynamic focusing into a square microchannel. Approximating the capillary as a square channel with width $h = \sqrt{\pi D_{orifice,1}^2/4}$, where $D_{orifice,1}$ is the diameter of the capillary inlet, the droplet diameter can be presented by [133]

$$\frac{D}{D_{orifice,1}} = k_1(\alpha_2 Ca_2)^n \tag{2.4}$$

where k_1 is an empirical constant, the volume fraction $\alpha_2 = Q_M/(Q_I + Q_M)$,

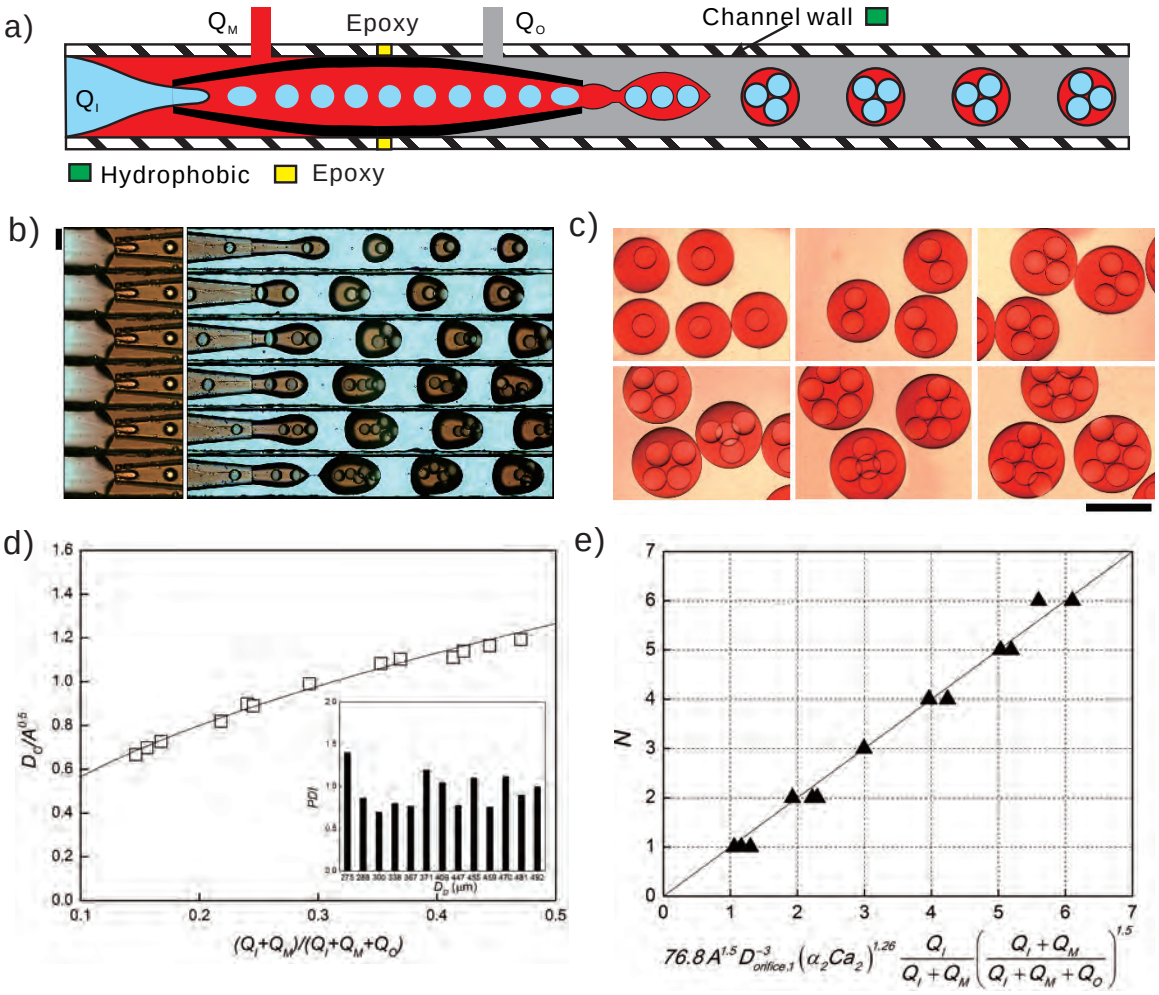

Figure 2.7: (a) Schematic of a microfluidic device for the formation of monodisperse O/W/O emulsions, in which, the inner phase is 20 cSt silicone oil (with 0.25% (v/v) Span 80), the middle phase is 100 cP water-gylcerin solution (with 0.25% (w/v) SDS) and the outer phase is 500 cSt silicone oil (with 0.25% (v/v) Span 80). (b) High-speed video frames of the generation of O/W/O emulsions with different flow rates, in which the inner (Q_I) and middle (Q_M) phase flow rates are fixed as 2 and 10 μL min^{-1} respectively, while the outer phase flow rates (Q_O) are varying as 65, 38, 29, 22, 17 and 15 μL min^{-1} respectively, producing 1 to 6 inner droplets, from top to bottom. Scale bar is 200 μm. (c) Photomicrographs of the O/W/O emulsion. Scale bar is 500 μm. (d) Experimentally measured double emulsion droplet diameter D_O(□) scaled by $A^{0.5}$ as a function of $(Q_I + Q_M)/(Q_I + Q_M + Q_O)$. The solid line represents the calculated results from eqn (2.7) with a best fitting parameter $k_2 = 0.62$. The inset shows the calculated PDI values. (e) Comparison of predicted (▲) and experimental measured number of encapsulated core droplets.

and the capillary number $Ca_2 = \mu_M Q_M / h^2 \sigma_{I,M}$, where $\sigma_{I,M}$ is the interfacial tension between the inner and middle phases (0.044 Nm^{-1} here). Finally n is a power law exponent of the product of the capillary number and the volume fraction ratio. By fitting the experimental results, we obtain

$$\frac{D}{D_{orifice,1}} = 0.42(\alpha_2 Ca_2)^{-0.42} \tag{2.5}$$

Fig. 2.6(c) shows a good fit between experimental data and the calculated results from eqn (2.5). The inset shows that the calculated (PDI) values are always below 1.5%, indicating highly monodisperse droplet generation.

The outlet orifice of the capillary has a typical co-flow structure. Imagining that all three liquid phases flow into a collection capillary which has an opening orifice with a radius of $R_{effective}$, defined by $\pi R^2_{effective} = k_2 A$, where k_2 is a proportionality constant and A is the known cross-sectional area of our square channel. So eqn (4.1) gives:

$$\frac{Q_I + Q_M}{Q_O} = \frac{\pi R^2_{jet}}{\pi R^2_{effective} - \pi R^2_{jet}} \tag{2.6}$$

Here $\mu_M/\mu_O = 0.2$, giving k, in eqn (4.2), as 10.78 [131]. Defining D_O as the outer diameter of the double emulsion droplets, combining eqns (4.2) and (2.6) gives:

$$\frac{D_O}{A^{0.5}} = 2.26 k_2^{1/2} \left(\frac{Q_I + Q_M}{Q_I + Q_M + Q_O} \right)^{1/2} \tag{2.7}$$

The best fit with experimental results gives a value of $k_2 = 0.62$ as shown in Fig. 2.6(d). The inserted image shows that the calculated (PDI) values are always below 1.5%, indicating highly monodisperse droplet generation.

Using above semi-empirical equation, the number N of encapsulated core droplets can be predicted as $N = f_1/f_2$, where f_1 and f_2 are the formation frequency of the inner single emulsion droplets and outer double emulsion droplets respectively [134].

From mass conservation within each stream:

$$N = \frac{f_1}{f_2} = \frac{Q_I/(\pi D^3/6)}{(Q_I + Q_M)/(\pi D_O^3/6)} \tag{2.8}$$

where D and D_O can be predicted from eqns (2.5) and (2.7) respectively, finally we get eqn (2.9).

Recall that A is the cross-sectional area of our square channel and $D_{orifice,1}$ is the diameter of the capillary inlet. It is shown in Fig. 2.6(e) that the number of the encapsulated core droplets can be generally predicted using eqn (2.9). When the calculated N is between two integers, the real encapsulated droplet number should be the integer which is closer to the calculated N by correspondingly adjusting D_O. Furthermore, under other flow conditions which give a calculated N that is more centered between two integers, such as 2.5, the real flow is observed to become non-steady, giving a real N changing randomly between 2 and 3.

It is shown in Fig. 2.6(b) that when the middle (Q_M) and outer (Q_O) phase flow rates are fixed, both the outer diameter D_O of the W/O/W double emulsions and N, the number of encapsulated core droplets, can be changed by varying the innermost phase flow rates (Q_I). However, it is also clearly shown in Fig. 2.6(b) that the diameter of the encapsulated core droplets D changes with Q_I, as the Q_M/Q_I also changes. In the cases that require control of D_O and N without changing D, one can change Q_O while keeping Q_I and Q_M constant, as shown in Fig. 2.6(f). This will be described in more details in the next section.

Oil-in-water-in-oil To prepare O/W/O emulsions with one tapered glass capillary (tapered at both ends), the corresponding surface treatment of the device is shown in Fig. 2.7(a). Only the right half channel inner wall needs to be hydrophobic. It is worth noting that although the outer surface of the right half capillary is in contact with the oil phase, surface modification is not necessary for it, as the co-flow structure

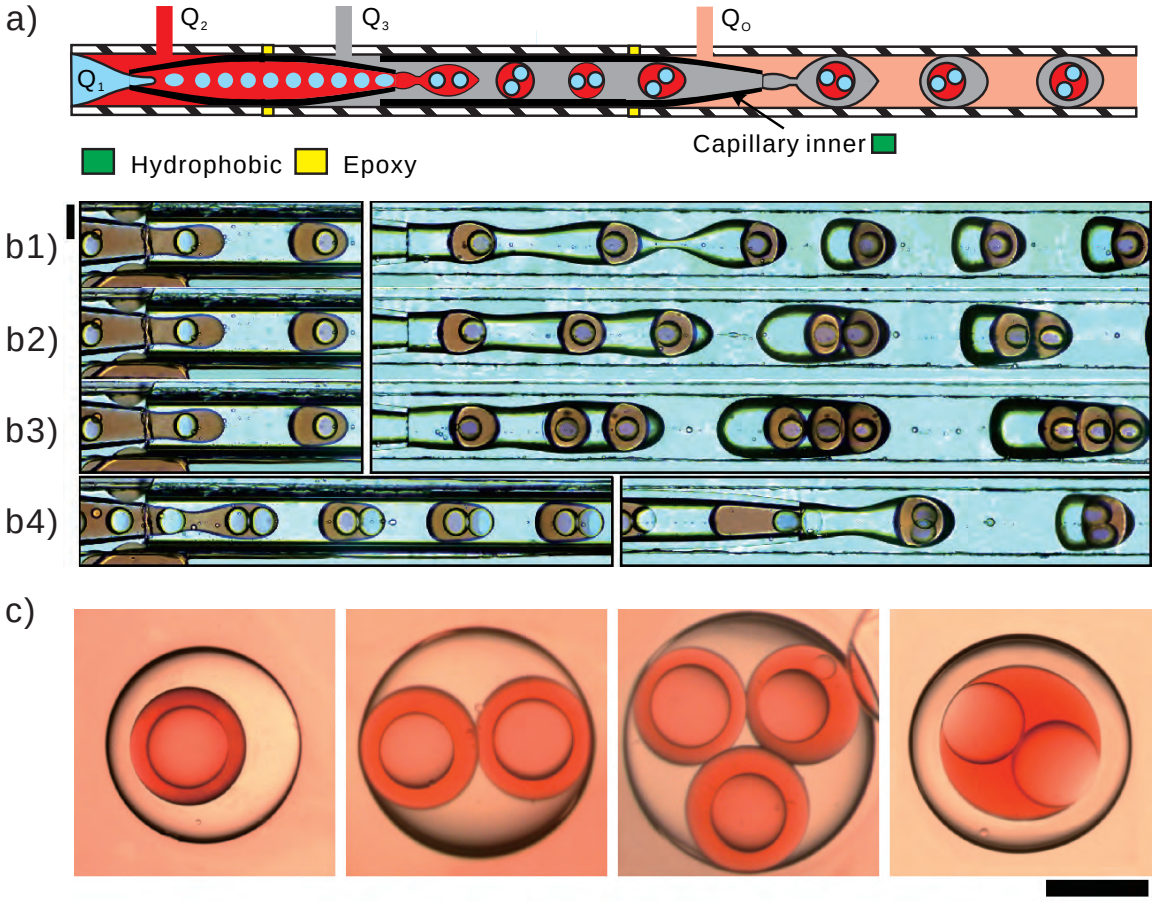

Figure 2.8: (a) Schematic of a microfluidic device for the formation of monodisperse O/W/O/W emulsions, in which, from inner to outer, the liquid phase is 20 cSt silicone oil with 0.25% (v/v) Span 80 (Q_1), 100 cP water-glycerin solution with 0.25% (w/v) SDS (Q_2), 500 cSt silicone oil with 0.25% (v/v) Span 80 (Q_3) and 1000 cP water-glycerin solution with 0.25% (w/v) SDS (Q_O), respectively. (b) High-speed video frames of the generation of O/W/O/W emulsions with different flow rates, in which, (b1, b2, b3) the flow rates Q_1, Q_2 and Q_3 are fixed as 1, 2 and 5 μL min^{-1} respectively, while the most outer phase flow rate Q_O is varying as 40, 20 and 13 μL min^{-1} respectively. (b4) The flow rates Q_1, Q_2, Q_3 and Q_O are 2, 2, 5 and 30 μL min^{-1} respectively. (c) Photomicrographs of the O/W/O/W emulsion. Both scale bars are 200 μm.

$$N = 76.8A^{1.5}D_{orifice,1}^{-3}(\alpha_2 Ca_2)^{1.26}\frac{Q_I}{Q_I+Q_M}\left(\frac{Q_I+Q_M}{Q_I+Q_M+Q_O}\right)^{1.5} \tag{2.9}$$

here forces the oil to adhere to the capillary outer surface.

In this configuration we use 20 cSt (μ_I) silicone oil with 0.25% (v/v) Span 80, 100 cP (μ_M) water-glycerin solution with 0.25% (w/v) SDS, and 500 cSt μ_O silicone

oil with 0.25% (v/v) Span 80 as the inner, middle and outer phases respectively to produce monodisperse O/W/O double emulsions, as shown in Fig. 2.7(b) As was mentioned in the previous section, in order to keep D, the diameter of the encapsulated core droplets constant, here the control of D_O and N was realized by varying Q_O while keep Q_I and Q_M constant. Firstly D was calculated by eqn (2.5), giving a value of 151 μm, which is very close to the measured value 144 μm. Then eqns (2.7) and (2.9) were used to predict D_O and N. Fig. 2.7(d) and 2.7(e) show excellent fit between experimental data and the predicted values. The inserted image shows that the calculated (PDI) values are always below 1.5%, indicating highly monodisperse droplet generation.

2.3.3 Preparation of monodisperse Triple emulsions O/W/O/W and (Gas + W)/O/W emulsions

Having demonstrated the flexibility in surface modification of our fabrication method, and successful preparation of W/O/W and O/W/O double emulsions, it is now straightforward to extend the method to prepare even higher-order multiple emulsion droplets through multi-step emulsification process using two capillary tubes. As depicted in Fig. 2.8(a), monodisperse O/W single emulsion droplets were produced at the inlet of the first capillary, then monodisperse O/W/O double emulsion droplets were produced at the outlet of the first capillary, where the flow enters the inlet of the second capillary. Monodisperse O/W/O/W triple emulsion droplets were finally produced at the outlet of the second capillary.

In this design the first capillary was tapered at both ends while the second one was only tapered at its outlet. The corresponding surface treatment of the device is also shown in Fig. 2.8(a). The whole inner surface of the second capillary is hydrophobic, whereas all other surfaces are untreated as hydrophilic in nature. Again, surface modification is not necessary here for the right half outer surface of the first capillary

as the co-flow structure will force the oil phase to adhere to the capillary outer surface.

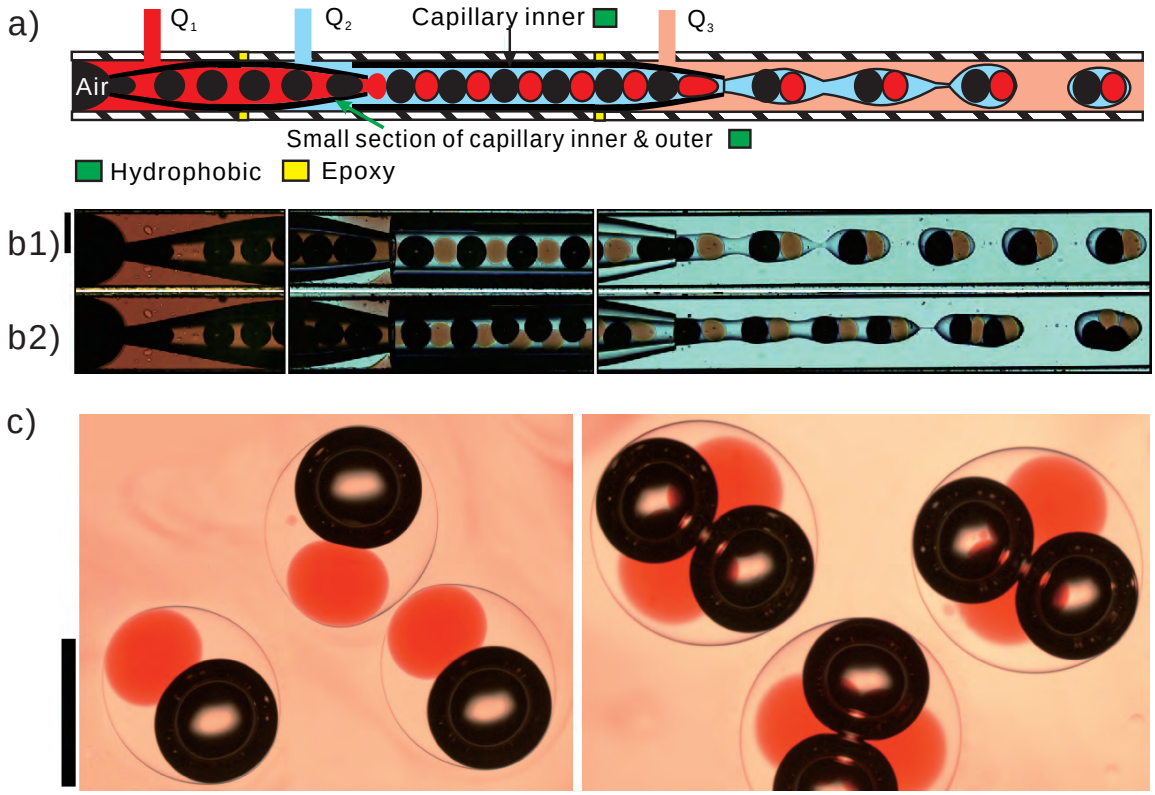

Figure 2.9: (a) Schematic of a microfluidic device for the formation of (G + W)/O/W emulsions, in which, the gas phase is air, the inner aqueous phase is 100 cP water-glycerin solution with 0.25% (w/v) SDS (Q_1), the oil phase is 500 cSt silicone oil with 0.25% (v/v) Span 80 (Q_2) and the outer phase is 1000 cP water-glycerin solution with 0.25% (w/v) SDS (Q_3). (b) High-speed video frames of the generation of (G + W)/O/W emulsions with different flow rates, in which, the flow rates Q_1, Q_2 and Q_3 are (b1) 5, 25 and 500 (b2) 10, 25 and 300 μL min^{-1} respectively, while the pressure for the air is fixed as 3 psi. (c) Photomicrographs of the (G + W)/O/W emulsion. Both scale bars are 500 μm.

In this configuration (Fig. 2.8(a)), from inner to outer, the liquid phase are respectively 20 cSt silicone oil with 0.25% (v/v) Span 80 (Q_1); 100 cP water-gylcerin solution with 0.25% (w/v) SDS (Q_2); 500 cSt silicone oil with 0.25% (v/v) Span 80 (Q_3) and 1000 cP water-gylcerin solution with 0.25% (w/v) SDS (Q_O). Four different structures of O/W/O/W triple emulsion droplets were shown in Fig. 2.8(b) and 6(c).

One interesting thing we observed was that if a short section of the first capillary inner surface was treated as hydrophobic (actually, which was accidentally when we

did the surface modification), the single oil emulsion droplets had a possibility to wet the first capillary inner surface when they passed through the first capillary outlet.

This possibility increases with the relative size of the oil droplet compared to the diameter of the first capillary outlet. When the wetting happened, the aqueous phase Q_2 was unable to encapsulate the oil droplets and then these oil droplets mixed with the oil phase Q_3 .

It is interesting to know what will happen if phase Q_1 is also immiscible with oil phase Q_3 . To investigate this, air was selected to replace the 20 cSt silicone oil. The corresponding surface treatment of the device was similar as that demonstrated in Fig. 2.8(a). The only difference here was that a short section ($\sim$ 3 mm) of the first capillary was modified as hydrophobic, as depicted in Fig. 2.9(a). Experimental results were shown in figure 7(b) : monodisperse air bubbles were firstly produced at the inlet, i.e., the flow-focusing section of the first capillary. Then air bubbles and aqueous droplets (phase Q_1) were alternately produced at the first capillary outlet (also the inlet of the second capillary).

Finally, monodisperse (G + W)/O/W emulsions encapsulating air bubble and aqueous droplets were produced at the outlet of the second capillary. Fig. 2.9(c) photomicrographically shows the monodisperse (G + W)/O/W emulsions encapsulating different number of air bubbles and oil droplets.

2.4 Conclusion

In this chapter, we present the design of a simple and inexpensive microfluidic device for generating monodisperse multiple emulsions. The advantages of our approach lie in a simple manufacturing procedure, inexpensive processing equipment, and flexibility in the surface modification of the designed microfluidic devices. It will take less than 30 minutes to fabricate a chip for double or triple emulsion generation, and the

cost is below one US dollar. Different types of chips have been designed and tested and the experimental results demonstrated the robust capability of our designed microfluidic devices for preparing monodisperse single, double, triple and multi-component emulsions. The relationship between encapsulated droplets number, emulsion droplets size and the flow parameters also has been investigated. We believe these simple and inexpensive microfluidic devices will benefit microfluidic researches.

Chapter 3

A co-flow-focusing monodisperse microbubble generator

3.1 Introduction

In chapter-1, we have introduced several common methods for producing microbubbles. In this chapter, we will focus on the generation of monodisperse microbubble with diameter less than 10 μm. The reason for our work on these small microbubbles is as following: First, microbubbles are widely used as ultrasound contrast agents for medical ultrasound imaging[135]. For this application, the bubble size should be smaller than 10 μm as bigger bubbles are not able to pass through the microvessels of the lungs [136]. The size range of microbubble contrast agents approved by U.S Food and Drug Administration (FDA) is 1 to 10 μm [137]. Second, microbubbles are also used as carriers to transport drugs to specific target tissues or genes into cells [138]. The walls of targeted microbubbles will rupture and drugs or genes are released from bubbles under ultrasound exposure. This also requires that bubble size should be small enough to penetrate into the smallest blood capillaries for releasing drugs or genes, the average size of microbubble carriers must be less than that of small blood capillaries (6-9 μm in diameter).

The monodispersity of bubble sizes is another critical factor in the above applica-

tions. The resonance frequency of a microbubble depends on its diameter. Therefore, highly polydisperse size distribution will give a wide range of resonance frequencies, which will reduce the sensitivity of the imaging system. In addition, the drug and gene delivery requires exact dosage to minimize toxic side effects and decrease costs for patients [139]. Therefore, highly monodisperse microbubbles with diameter less than 10 μm are desirable for diagnostic and therapeutic applications.

In recent years, microfluidic techniques have been developed to prepare microbubbles with narrow size distribution and smaller diameter (less than 10 μm). Most researchers used soft lithography techniques to produce a planar flow-focusing structure with a narrow orifice. By decreasing the orifice width down to about 10 μm, they can generate microbubbles with diameter less than 10 μm, i.e. comparable to the size of orifice [136, 140, 141, 142]. These common microfluidic methods listed above inevitably require complex fabrication techniques because of the complexity of soft lithography process or made use of a narrow orifice (about 10 μm) in which the gas and liquid phases pass through together. Impurities, such as dust or fine fibers are more common in the liquid-phase than the gas-phase. Blockage or clogging is therefore more common when the liquid passes through a narrow orifice. In our setup we will reduce this clogging problem, by only flowing the gas through the narrow section of the device. Gañán-Calvo *et al.* [95] successfully used a capillary together with a relatively large orifice ($\sim$ 100 μm) in a thin plate to generate microbubbles with diameter less than 10 μm. Castro-Hernandez *et al.* [143] made the exit channel much larger than its width avoiding the narrow orifice to successfully produce microbubbles with diameter around 5 μm. It was recently reported that researchers used flow-focusing structure to generate CO_2 microbubbles and then control the dissolution amount of CO_2 to form even smaller microbubbles with diameter less than 10 μm [144, 145]. In order to control the amount of dissolution of CO_2, the chemistry environment must be carefully controlled. Recently, Gordillo's group reported a microgroove structure

to produce microbubbles smaller than 10 μm with high generation frequency (larger than 10^5 Hz) [146]. In addition, coaxial electrohydrodynamic atomization (CEHDA) method was reported to have the ability to generate microbubbles with diameter less than 10 μm [147, 148]. A high voltage is required to be applied between the nozzle and electrode. CEHDA will introduce a wide range of size distribution and needs high voltage, which hinders its application in clinic use.

Herein, we report the design and fabrication of a simple and inexpensive microfluidic device, which is based on tapered glass capillaries and microscope glass slides, to produce highly monodisperse microbubbles with diameters less than 10 μm. The narrowest section along the liquid-phase path has a diameter of 75 μm, much bigger than the size of narrow orifice where liquid phase has to flow through to produce smaller microbubbles in many other microfluidic devices, except for references [143, 149]. Thus clogging is greatly suppressed for our chips. A simple scaling law based on capillary number and liquid-to-gas flow rate ratio, to predict bubble size, is also proposed and verified.

3.2 Methods

Our microfluidic devices are designed and fabricated using microscope glass slides and glass capillaries, as shown in Fig. 3.1. This fabrication technique was earlier used to produce multiple emulsions [150]. Our idea of generation of microbubbles is inspired by the 3D flow-focusing microfluidic device that was used to produce bubbles as small as 50 μm [87]. The difference here is that a tapered capillary (Capillary 1 in Fig. 3.1) with a long and thin tip is imbedded into the channel, with the purpose of providing a stable and small gas flow rate Q_g at its outlet. According to the Hagen-Poiseuille law, the calculated pressure difference between the capillary inlet and outlet is on the order of 10^5 Pa, which is in agreement with our gas supply pressure 430 kPa. The

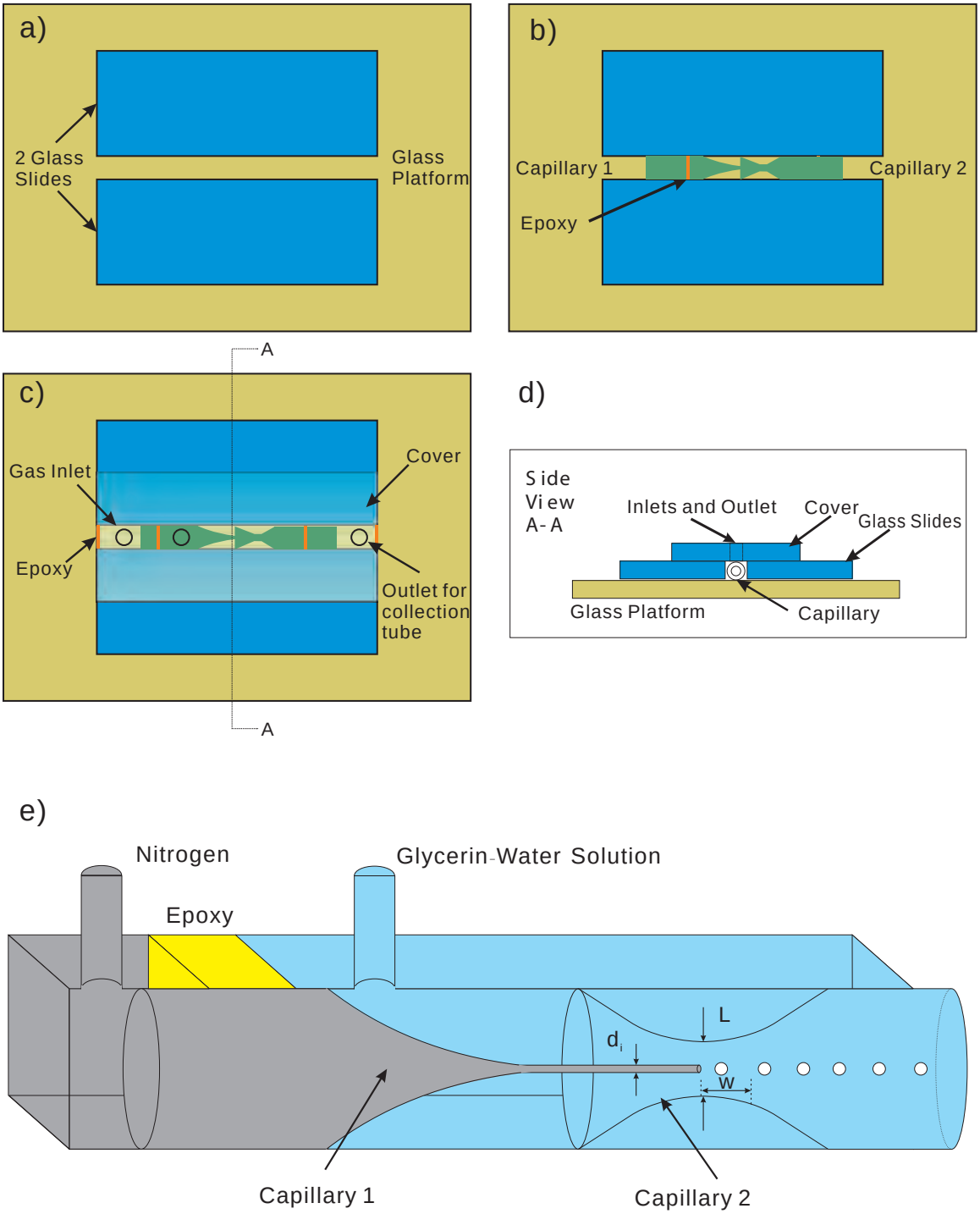

Figure 3.1: A schematic illustration of the microbubble generator based on microscope glass slides and glass capillaries. (a) Two glass slides are bonded onto a bigger platform, to form a channel. (b) Two capillaries were bonded into the channel in a designed arrangement. (c) Another glass slide is bonded on top of the channel, working as the cover of the microfluidic device. (d) Side view of the cross section at A-A. (e) A 3D schematic illustration of the designed microbubble generator.

fabrication process is as following. Firstly, two glass slides (75 mm × 25 mm, thickness of 1 mm were fixed onto a bigger microscope glass slide (75 mm × 50 mm, thickness of 1 mm) by epoxy (HP 250, ITW Devcon, Inc.), to form a channel. A glass capillary was used as temporary baffle between these two glass slides, providing the channel with a desired width that equals the OD of the capillary. Meanwhile, a second glass capillary (with 1 mm OD) was heated and pulled by a micropipette puller (P-1000, Sutter Instrument), to form tapered ends with desired orifice around 2 microns. The outer and inner surfaces of this pulled capillary were made hydrophobic by dipping it into FluoroPel PFC 801A solution (Cytonix Corporation). Then this capillary (Capillary 1, in Fig. 3.1) was inserted into another pulled capillary (Capillary 2, in Fig. 3.1) with a converging-diverging profile at its inlet end. The two capillaries were aligned in a manner that the sharp tip of Capillary 1 was located at the middle of the converging-diverging throat of Capillary 2. Both capillaries were bonded into the channel by epoxy, which splits the channel into different sections. Finally, a plexiglass or glass slide (76.2 mm × 25.4 mm, thickness of 1 mm), working as the cover of the microfluidic device, was bonded onto the channel, and syringe needles (16G×1-1/2", Air-Tite Products Co., Inc.) were bonded to the holes in the cover slide, to form inlets and outlet. Diamond core drills (Eternal Tools) were used to fabricate liquid inlets and outlet when glass cover was used. As shown in Fig. 3.1(e), nitrogen was used as the dispersed phase, glycerol-water solutions of different viscosities (1 cP, 10 cP, 100 cP and 1000 cP) were used as the continuous phase. Both phases were forced to flow through the converging-diverging throat of Capillary 2, to produce a stream of bubbles that can be collected at the outlet of the device. Nitrogen was supplied from a pressurized tank at a constant pressure $p_g = 430$ kPa. Its volume flow rate was calculated from the produced bubble size and production rate. Glycerol-water solution was fed by a syringe pump (Fusion 200, Chemyx, Inc.).

The bubble formation process at the co-flow-focusing region was observed and

recorded with a high-speed CMOS video camera Phantom V1610. The camera was equipped with a long-distance microscope objective with a magnification of 50X (Mitutoyo Corporation), which gave a corresponding pixel resolution of 0.5 μm. The geometry allows frame rates up to $\sim$ 130 kfps at resolution of 512 $\times$ 128 pixel. Backlighting was accomplished with a 350 W metal-halide lamp (Sumita Optical Glass, Inc.), which was shone onto a diffuser. Based on recorded images, the size of bubbles were analyzed using a Matlab program. All experiments were carried out at room temperature (22 °C).

3.3 Results and Discussion

As shown in Fig. 3.2 and Fig. 3.3, when nitrogen gas flows out from Capillary 1, it is hydrodynamically focused by the glycerin-water solution; dripping occurs, characterized by the periodic formation of monodisperse bubbles that are generated at the Capillary 1 outlet. The bubble size decreases with increase of Q_l, the liquid flow rate (Fig. 3.2) or μ_l, the liquid viscosity (Fig. 3.3). With further increase of Q_l, too high hydrodynamic pressure can be set up at this region, then nitrogen is unable to flow out and bubble generation stops. For each fluid condition, a video clip which contains more than 1,000 bubbles is recorded and is analyzed later by a Matlab program to extract bubble sizes. The smallest bubbles generated in this study are about 3.5 μm, as shown in Fig. 3.2(c). The size distribution of bubbles can be described as PDI index, which is defined as $PDI = \delta/d_{av} \times 100\%$, where δ is the standard deviation and d_{av} is the average bubble size. The calculated PDI value is shown in Fig. 3.4. As we can see, the PDI value is always below 1.5% for relatively bigger bubbles over 20 μm in diameter. Even for the smallest bubbles below 10 μm in diameter, the PDI value is still smaller than 2.5%, indicating highly monodisperse bubble generation in our device. However, for the smallest bubbles we

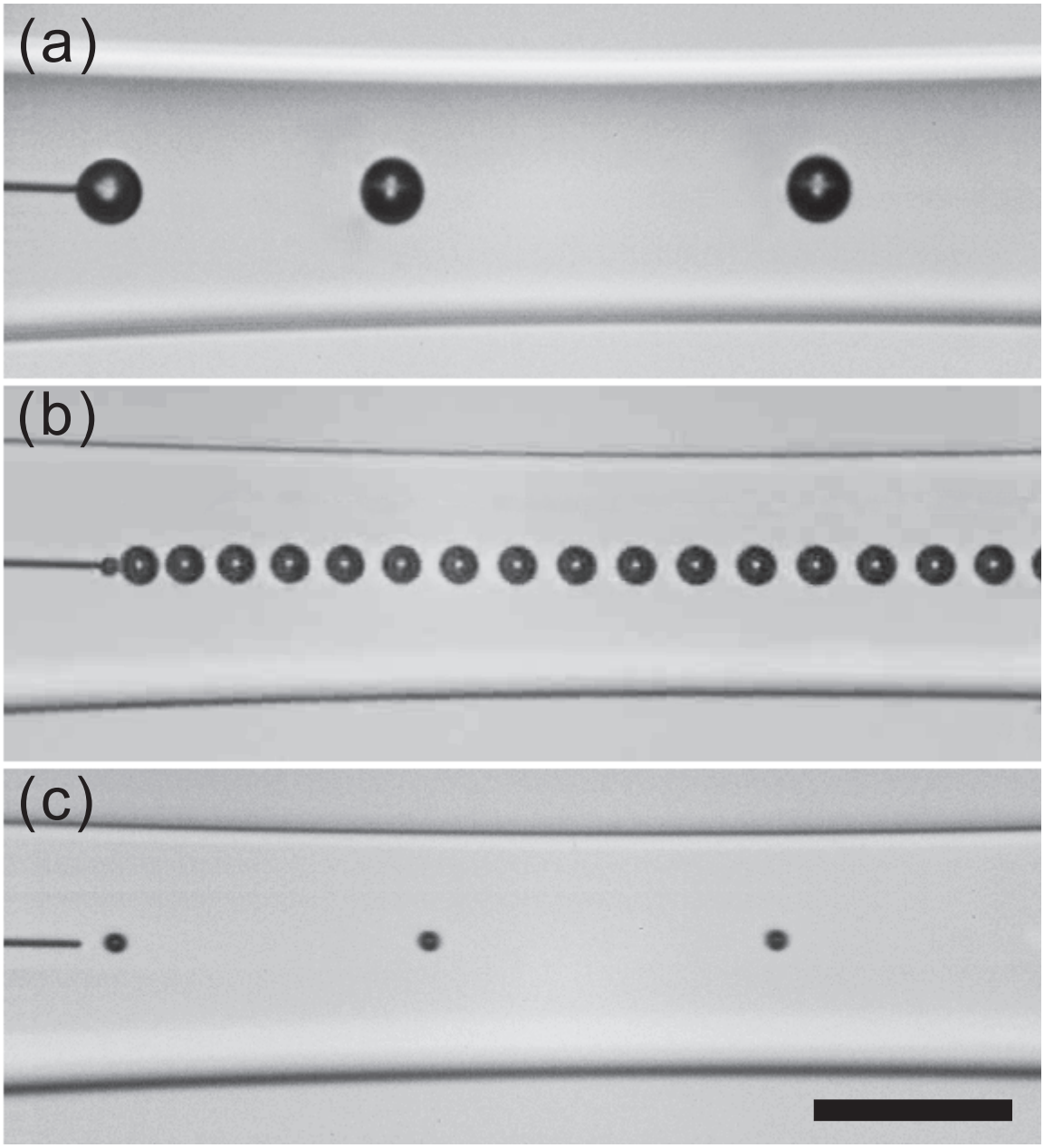

Figure 3.2: High-speed video frames of microbubbles generation with different liquid flow rates Q_l. Nitrogen pressure is constant: $p_g = 430$ kPa; Liquid viscosity is constant: $\mu_l = 1000$ cP. $d_i = 2.5$ μm and $L = 75$ μm, where d_i is the diameter of Capillary 1 outlet and L is the throat width of Capillary 2, as shown in Fig. 3.1(e). (a) $Q_l = 10$ μL min^{-1}; (b) $Q_l = 30$ μL min^{-1}; (c) $Q_l = 70$ μL min^{-1}. All videos recorded at 30,000 fps with 2 μs exposure time. Scale bar is 50 μm.

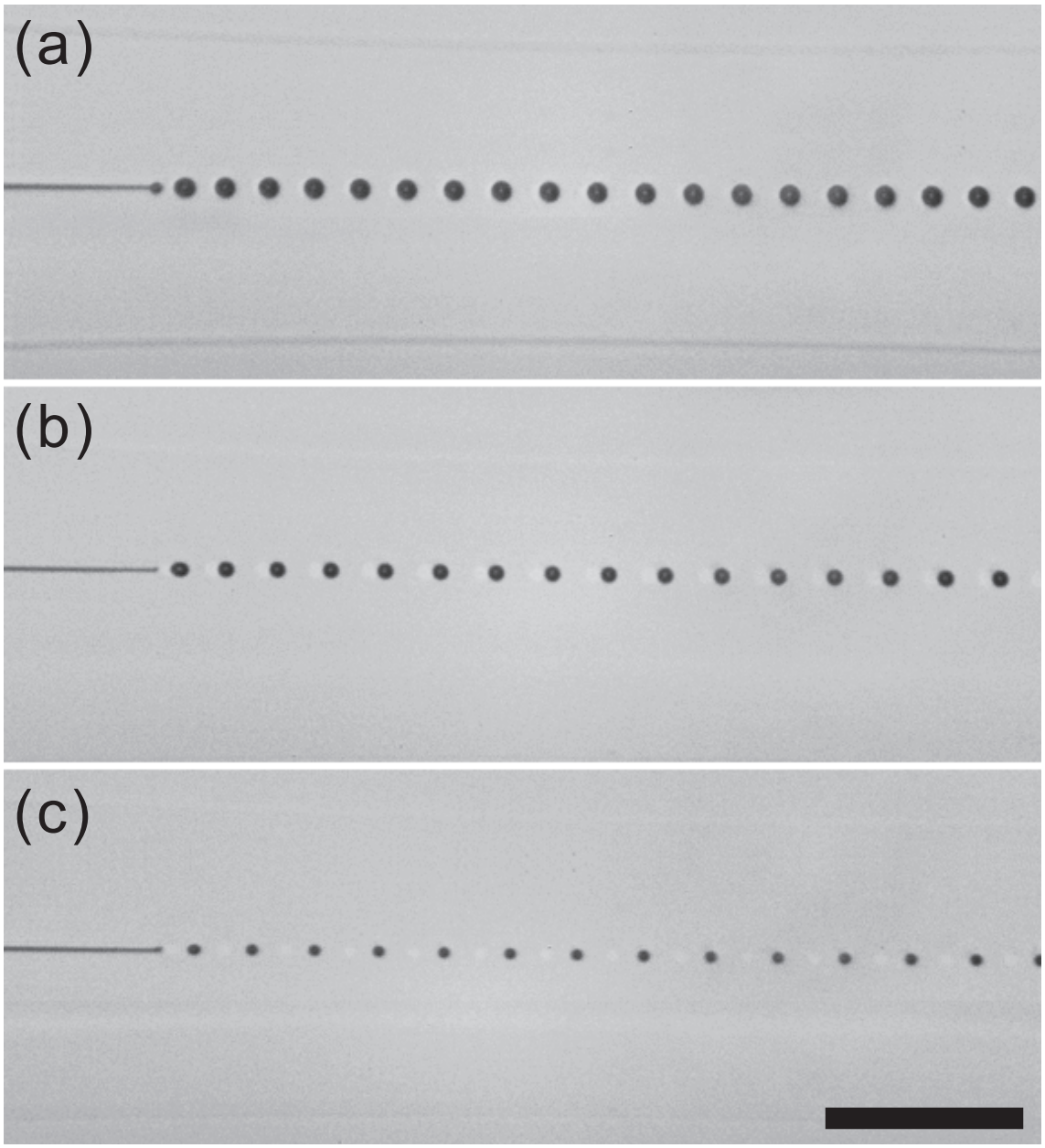

Figure 3.3: High-speed video frames showing dependence of microbubble sizes on liquid viscosity μ_l. Nitrogen pressure is constant: $p_g = 430$ kPa; Liquid flow rate is constant: $Q_l = 90$ μL min^{-1}. $d_i = 4$ μm and $L = 62$ μm, where d_i is the diameter of Capillary 1 outlet and L is the throat width of Capillary 2. (a) $\mu_l = 10$ cP, video recorded at 20,000 fps with 2 μs exposure time; (b) $\mu_l = 100$ cP, video recorded at 40,000 fps with 2 μs exposure time; (c)$\mu_l = 1000$ cP, video recorded at 40,000 fps with 2 μs exposure time. Scale bar is 50 μm.

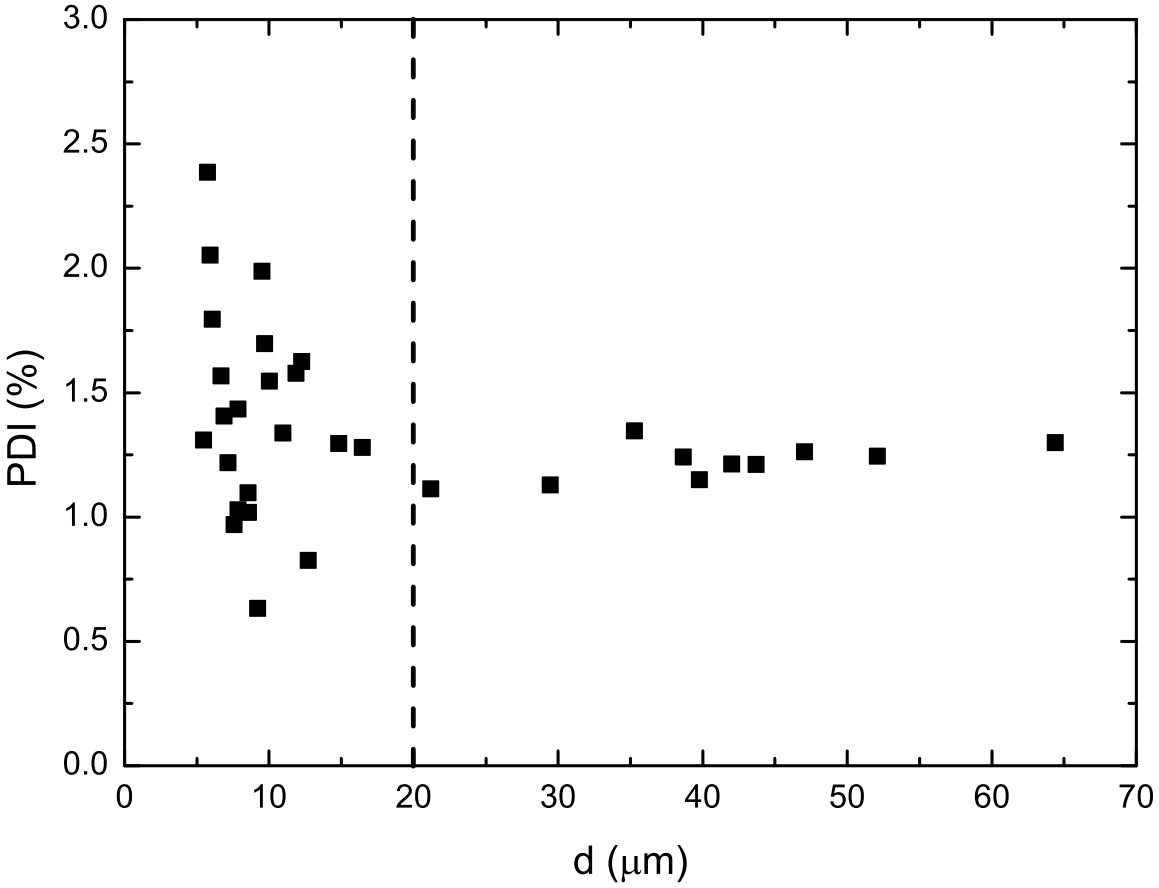

Figure 3.4: Polydispersity index, in %, as a function of bubble diameter. Note that even smal bubbles with diameter less than 10 μm can be generated with PDI value below 3%. The values for bubbles smaller than 20 μm are likely affected by imaging noise and should only be thought of as upper bounds.

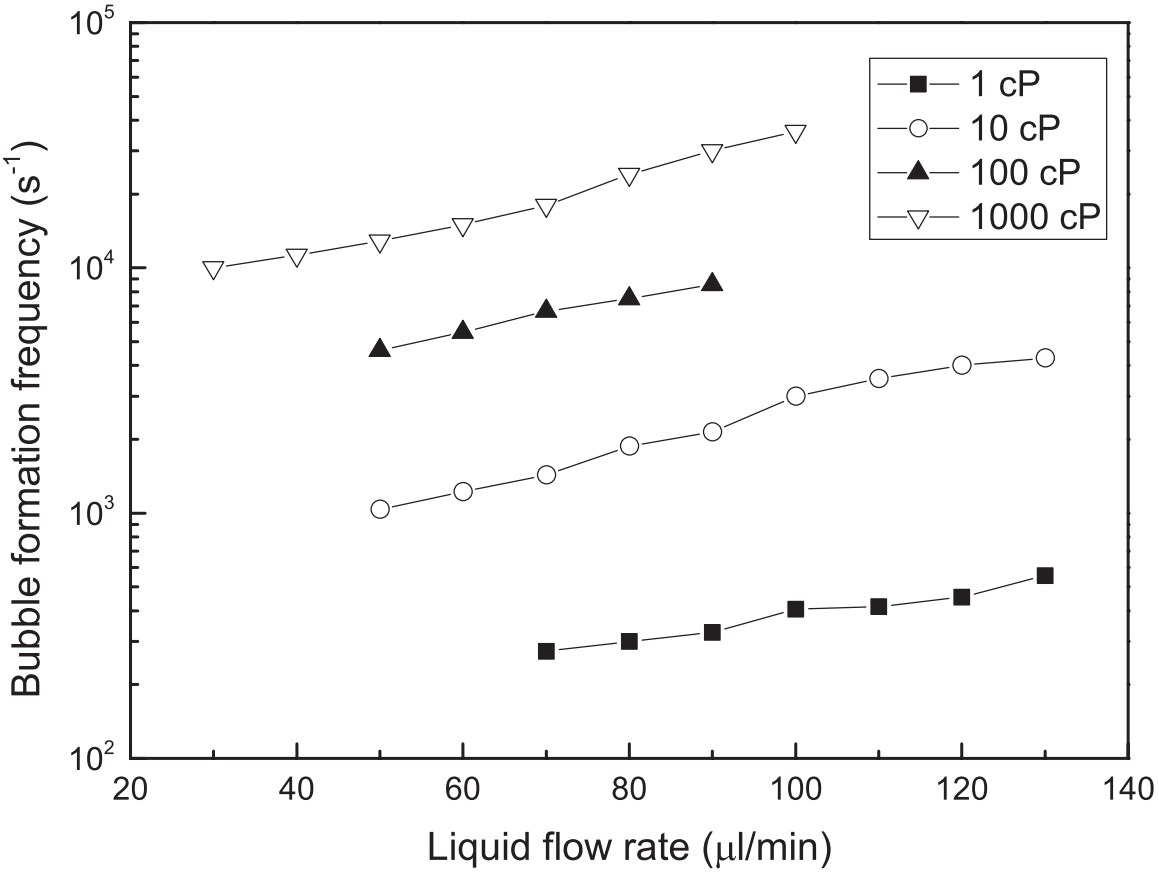

Figure 3.5: Microbubble formation frequency with different liquid flow rates and liquid viscosities (1 cP, 10 cP, 100 cP and 1000 cP).

expect significant effect on the PDI values from image noise, as we are integrating over only a few pixel area.

As shown in Fig. 3.5, the bubble production rate is measured to be as high as about 40 kHz. Microbubble formation frequency increases approximately linearly with the increase of liquid flow rate as viscosity is kept constant. For constant flow-rate the formation frequency increases greatly with the increase of the liquid viscosity.

The most relevant nondimensional numbers for multiphase flow in microfluidics, are the Reynolds number ($Re = \rho UD/\mu$), Weber number ($We = \rho DU^2/\sigma$) and capillary number ($Ca = \mu U/\sigma$), where U and D are the characteristic velocity and length scales; ρ, μ and σ are respectively the density, viscosity and surface tension. In our experiments, the range of Re for the flow of the continuous fluid at throat is

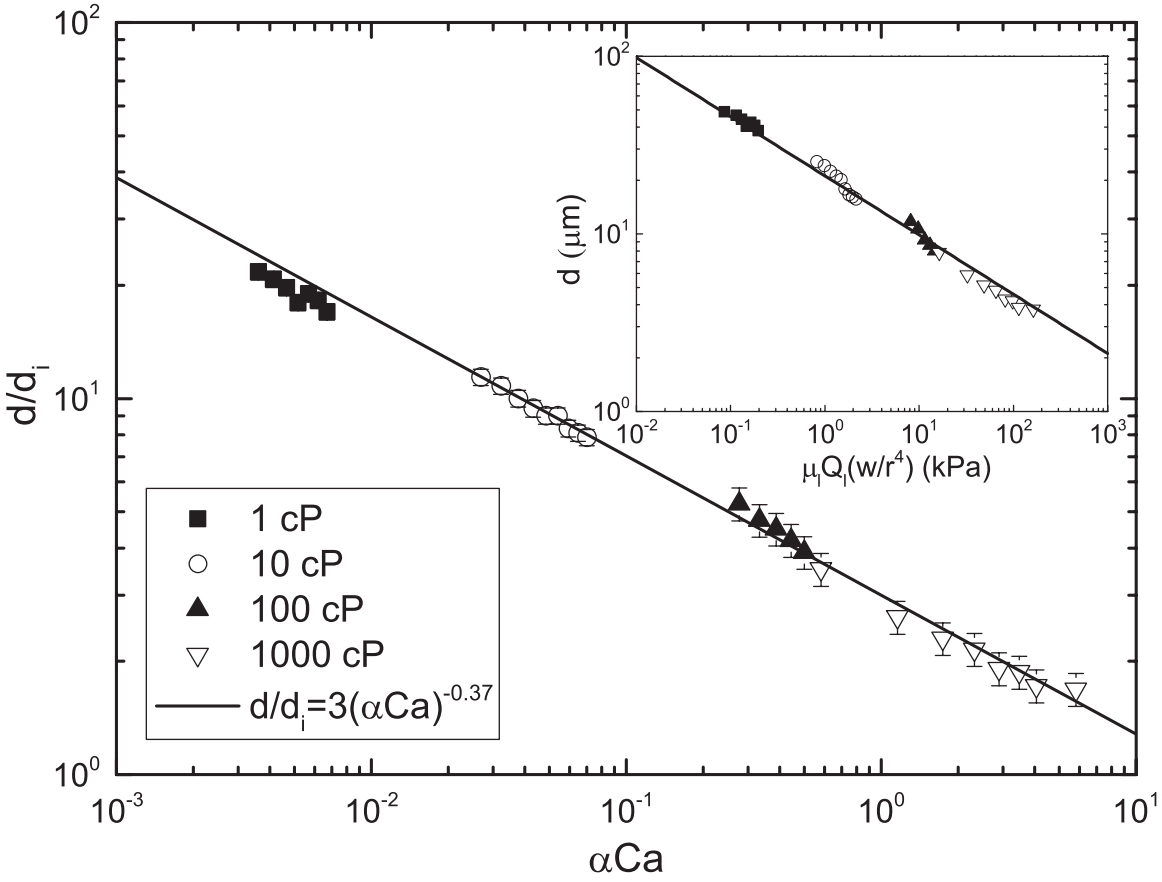

Figure 3.6: Optically measured average diameter of microbubbles as function of αCa, together with the scaling law $d/d_i \propto (\alpha Ca)^{-0.37}, \alpha = Q_l/(Q_l + Q_g)$, where d is bubble diameter and d_i is diameter of capillary 1 outlet, Q_l is flow rate of liquid and Q_g is flow rate of gas. Glycerin-water solution viscosity varies from 1cps to 1000 cps. The inset shows that microbubble size scaling proposed by Garstecki *et al.* [85]. This scaling is based on the product of the liquid flow rate Q_l and liquid viscosity μ_l, and scaled to the units of pressure by multiplying by w/r^4, where w is the axial length of throat section, where the curvature does not increase significantly as shown in Fig. 3.1(e). We use $w = 200\mu$m and r is the throat radius: $r = L/2 = 37.5\mu$m.

about $10^{-3} - 10^{1}$, which means the inertial force of fluid is small compared to the viscous force. The range of We is about $10^{-3} - 10^{-1}$, which similarly means the inertial force of fluid is also small compared to the surface tension. The range of Ca is about $10^{-3} - 10^{1}$, which means surface tension is dominant or comparable with the viscous force. So in our experiment, the inertial force effect can be ignored and the bubble formation is governed mainly by viscous forces and surface tension. From Fig. 3.6, we can see that at certain viscosity, bubble size decreases with the increase of the liquid phase flow rate. With the increase of the liquid viscosity, bubble size decreases significantly. It implies that viscous effects are so important in our experiment.

Therefore, to predict the produced bubble size in our experiment, we follow the method proposed by Cubaud and Mason [129], who investigated the dripping droplet size in a square microchannel, i.e., $d/d_i = m(\alpha Ca_l)^n$, where m and n are coefficients to be determined. The volume fraction of liquid $\alpha = Q_l/(Q_l + Q_g) \approx 1$ in our experiment. $Ca_l = \mu_l U/\sigma$ is the capillary number based on viscosity of the glycerin-water mixture, $U = (Q_l + Q_g)/(\pi L^2/4)$ is the flow velocity at the throat of capillary 2, d_i is the diameter of capillary 1 outlet, and L is the throat diameter of capillary 2 as shown in Fig. 3.1(e). The best fit with experimental results gives a value of $m = 3.0$ and $n = -0.37$, as shown in Fig. 3.6. The negative exponent of Ca agrees with the fact that strong viscous force favors the bubble pinch-off and decreases the bubble size, while interfacial tension acts against the bubble pinch-off and increases the bubble size during the bubble pinch-off stage [129].

Garstecki *et al* [85] proposed a different scaling law for the bubble size based on liquid flow rate, liquid viscosity and gas pressure in their experiment. They generated microbubbles in a planar microfluidic flow-focusing device. The range of Re in their experiment is low-to-moderate, similar to the range of Re in our experiment, implying that viscous effects are of similar importance in both experiments. This is indeed observed, in the inset of Fig. 3.6, were their scaling fits our data perfectly. The

scaling law here is $d = 21.24[\mu_l Q_l(w/r^4)]^{-1/3}$. Keep in mind that their formula ignores the value of the surface tension, which in our experiment is constant. To distinguish between these two scalings one would need to test liquids over a wide range of surface tensions, which is beyond the scope of the current experiments.

In addition, Gañán-Calvo [151] has proposed another bubble-size scaling law which is only based on the gas/liquid flow rates ratio and orifice diameter: $d_b/D = 1.1(Q_g/Q_l)^{0.4}$. However, as this law is proposed for large Re and We numbers, it is not applicable in our case, where viscosity and surface tension play a central role.

Fig. 3.6 tells us that to achieve micron sized bubbles in the current device, one can either use a continuous phase with high viscosity or low interfacial tension, thus adding surfactant can be a good option, which may also be helpful for stabilizing bubbles and prevent coalescence.

Finally, the jetting regime that has been extensively investigated when the core fluid is liquid [129, 152, 153], has not been observed in our experiments where the core fluid is gas. This is consistent with the work of Gordillo *et al.* [154] and Gañán-Calvo et al. [155] who showed that the liquid jets break up from convective instability, whereas a gas ligament is more easily broken up by absolute instabilities resulting from the shear at the gas-liquid interface and by surface tension instability. Sevilla *et al.* [156] identified experimentally the transition from bubbling to jetting in a coaxial air-core-liquid jet for the large Reynolds number situation, where viscous effects were insignificant. This does not apply in our study, as viscous effects are dominant, explaining the absence of a jetting regime.

3.4 Conclusion

In this chapter, we propose a novel glass capillary microfluidic device to generate microbubbles as small as 3.5 μm, with high monodispersity. Bubble sizes can be

controlled by varying liquid flow rate and adjusting the liquid viscosity. The bubble generation rate in our chip can exceed 40 kHz. The narrowest section along the liquid-phase path has a dimension of 75 μm, which greatly suppresses clogging problems for our chips. The key ingredient for success is the very smooth and low gas flow rate and an existence of a shear stress at the throat of Capillary 2. Furthermore, the fabrication process is simple and inexpensive, avoiding complex soft-lithography procedure. A theoretical model to predict the bubble size as function of the flow parameters is also proposed and verified.

In future work, we will focus on stabilizing these micron-size bubbles by adding phospholipids and surfactants to solve the bubble dissolving and coalescing problem after their generation. We thereby aim to use our device to produce coated microbubbles for use as ultrasound contrast agents, with a more monodisperse size distribution than is possible with commonly used methods.

Chapter 4

A simple and low-cost fully 3D-printed non-planar emulsion generator

4.1 Introduction

In chapter-1, we have reviewed the current fabrication techniques for fabrication of microfluidic devices. The popular methods normally require multi-step fabrication process and much time-consuming. Simpler and more straightforward techniques are still needed to develop. From this chapter, we utilize the emergent 3D printing technology to fabricate microfluidic devices for emulsion generation. This technology has not been fully exploited in microfluidic community so far.

A variety of 3D printing technologies have achieved great progress and made it possible to produce operational devices, such as microbatteries [157], scaffolds[158], microvascular networks[159] and reactionware[160]. This additive manufacturing technology has the potential to greatly reduce ecological footprints as well as the energy consumed in manufacturing. Also it is a data-driven process that patterns directly onto the substrate with ejection[161]. Due to its simple and low-cost fabrication

process, 3D printing technology has recently been applied to fabricate miniaturized devices [162, 163, 164, 165, 166]. However, few researchers have applied 3D printing technology to fabricate droplet generators, and so far, still employ the traditional planar structures to produce droplets [167, 168, 169], not taking advantage of 3D flow structure that can be easily produced by 3D printing technology for generating droplets. Following the elegant non-planar structure design by Rotem et al. [170] to generate droplets using the soft-lithography technique, here we report design and fabrication of a simple and low-cost 3D-printed emulsion generator devices, without need for surface treatment of the channel walls. Such treatment is not needed, due to the local 3D geometry of the junctions where emulsion droplets are produced. This 3D geometry of junctions can be printed through current 3D-printing technique but is difficult to achieve when using the conventional fabrication techniques. We have investigated droplet production in our 3D droplet generators and illustrated their feasibility for stable single and multiple emulsions production. Single emulsions, water-in-oil (W/O) or oil-in-water (O/W), as well as double emulsions, water-in-oil-in-water (W/O/W), oil-in-water-in-oil (O/W/O) or air-in-oil-in-water (Air/O/W) can be successfully produced by the same emulsion generator without surface wettability treatment. The simple fabrication process involves design using Computer Aided Design (CAD) software and printing using an inexpensive commercial desktop 3D printer. The total cost of materials for one generator is below $1. The whole printing process only takes a couple of hours. This capability could be highly convenient for researchers, especially for those not familiar with complicated fabrication skills, to design and fabricate customized miniaturized devices rapidly. Furthermore, uniform scaling laws for prediction of emulsion (W/O and O/W) droplet sizes generated in different regimes are successfully proposed. Finally, we produce magnetic particles based on droplet templates, demonstrating the extensive possibilities of chemical and material applications through our 3D-printed miniaturized devices.

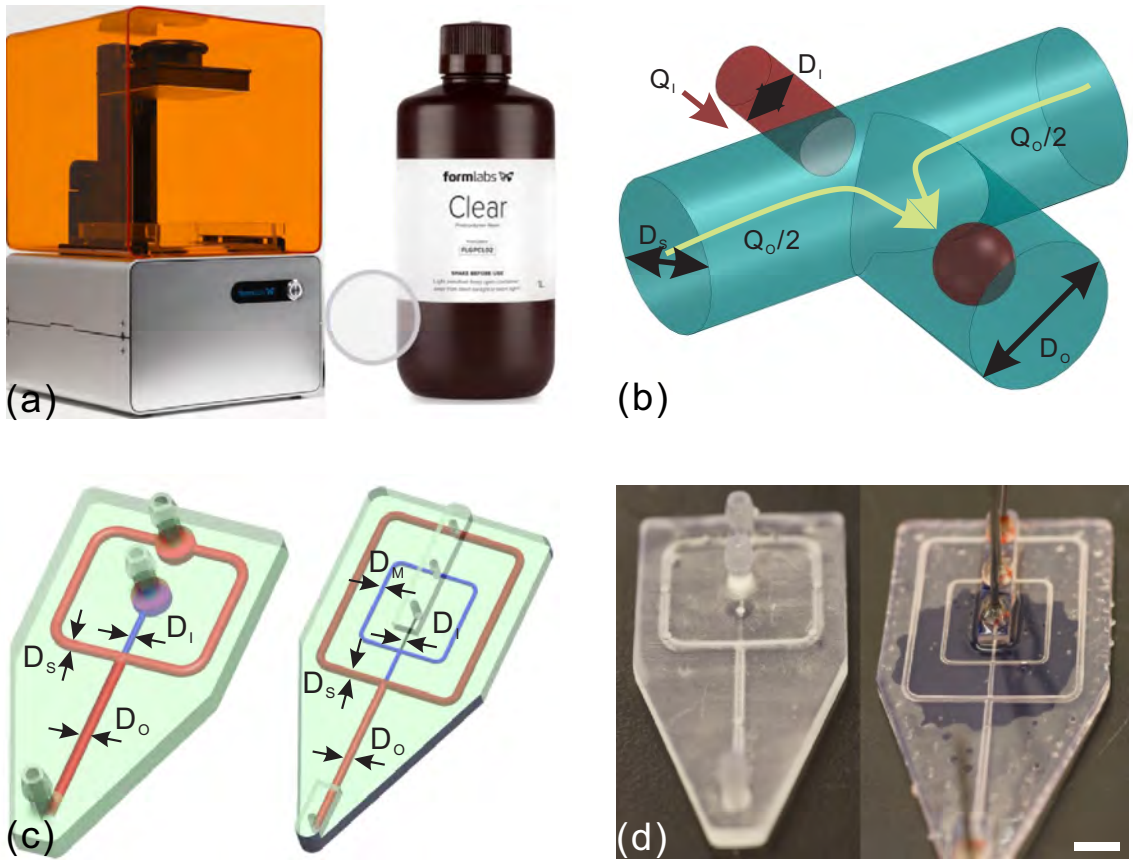

Figure 4.1: (a) Photograph of the Form 1+ printer with its clear resin, used to fabricate our emulsion generator. (b) Local 3D structure design for emulsion generation. The inner phase (Q_I) flows in the central inlet channel with diameter $D_I = 0.6$ mm. The outer phase (Q_O) flows in the two side channels with diameter $D_S = 1$ mm. These two phases flow together into the outlet channel with diameter $D_O = 1$ mm. (c) Schematics of single and double emulsion generator. For double emulsion generator, the dimensions are $D_I = 0.6$ mm, $D_M = 1$ mm and $D_O = 2$ mm. (d) 3D-printed single and double emulsion generators. Scale bar is 1 cm.

4.2 Methods

Emulsion droplet generators are designed using Solidworks (Dassault Systemes S.A.), and then fabricated with Form 1+ printer (Formlabs, Inc.) as shown in Fig. 4.1(a). The printer only costs $2799 and is based on the stereolithography technique to build structures [171]. The great advantage of this technique applied in microfluidics lies in the clear resin provided for printing, which provides an excellent transparency and thus allows researchers to observe the internal fluid field and develop variety of microfluidic applications requiring optical access.

In addition, the Young's modulus of postcured clear resin is 2.7 Gpa, much larger than that of PDMS: 0.75×10^{-3} Gpa. Thus, our devices printed by this material are capable of withstanding high liquid flow rate and input pressure.

This clear resin contains modified acrylate oligomer and monomer, together with a photoinitiator and their weight ratio is propriety.

The basic geometry of our emulsion generator is illustrated in Fig. 4.1(b). The center inlet with diameter $D_I = 600$ μm introduces the inner dispersed phase Q_I, whereas two side inlets with diameter $D_S = 1000$ μm introduce the outer continuous phase Q_O. Both inner and outer phase flow out through the outlet with diameter $D_O = 1000$ μm. The center inlet is smaller than the side inlets, forming a 3D junction where the inner phase is pinched-off to generate droplets without touching the downstream walls. This 3D junction thereby allows the outer phase coming from the side inlets to encapsulate the inner phase completely when the flow rate of outer phase is large enough, which prevents the inner phase from contacting the channel walls. Consequently, the drop formation at the junction will not be affected by the channel wall wetting conditions. Therefore, the complicated process of local surface treatment on channel walls is avoided. Both single emulsions of W/O and O/W, are successfully produced in the same emulsion generator without any surface treatment.

Subsequently, we extend this single 3D junction to two sequential junctions for

double emulsion production. As shown in Fig. 4.1(c), the inner channel with diameter $D_I = 600$ μm carries the inner phase to the first junction. The middle channel with diameter $D_M = 1000$ μm carries the middle phase also to the first junction to pinch off the inner phase and generate inner droplets. Then the inner droplets and middle phase are carried to the second junction, where the outer phase carried by the outer channel with diameter $D_O = 2000$ μm squeezes the middle phase and generate outer droplets. All three phases are collected in the outlet channel with diameter 2000 μm. Due to the gradual increase of channel diameter from inner to outer, both the inner phase in the first junction and the middle phase in the second junction are prevented from contacting the channel walls. Thus, different double emulsions (W/O/W, O/W/O and Air/O/W) can be generated using the same chip without the need to modify the wettability of the channel walls. Such special 3D structure will require complicated fabrication processes with high-cost equipment and skilled people for traditional fabrication techniques, but it can be simply and inexpensively fabricated through 3D printing technology.

Syringe needles are inserted into the openings in the chip, sealed by epoxy to form inlets and outlet. Meanwhile, we design and print a cone inlet, which can be directly connected with tubes for liquid input as shown in Fig.1 (c). Silicone oil (Sigma-Aldrich Corp.) of different viscosities are employed as the oil phases, and water-glycerin mixtures of different viscosities are employed as aqueous phases. Red dyes are applied in the aqueous phase to enhance observation. Up to three syringe pumps (Fusion 200, Chemyx, Inc.) are applied for driving the fluids into the generators. The formation process of the emulsion droplets are observed and recorded with a high-speed CMOS video camera SA-3. The sizes of the emulsion droplets are analyzed using free image-analysis software ImageJ.

All experiments are carried out at room temperature (22 °C).

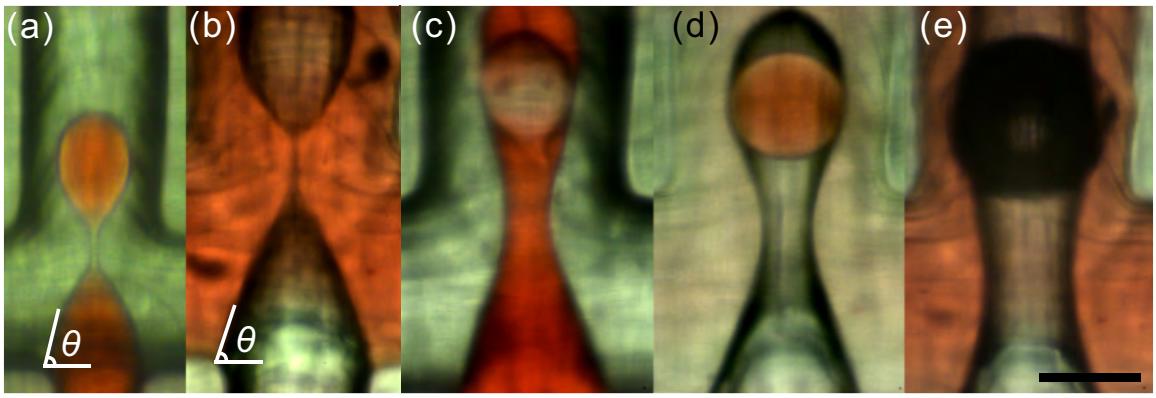

Figure 4.2: Different composite emulsions generated in our devices. (a) Single W/O emulsion, (b) single O/W emulsion, (c) double O/W/O emulsion, (d) double W/O/W emulsion and (e) double Air/O/W emulsion. For inner aqueous phase, the dynamic contact angle is $\theta \sim 82°$; For inner oil phase, $\theta \sim 70°$. Red dyes are used in the aqueous phase. Scale bar is 1 mm.

4.3 Results and Discussion

Table 4.1: Viscosities of the different liquids used in our experiments for generation of single and double emulsions.[a]

W/O		O/W		W/O/W			O/W/O			Air/O/W		
inner	outer	inner	outer	inner	middle	outer	inner	middle	outer	inner	middle	outer
20	50	20	50	20	500	1000	20	500	1000	Nitrogen	500	500
20	100	20	100	—	—	—	—	—	—	—	—	—
20	350	20	350	—	—	—	—	—	—	—	—	—

[a]W: water-glycerin mixture, unit: cP; O: silicone oil, unit: cSt.

First, we choose different viscosities of silicone oil listed in Table 4.1 as the outer continuous phase and 20 cP water-glycerin mixture as the inner disperse phase, to generate W/O emulsions as shown in Fig. 4.2(a). Since our printing material has a higher affinity for the oil phase, the inner aqueous phase can be easily encapsulated by outer oil phase. With the flow rate ratio alteration, two regimes, dripping and jetting, are observed [172]. The dynamic contact angle of inner aqueous phase during the drop formation, $\theta \sim 82°$, as shown in Fig. 4.2(a).

After successful generation of W/O emulsions, we use the same generator to also generate O/W emulsions as shown in Fig. 4.2(b). Different viscosities of water-

glycerin mixture listed in Table 4.1 are used as outer aqueous phase respectively and 20 cSt silicone oil is used as inner oil phase. Before O/W emulsion generation, isopropyl alcohol and DI water are used to flush the channels for 10 minutes to remove the oil residues and water-glycerin mixture is pumped into the chip first. Then, the inner silicone oil is injected into the chip. We always keep the inner oil phase flow rate (Q_I) less than the outer aqueous phase flow rate (Q_O), $Q_{I,max} \approx 0.35 Q_O$, to prevent the inner oils phase from wetting the channel walls. Once the inner oil contacts the channel walls and form an oil film on the walls, oil drops cannot be produced anymore. No dripping or jetting regime is observed in O/W emulsion generation, while an oil cap as shown in Fig. 4.2(b) is completely surrounded by outer aqueous phase and pinched-off to generate droplets. The dynamic contact angle of inner oil phase during the drop formation, $\theta \sim 70^\circ$, as shown in Fig. 4.2(b).

We have carried out two series of experiments for both W/O and O/W emulsion droplet production. 1. Keeping the inner phase flow rate constant and increase the outer phase flow rate until the inner phase fails to flow out from the inner channel due to the high shear exerted by outer liquid phase; 2. Keeping the outer phase flow rate constant and increase the inner phase flow rate until the inner phase contacts the channel wall and no droplet can be generated. In the first series of experiments, we keep the inner phase flow rate constant as 30 μL min^{-1}, and increase the outer phase flow rate from 200 μL min^{-1} to 2000 μL min^{-1}. With the increase of the outer phase flow rate, droplet generation sizes decrease, as depicted in Fig. 4.3. Under the same flow rate ratio, smaller droplets are generated with the higher outer phase viscosity, because higher viscosity introduces higher shear-stress to the inner phase and make it pinch off more easily to generate smaller droplets.

In the second series of experiments, we keep the outer phase flow rate constant for each viscosity of the outer oil phase: [900 μL min^{-1} for 50 cSt; 700 μL min^{-1} for 100 cSt; 500 μL min^{-1} for 350 cSt] for the W/O emulsion, and for each viscosity

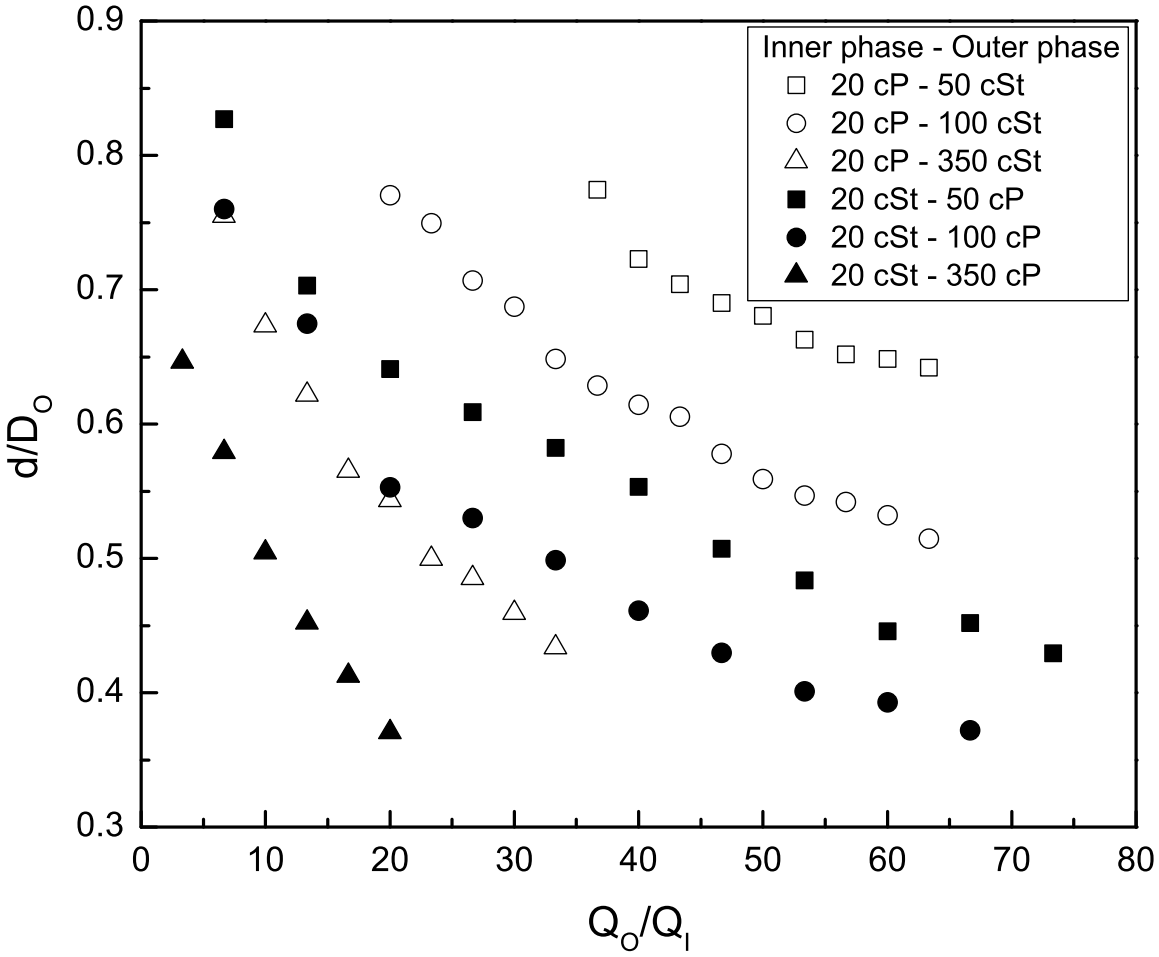

Figure 4.3: Aqueous (open symbol) and oil (solid symbol) emulsion droplet diameter (d) scaled by the diameter of outlet channel (D_O) as a function of liquid flow rate ratio (Q_O/Q_I). The two different emulsions are generated in the same emulsion generator with the same constant inner phase flow rate $Q_I = 30$ μL min^{-1} while increasing the outer phase flow rate Q_O from 200 μL min^{-1} to 2000 μL min^{-1}. Liquid choices are listed in Table 4.1.

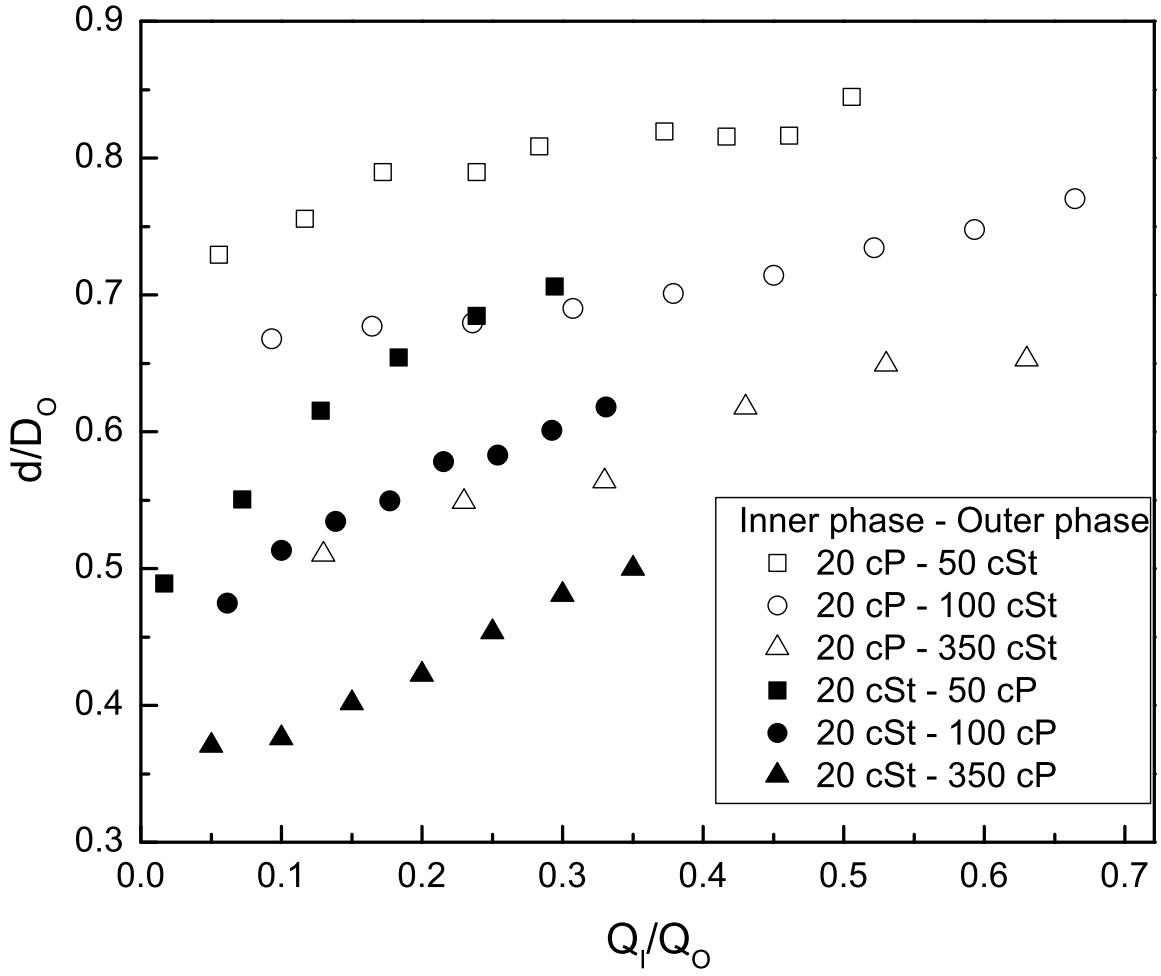

Figure 4.4: Aqueous (open symbol) and oil (solid symbol) emulsion droplet diameter (d) scaled by the diameter of outlet channel (D_O) as a function of liquid flow rate ratio (Q_I/Q_O). Two different emulsions are generated in the same emulsion generator with the constant outer phase flow rate Q_O. For W/O emulsions, [Q_O = 900 μL min^{-1} for 50 cSt, Q_O = 700 μL min^{-1} for 100 cSt, Q_O = 500 μL min^{-1} for 350 cSt]; For O/W emulsions, [Q_O = 900 μL min^{-1} for 50 cP, Q_O = 650 μL min^{-1} for 100 cP, Q_O = 300 μL min^{-1} for 350 cP]. Liquid choices are listed in Table 4.1.

of the outer aqueous phase: [900 μL min^{-1} for 50 cP; 650 μL min^{-1} for 100 cP; 300 μL min^{-1} for 350 cP] for the O/W emulsion. With the increase of inner phase flow rate, droplet generation sizes increase, as depicted in Fig. 4.4.

In addition, as shown in Fig. 4.4, oil drops (solid symbol) cannot be generated when $Q_I/Q_O > 0.4$, because the oil cap has grown so big that it contacts the channel walls, which prevents the drop generation. On the other hand, aqueous drops (open symbol) can still be generated beyond this flow rate ratio, because the inner aqueous phase is in the jetting regime and droplets can also be generated downstream. This difference originates from the different droplet generation mechanism due to different wetting conditions for the inner phase.

The most relevant nondimensional parameters for multiphase flow in microfluidics, are the Reynolds number ($Re = \rho UD/\mu$) and Capillary number ($Ca = \mu U/\sigma$), where U and D are the characteristic velocity and length scale; ρ, μ and σ are density, viscosity and interfacial tension between the liquids, respectively. In the first series of experiments with small constant inner phase flow rate, the Reynolds number of inner phase is much smaller than unity ($Re \ll 1$), which means the inertial forces can be ignored compared with the viscous forces. The range of outer phase Capillary number from 0.01 to 1 ($Ca : 0.01 \sim 1$), means that the surface tension is dominant or comparable with the viscous forces. According to these facts and considering the contact angle effect on the drop formation, we propose a uniform scaling law for prediction droplet sizes generated in our 3D emulsion generator of both emulsion (W/O and O/W). This scaling is based on the method used by Cubaud and Mason [173], who studied the dripping droplet size in a 2D planar cross junction. We incorporate the dynamic contact angle effects and get $d/D_O = m[\alpha(Ca \cdot \cos\theta)]^n$, where m and n are coefficients to be determined and $\alpha = Q_O/(Q_O + Q_I)$ is the volume fraction of outer liquid. θ is the dynamic contact angle of inner phase during the drop pinch-off. D_O is the outlet channel diameter. In our study, $Ca = \mu_O U_O/\sigma$, where μ_O is the viscosity

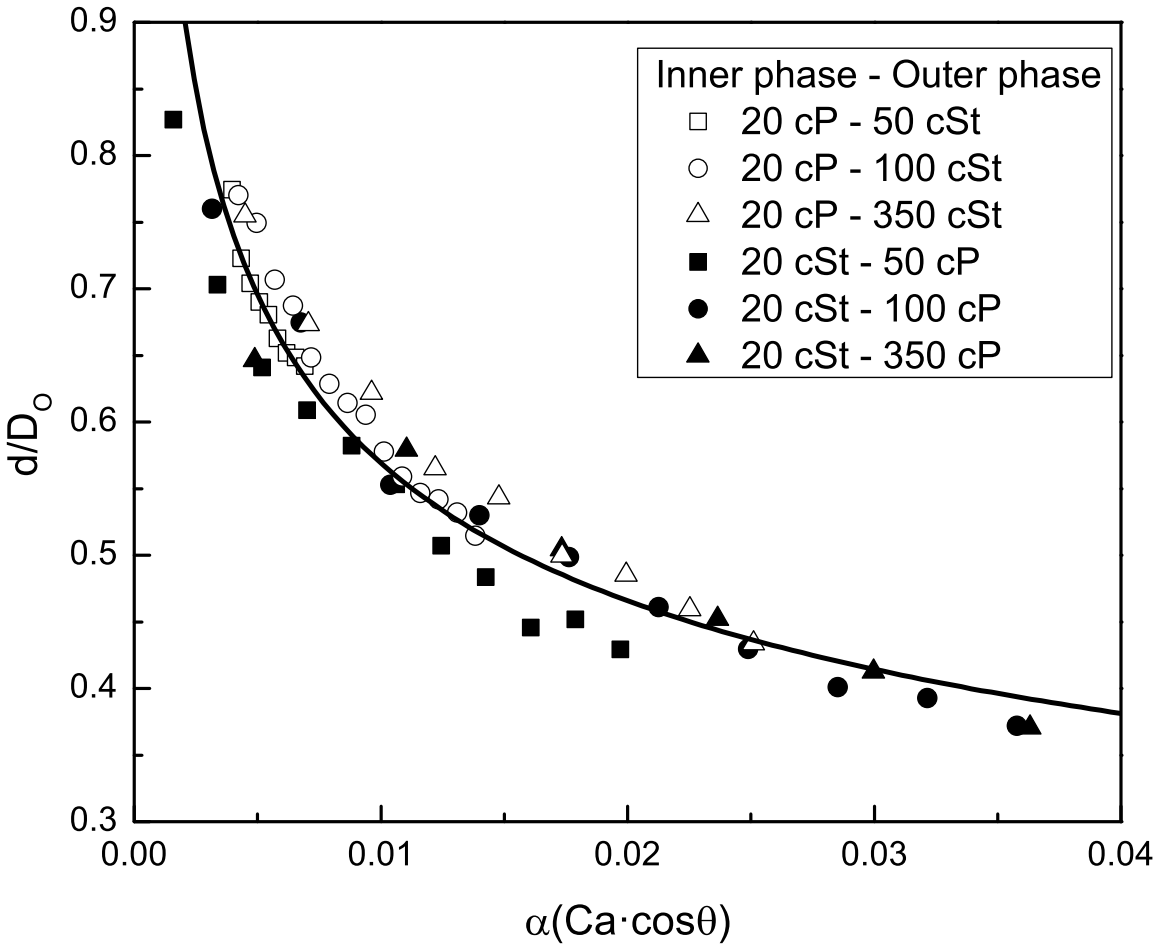

Figure 4.5: Aqueous (open symbol) and oil (solid symbol) emulsion droplet diameter as a function of $\alpha \cdot (Ca \cdot \cos\theta)$, where θ is the dynamic contact angle of inner phase during drop formation. $\theta \approx 82°$ for aqueous inner phase, and $\theta \approx 70°$ for oil inner phase.

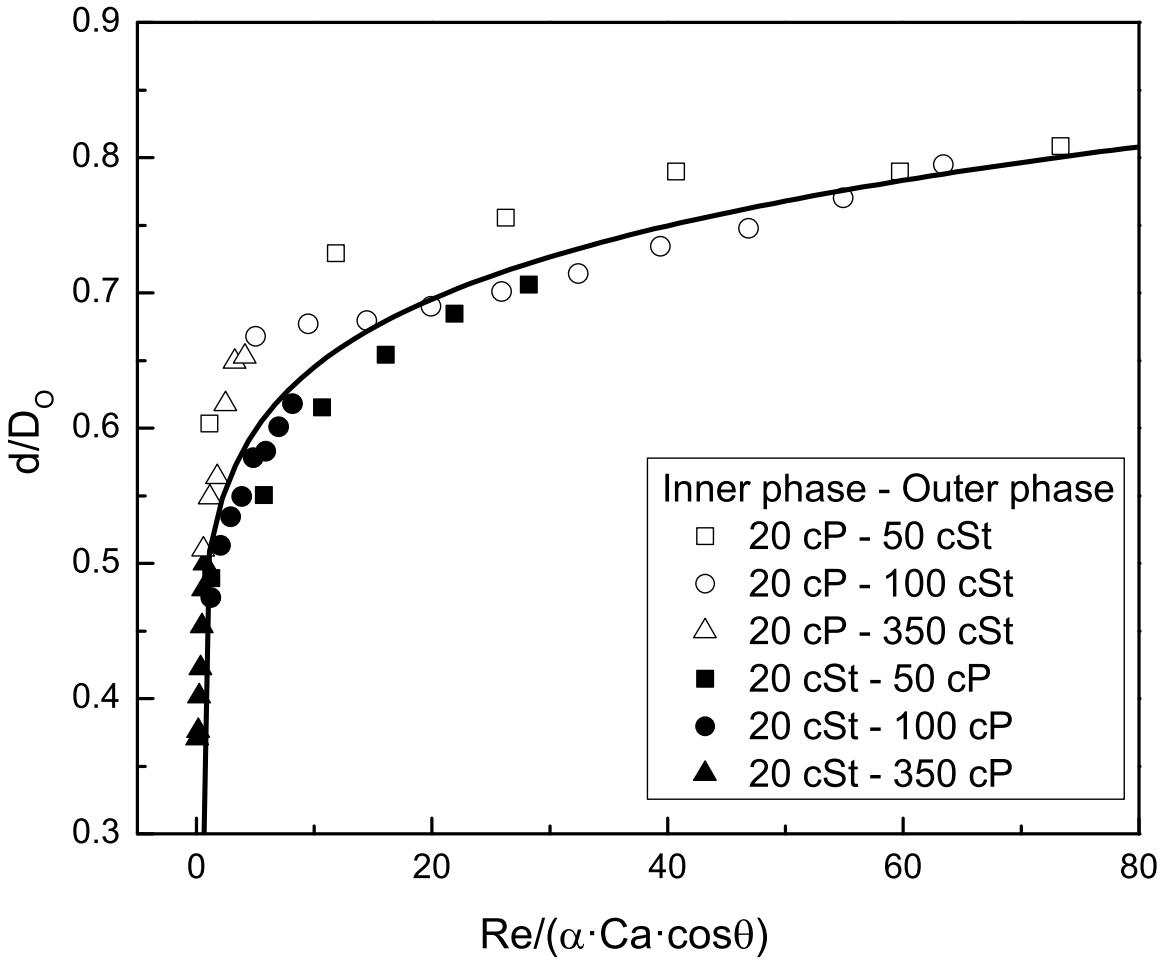

Figure 4.6: Aqueous (open symbol) and oil (solid symbol) emulsion droplet diameter as a function of $Re/(\alpha \cdot Ca \cdot \cos\theta)$, where θ is the dynamic contact angle of inner phase during drop formation. $\theta \approx 82°$ for aqueous inner phase, and $\theta \approx 70°$ for oil inner phase.

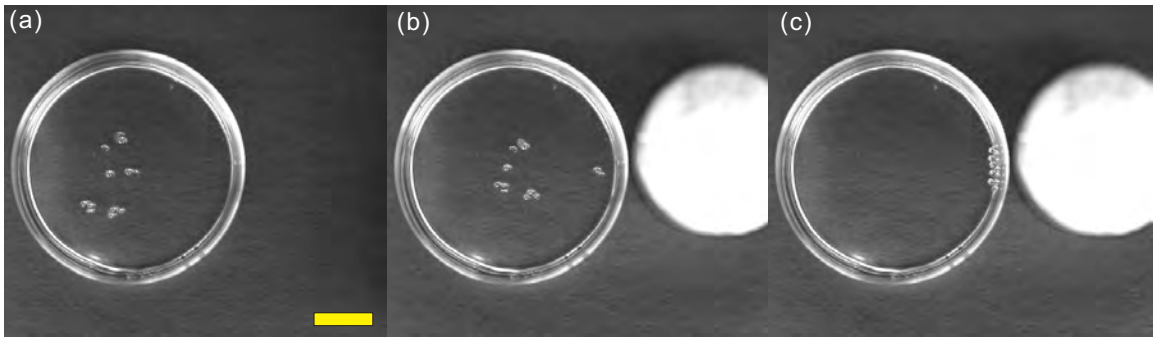

Figure 4.7: Functionalized particles fabricated in our 3D printed chip. (a) Magnetically responsive microspheres are dispersed in water inside a petri dish without applied magnetic field. When a magnet (white circle) is brought near the petri dish (b), these particles are attracted by the external magnetic field and move towards it (c) until they reach the edge. Scale bar is 10 mm.

of outer phase, σ is the interfacial tension between the inner phase (water-glycerin mixture) and outer phase (silicone oil): 40 mN m^{-1} and $U_O = Q_O/(\pi D_O^2/4)$ is the outer phase flow velocity in the outlet channel. The best fit with experimental results gives a value of $m = 0.15$ and $n = -0.29$, as shown in Fig. 4.5 and eqn (4.1). The negative exponent of Ca agrees with the fact that the viscous force favors the inner phase pinch-off and decrease the droplet size, while interfacial tension holds back the inner phase and acts against its pinch-off and increases the droplet size.

$$d/D_O = 0.15(\alpha \cdot Ca \cdot \cos\theta)^{-0.29} \tag{4.1}$$

The mechanism is a little different in the second series of experiments. When we keep increasing the inner aqueous phase flow rate, the Reynolds number of inner phase approaches unity, which means the inertia of inner phase is comparable to the viscous force, and thus we cannot ignore this inertia in this case. Therefore, we must add Re to our scaling law here, as depicted in Fig. 4.6 and eqn (4.2),

Here $Re = \rho_I U_I D_I/\mu_O$, where ρ_I is the density of inner phase, D_I is the inner channel diameter, and $U_I = Q_I/(\pi D_I^2/4)$ is the inner phase flow velocity in the inner channel. The positive exponent of Re agrees with the fact that the inertial force

increases the inner phase pinch-off time and thus increases the droplet size.

$$d/D_O = 0.50[Re/(\alpha \cdot Ca \cdot \cos\theta)]^{0.11} \tag{4.2}$$

As we described in the introduction, successful double emulsion production in microfluidic device has made a great advance in droplet-based microfluidics. Conventionally fabricated 2D channels usually requires delicate control of wall wetting conditions: One segment of the channel wall is made hydrophobic and the other segment is made hydrophillic. Researchers have to locally modify the wettability of the channel walls for every single chip. This process is always complicated and is unfavorable for further applications in the industry, where mass production with simple and rapid fabrication processes are required. To highlight this point, we extend our single 3D junction to two sequential 3D junctions to generate double emulsions where even more complicated wetting conditions must be maintained. Generated double emulsions are shown in Fig. 4.2 (c), (d) and (e), demonstrating that different double emulsions can be produced by the same chip without any surface treatment of the channel walls. This extension from single 3D junction to two sequential 3D junctions is quite easily achieved through 3D printing technology. However, it is not easy to make this extension using current traditional fabrication techniques. This again demonstrated the flexibility and convenience of 3D printing technology. The liquids we used to generate both modes of double emulsions are listed in Table 4.1. To the best of our knowledge, this is the first time that different double emulsions can be both produced in the same flow-focusing structure.

An important application for emulsions in microfluidic device is to produce functional particles based on emulsion templates [174]. Variety of chemical reagents are dissolved in either the aqueous phase or oil phase. Therefore, researchers must use different microfluidic devices to generate different droplet templates (water or oil) for functional particle production. Now this low-cost printed chip can be used to produce

functional particles based on both water and oil droplet templates without need for changing the chips. Here W/O emulsions are used as templates to produce magnetically responsive microspheres, to demonstrate a potential application for chemical and material engineering. The inner disperse phase consists of Poly(ethylene glycol) diacrylate precursor solution (Sigma-Aldrich), together with 5% (v/v) 20 nm nanomagnetic particles solution (Micromod Partikeltechnologie GmbH.) and 2 wt% 2,2-dimethoxy-2-phenylacetophenone (Sigma-Aldrich) as photoinitiator, while the outer continuous phase is 100 cSt silicone oil. Droplets containing nanomagnetic particles are irradiated under UV light for about 5 minutes for polymerization, to form magnetically responsive microspheres. Fig. 4.7 shows how these magnetically responsive microspheres are attracted to the edge of petri dish from the center by a magnet.

4.4 Conclusion

In this chapter, we present a design and fabrication of 3D miniaturized fluidic emulsion generator using 3D printing technology. The advantage of having a truly 3D junction, is that unfavorable wettability of the channel-walls does not prevent the emulsion formation.

This 3D junction will be quite complicated and expensive to fabricate using traditional fabrication techniques, but can be easily, rapidly and inexpensively fabricated using the 3D printing method. For the first time, both W/O/W and O/W/O double emulsions can be produced in the same flow-focusing structure without modifications or additional wall wettability treatments. The excellent transparency of our chips is highly favorable for observation and various microfluidic applications requiring optical access.

Uniform scaling laws for both emulsion (W/O and O/W) drop sizes generated in our 3D emulsion generator are successfully proposed for the first time, which pro-

vides an excellent prediction and guidance for researchers to produce different sizes of droplet templates for variety of applications using similar 3D flow structures. Our design can be easily extended with more sequential 3D junctions for even higher-order emulsions or be paralleled to produce an emulsion generator array to increase the production rate, which is attractive in the industry field.

We also presented the production of magnetically responsive microspheres based on droplet templates, as an example of functional particle production, showing the great potential of our emulsion generator for chemical and material applications.

3D printing technology is undergoing a rapid development currently. More importantly, this 3D geometry achieved here can be easily extended in a modular manner, which will enable us to produce higher-order composite emulsions regardless of channel wettability. We believe that more and more complex miniaturized fluidic devices will soon be easily fabricated using 3D printing technique with higher resolution and faster speed.

Chapter 5

Droplet Generation In Cross-flow With Cost-Effective 3D-Printed Plug-and-Play Microfluidic Devices

5.1 Introduction

In previous chapter, we have applied 3D printing technology to fabricate fully 3D-printed microfluidic devices for emulsion generation. It provides a simple, rapid and low-cost alternative method for fabrication of microfluidic devices. However, the relatively large channel dimension has limited its usage in droplet microfluidics.

The difficulty of the removal of the uncured resin or other support material from small channels due to the capillary effect, has not been well resolved. Although the layer resolution of current desktop printers can achieve 50 μm or even finer, the actually printed channel dimension (feature size) has only reached 250 $\sim$ 300 μm in the best case [168], which is an order of magnitude larger compared to the resolution of printer itself. In addition, the channel with this limited dimension cannot be long or complex, which will increase the risk of channel clogging due to uncured materials, which are easily left inside such long or complex channels. Resulting from the rela-

tively large dimension of channels, 3D-printed channels are not capable of producing droplet with sizes comparable to the sizes of those produced in conventional microfluidic devices [175]. This hinders the full implementation of 3D printing technology in droplet-based microfluidics.

Herein we propose a novel design of 3D-printed plug-and-play devices for the generation of monodisperse droplets with sizes comparable to those generated in current microfluidic devices. The device consists of a 3D-printed channel with an embedded screw thread to connect a commercial fitting. This fitting contains an inserted commercial tubing which can be easily replaced according to user's requirement. The inserting depth of the tubing depends on our design, which can be accurately controlled. By combining the tubing to the channel, the feature size of our device where the droplets are generated can reach down to ~ 100 μm with 100% yields. This is the smallest size achieved in current 3D-printed microfluidic devices printed by desktop printers. Different emulsions, Water-in-Oil (W/O) and Oil-in-Water (O/W), can be generated using different tubings.

5.2 Methods

3D-printed microfluidic devices were designed using Solidworks (Dassault Systemes S.A.), and then printed with a low-cost commercial printer Form 1+. This desktop printer is based on the stereolithography (SLA) technique to build structures [176] and only costs $2799, which is affordable and could become widespread in most laboratories. A major advantage of SLA is the high precision of the surface resolution, due to the process of photo-curable resin exposed by a UV laser. This makes SLA a good candidate for fabrication of droplet-based microfluidic devices since a smooth channel surface is crucial for droplet creation and their transportation inside the microchannel. Another benefit of SLA lies in the availability of clear resin, which

provides an excellent transparency after being polished appropriately and thus allows researchers to observe the internal fluid flow such as droplet generation. This is crucial for many microfluidic applications requiring optical access. This clear resin contains modified acrylate oligomer and monomer, together with a photoinitiator and their weight ratio is proprietary.

In addition, the Young's modulus of postcured clear resin is 2.7 Gpa, much larger than that of PDMS: 0.75×10^{-3} Gpa. Therefore, our devices, printed by this material, are capable of withstanding higher liquid flow rate and input pressure, which leads to benefits such as the increase of the droplet generation frequency and reduction of the droplet sizes.

The basic design of our device is illustrated in Fig. 5.1(a) and (b). A screw-thread was designed and printed to allow the connection of a commercial 1/16 inch fitting for holding a commercial tubing (1/16 inch OD), through which the dispersed phase flows. Following the thread, a cone structure was printed for sealing the cone fitting. Next, a tubing chamber was fabricated for accommodation of commercial tubing. This chamber was cylindrical with diameter 1/16 inch ($\sim$ 1.6 mm), matched to the tubing OD. The final height of chamber depends on our design, which determines the tubing position inside the main channel. This main channel with a square cross-section was printed with a width dimension of 1 mm, through which the continuous phase was introduced. Thus, a small gap between the chamber and the main channel was constructed, as shown in Fig. 5.1(b). Then the tubing was inserted into this champer, enclosed by fitting and thread. Finally, the dispersed phase was pinched off at this small gap between the tubing and the channel wall. The channel can be printed in relatively large dimensions with little effects on droplet size, since droplets are generated in the small gap instead of in the main channel. The uncured resin between this small gap can be easily removed through this chamber since this chamber structure acted as a resin released hole. Our design overcomes the limitation that

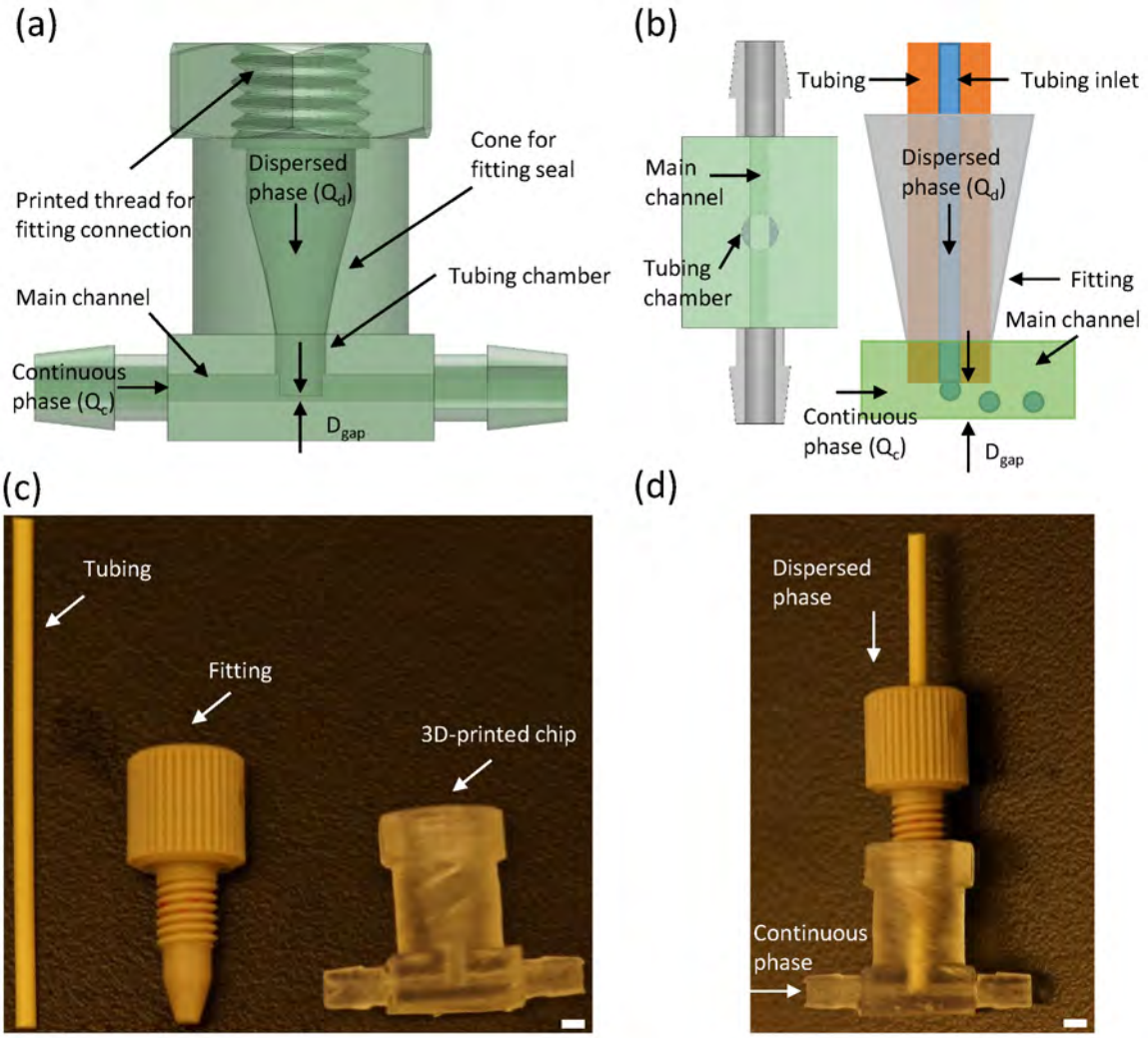

Figure 5.1: Schematic of a 3D-printed emulsion generator with (a) side view and (b) bottom view. The dispersed phase (Q_D) is introduced through a tubing with fitting connected within the printed thread. The continuous phase (Q_c) flows in the main channel. The droplet is generated in a small gap with designed height 300 μm. (c) A commercial tubing (1/16 inch OD) and fitting along side the 3D-printed chip. (d) Assembly of the full device consisting the tubing, the fitting and the 3D-printed generator. All scale bar are 1 mm.

small feature size in 3D-printed devices is difficult to achieve. The dimension of small gap here which we can print is close to the layer resolution set by our desktop 3D-printer, *i.e.* 100 μm.

Silicone oils (Sigma-Aldrich Corp.) with different viscosities were used as the continuous oil phases, and water-glycerin mixtures of different viscosities were used as the dispersed aqueous phases. Tetradecane was used as the dispersed oil phase. Red dyes were applied in the aqueous phase to enhance observation, as well as Sudan red was used in the oil phase. The surfactant Tween 20 (Sigma-Aldrich Corp.) was used in the aqueous phase, whereas the surfactant Dow Corning 749 (Dow Corning Corp.) was used in the oil phase. The interfacial tension between aqueous phases and oil phases were measured using a tensiometer (Kruss GmbH) and the values are listed in table 5.1, for all the liquids used in the present study. The difference of interfacial tension between specific water/glycerin mixtures with different viscosities of silicone oils is negligible, so 100 cSt silicone oil was used for measuring the interfacial tension.

Table 5.1: Liquids used in the experiments

Aqueous phase (water/glycerin mixture)	Oil phase (silicone oil)	Interfacial tension	Value (mN/m)
1 cP	50 cSt	1 cP - 100 cSt	20
10 cP	100 cSt	10 cP - 100 cSt	19
100 cP	350 cSt	100 cP - 100 cSt	18

Commercial fittings and tubings as shown in Fig. 5.1 were purchased from IDEX Corporation. Syringe pumps (Fusion 200, Chemyx, Inc.) were applied for driving the fluids into the devices. The formation processes of the droplets were observed and recorded with a high-speed color CMOS video camera Photron SA-3. The sizes of the droplets were analyzed using the free image-analysis software ImageJ. Since the dimension of the main channel is 1 mm, which is much larger than the droplet sizes generated, the droplets have little deformation in the main channel and we assume their shape is spherical. All experiments were carried out at room temperature of 22

°C.

5.3 Results and Discussion

5.3.1 The generation of different emulsions

Since the droplets were generated from the inserted tubing inlet, the tubing surface wettability is crucial for producing different emulsions (W/O or O/W). The commercial tubing was treated to make it hydrophobic using a commercial coating agent (Glaco Mirror Coat 'Zero', Soft 99 Co.). W/O emulsion was first generated with the hydrophobic tubing surface, as shown in Fig. 5.2(a). Then the commercial tubing was treated to become hydrophilic using plasma. O/W was generated with the hydrophilic tubing surface, as shown in Fig. 5.2(b). Both W/O and O/W emulsions were produced in a highly monodisperse manner. One benefit with this setup is that only the tubing needs to be replaced for producing different emulsions and the channel wall does not need surface treatment. Thus, different emulsions can be generated in the same microfluidic generator without additional surface treatment for the generator.

5.3.2 Flow-pattern

The flow pinch-off dynamics was controlled in the dripping regime in the present study. Unlike the microfluidic T-junctions [**?**], where the jetting regime is observed in other studies [177, 178], there is no jetting regime in our device even when the flow rate of dispersed phase is large. Instead of the jetting regime, the dispersed phase will attach to the tubing surface at the back area of the tubing, where a stable liquid cone is formed and pinches off to generate monodisperse droplets with larger sizes, as shown in Fig. 5.2(c). The velocity of the continuous phase flow at the backside of the tubing is much lower than that in the gap, and thus less viscous stresses are exerted

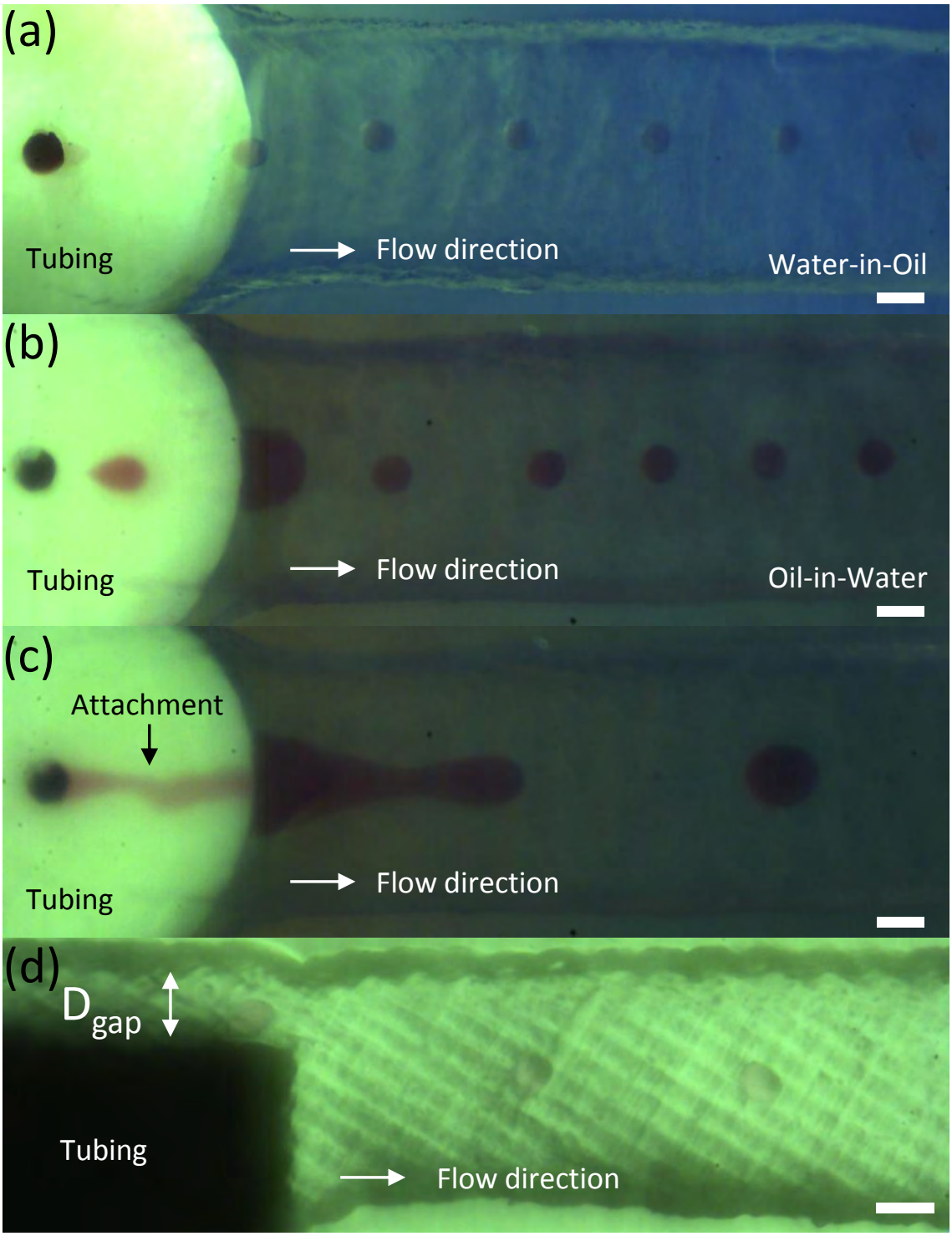

Figure 5.2: Droplet generation in our 3D-printed device. (a) Aqueous droplets generation. (b) Oil droplets generation. (c) The dispersed phase attaches the tubing wall due to the large flow rate of the dispersed phase. (d) Side view of the printed device. The real printed gap distance (D_{gap}) is 262 μm with the designed gap distance 300 μm. All scale bars are 200 μm.

on the dispersed phase at the back of the tubing. So larger droplets were generated during pinch-off in the tubing back area. This novel regime is beyond the scope of the present study and will be discussed in details in the future.

5.3.3 Geometry effects

The geometry parameters including the tubing inside diameter (ID) and the gap distance (D_{gap}) have influence on the droplet sizes. Smaller droplets can be produced with smaller tubing ID or smaller D_{gap} [179]. The main channel dimension has little influence on the drop sizes because the droplet are generated in the gap area instead of the main channel. The droplets were all generated with the same tubing ID (177 μm) in the present study. As shown in Fig. 5.2(d), the gap distance we obtained here is 262 μm, compared with the design distance 300 μm. The actual channel dimension is usually smaller than the design due to incomplete removal of resin residues. The smallest D_{gap} with 100% yields using our low-cost desktop printer Form 1+ is 115 μm, with the design distance of 150 μm, which is closed to the layer resolution we set in this 3D-printer. Droplets with a diameter of 56 μm can be generated with this smallest gap distance even if the tubing ID (177 μm) is much larger than the droplet sizes.

5.3.4 Fluid analysis

W/O emulsions are used for the fluid analysis in the following sections. Other than using different viscosities of continuous phases, different viscosities of dispersed phase were also used for altering the viscosity ratio in the present study. The dimensionless droplet sizes are scaled by the tubing ID. First, we investigated the flow rate ratio (Q_d/Q_c) effects on the generated droplet sizes. As shown in Fig. 5.3, the droplet sizes increase overall with increasing the flow rate ratio. In other words, when the flow rate of the continuous phase is reduced, the droplets become larger.

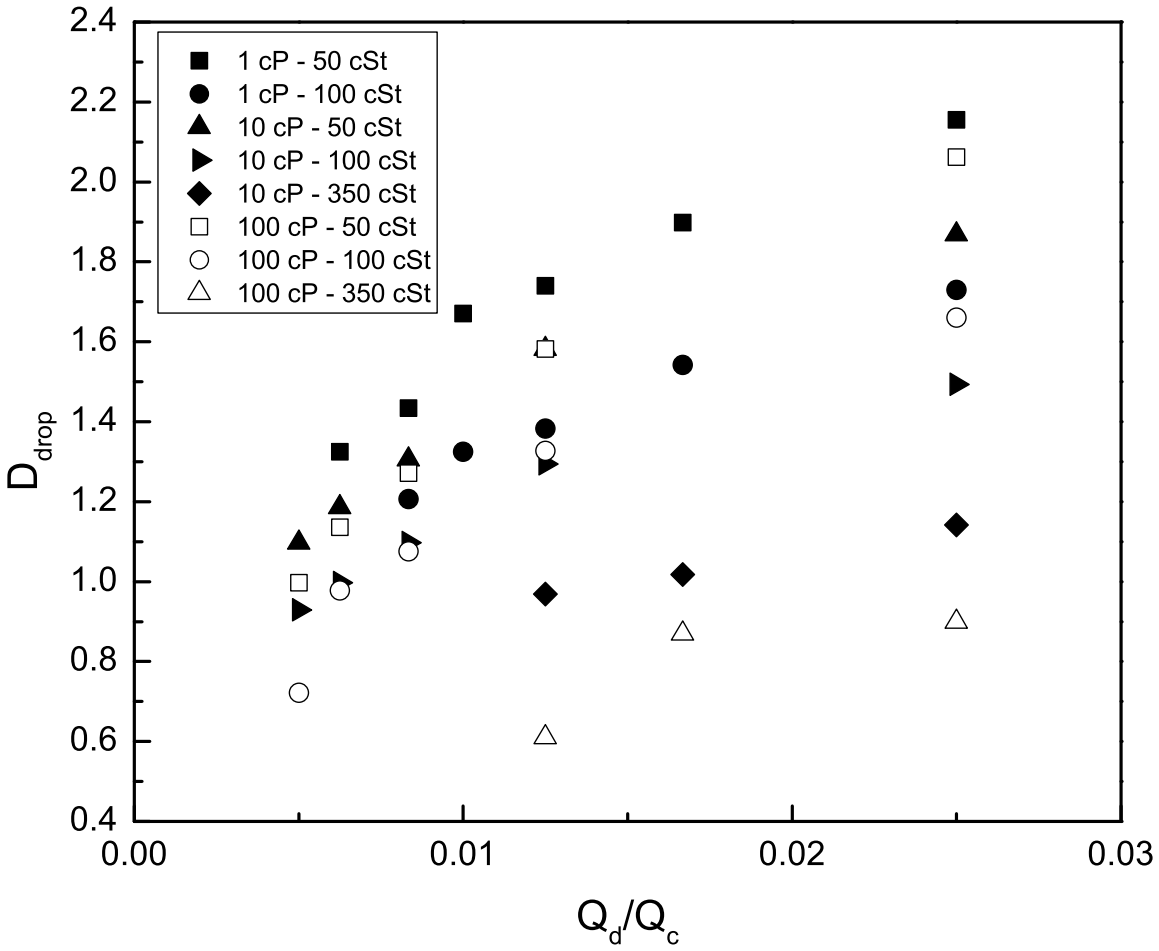

Figure 5.3: Dimensionless droplet size with variation of flow rate ratio. The dispersed flow rate (Q_d) is kept constant 5 μL min^{-1}. The continuous flow rate (Q_c) is altered from 200 μL min^{-1} to 1000 μL min^{-1}. The drop sizes increase with increasing the flow rate ratio, i.e. when the flow rate of the continuous phase is reduced, the droplet become larger.

At the same flow rate ratio, smaller droplets were generated with more viscous continuous phase. Surprisingly, smaller droplets were also generated with more viscous dispersed phase. The experimental results show that not only viscosity ratio has influence on the droplet size, but the viscosity of dispersed phase can also affect the droplet size. The reason for the variation of the droplet size with different viscosity ratio is still unclear. For more viscous continuous phase, more viscous stresses are exerted on the droplet interface at the same flow rate ratio. Thus, the dispersed phase is more easily pinched off with more viscous stresses and this causes smaller droplets being generated. Few studies involving the effects of the viscosity of the dispersed phase, on droplet sizes, have been reported. Higher liquid viscosity can result in greater deformation, which stretches out the dispersed phase from the tubing into a filament before this filament ruptures. Therefore, less of the liquid supply results in the smaller droplets.

The droplet pinch-off process results from the balance of the viscous stresses, interfacial tension and squeezing pressure [180]. The capillary number Ca describes the relative magnitude of the viscous forces compared with the interfacial forces. Here we define Ca in terms of the average velocity (u_c) of the continuous phase flow within the narrow gap:

$$Ca = \frac{\mu_c u_c}{\sigma} = \frac{\mu_c Q_c}{\sigma D_{gap} w} \tag{5.1}$$

μ_c is the viscosity of the continuous phase, σ is the interfacial tension and w is the main channel width, $w = 1$ mm in all experiments. The droplet size was scaled by the tubing ID (177μm) and thus we obtain the dimensionless droplet size (D_{drop}). We plot D_{drop} as a function of Ca in Fig. 5.4. As shown in Fig. 5.4, the droplet sizes decrease with increasing Ca. This trend is consistent with other studies on microfluidic T-junction [177, 180]. We observed the variation of the droplet sizes with Ca over the entire range (10^{-2} to 10^{0}) in our experiments. In Fig. 5.4, we find

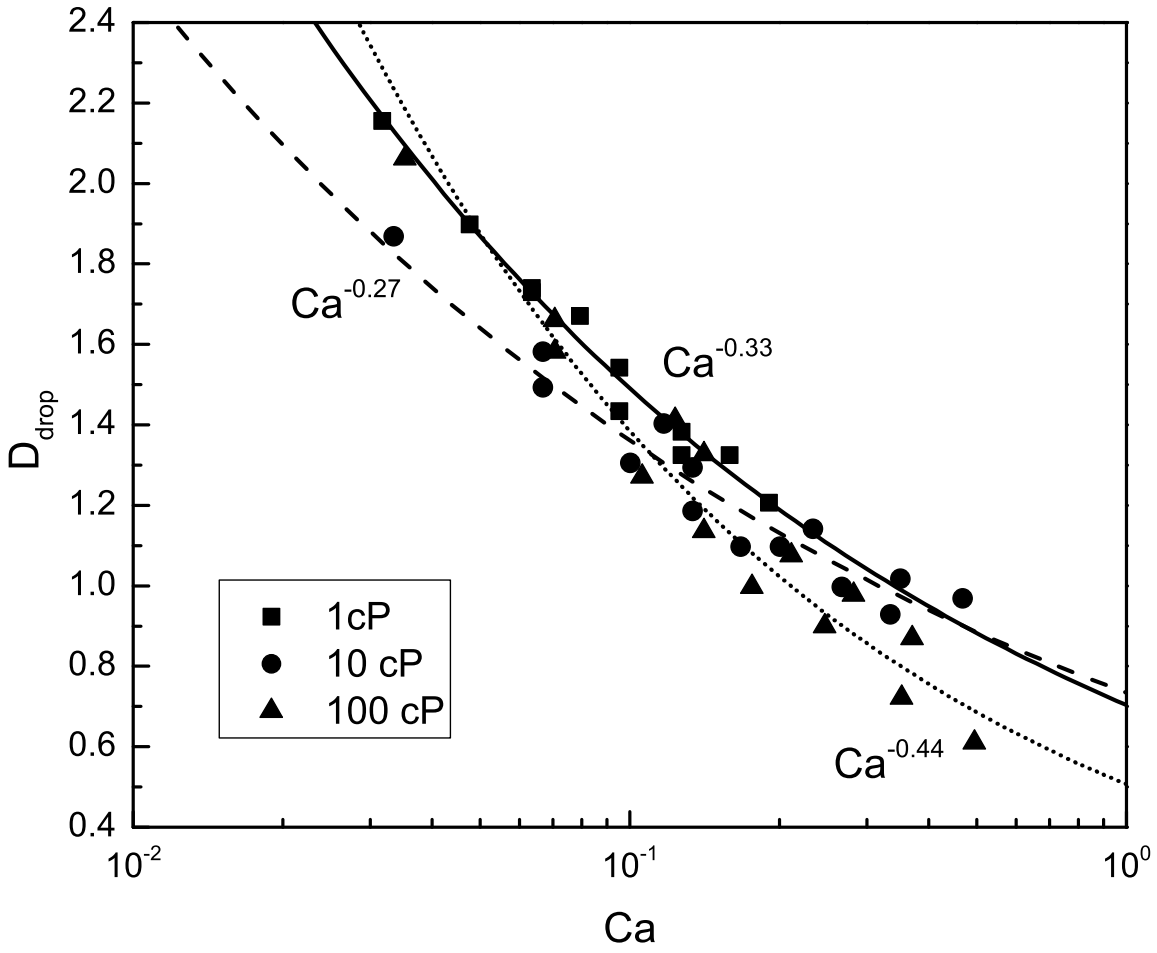

Figure 5.4: Dimensionless droplet size as a function of capillary number with different viscosities of the dispersed and continuous phases. The dispersed phase used here is 1 cp, 10 cP and 100 cP, respectively. The curve of 100 cP dispersed phase has a larger slope.

that the droplet size exhibits a power-law dependence on *Ca*. For 1 cP and 10 cP of the dispersed phase case, the exponent is -0.33 and -0.27. This value agrees with the value given in other studies in microfluidic T-junctions ($\sim -1/3$) [**?**, 180]. But for 100 cP of the dispersed phase case, the curve has a larger slope with exponent -0.44.

The flow rate ratio in Fig. 5.3 is up to 0.025. For the following case, Q_c was kept constant as 200 μL min^{-1} and the viscosity of the continuous phase was kept constant as 350 cSt. The flow rate of the dispersed phase is kept increasing from 10 μL min^{-1} to 50 μL min^{-1}, which makes the flow rate ratio higher. in Fig. 5.5, we plot D_{drop} with variation of higher flow rate ratio. It shows the droplet size increases

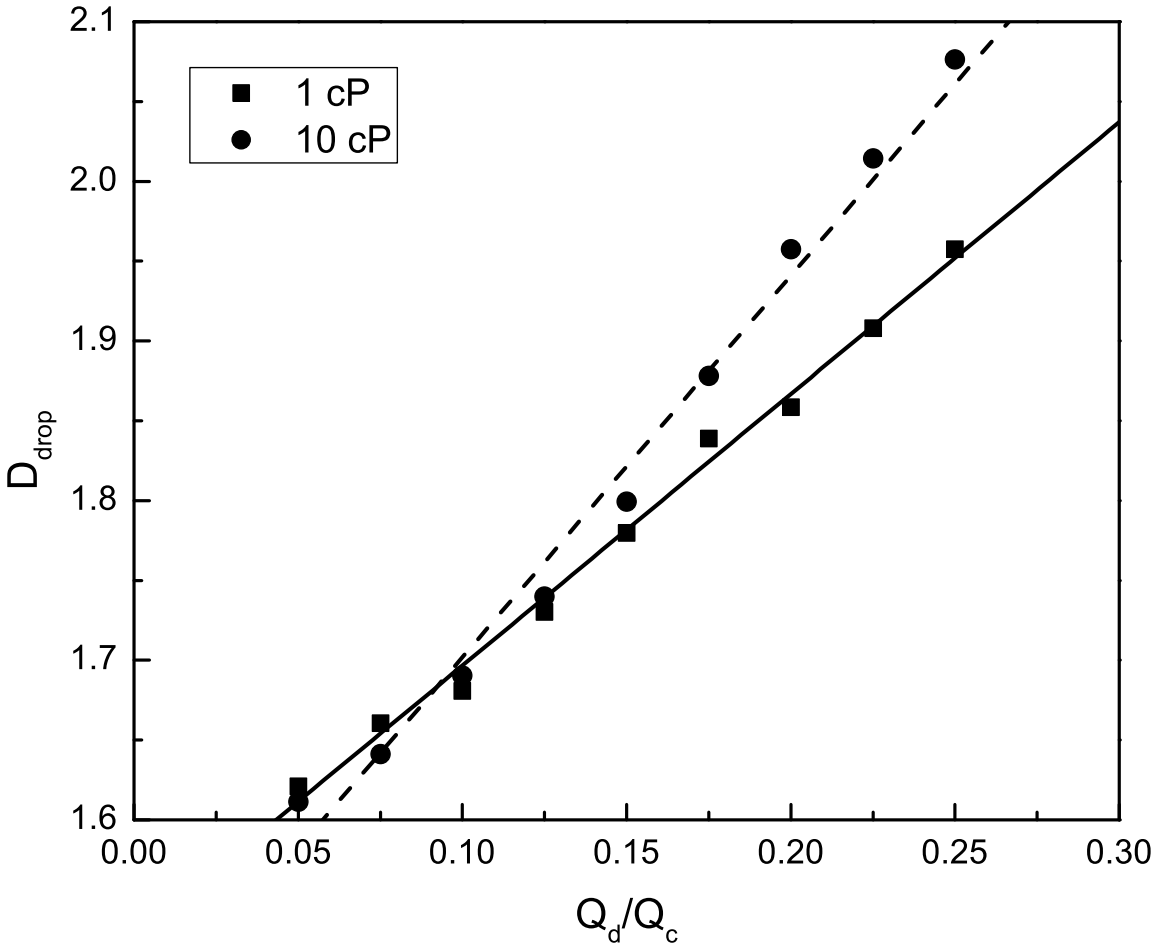

Figure 5.5: Dimensionless droplet size with variation of flow rate ratio. Q_d is altered from 10 μL min^{-1} to 50 μL min^{-1}, while Q_c is kept constant at 200 μL min^{-1}. The viscosity of the continuous phase is kept constant at 350 cSt and the viscosity of the dispersed phase used here is 1 cP and 10 cP, as marked by the different symbols. The curve of higher viscosity of dispersed phase has a larger slope.

with increasing the flow rate of the dispersed phase. This is consistent with droplet generation in microfluidic T-junctions. Droplet sizes depend not only on the flow rate ratio, but also on the flow rate of the dispersed phase. The curve of higher viscosity of dispersed phase has a larger slope. More specifically, the droplet sizes exhibit a linear relation dependence on the flow rate ratio. Notice that over the range of flow rate ratio in Fig. 5.5, the droplet sizes exceed the gap distance (D_{gap}). This is similar to the squeezing regime reported in microfluidic T-junction [178]. The droplet starts to block the continuous phase flow in the gap in vertical direction, and the squeezing pressure play a role in this regime. In this case, the droplet sizes mainly depend on the flow rate ratio instead of Ca.

Few studies on droplet generation frequency in microfluidic T-junctions have been reported [177, 180]. In Fig. 5.6, we plot the droplet generation frequency as a function of flow rate ratio with different viscosity ratio of liquid phases. At the same flow rate ratio, more viscous continuous phase or more viscous dispersed phase causes larger generation frequency. From the view of mass conservation, one can calculate the frequency if Q_d and droplet size is known. We see that smaller droplets are generated with more viscous continuous phase or with more viscous dispersed phase and the flow rate of the dispersed phase is kept constant. Thus, the higher generation frequency results from the smaller droplet sizes when the flow rate of the dispersed phase is constant. In addition, in Fig. 5.6, we find that the droplet generation frequency exhibits a power-law dependence on the flow rate ratio. The power-law exponent lies in a narrow range from -1.1 to -1.4, which has not yet been reported in other studies.

One big advantage of 3D printing technology is to allow researchers to design and integrate different functional parts in a modular manner. Therefore, we have designed and fully 3D-printed two functional parts which can be integrated with our droplet generator for further droplet-based applications. These functional parts were also printed with our low-cost desktop printer and are introduced in the following section.

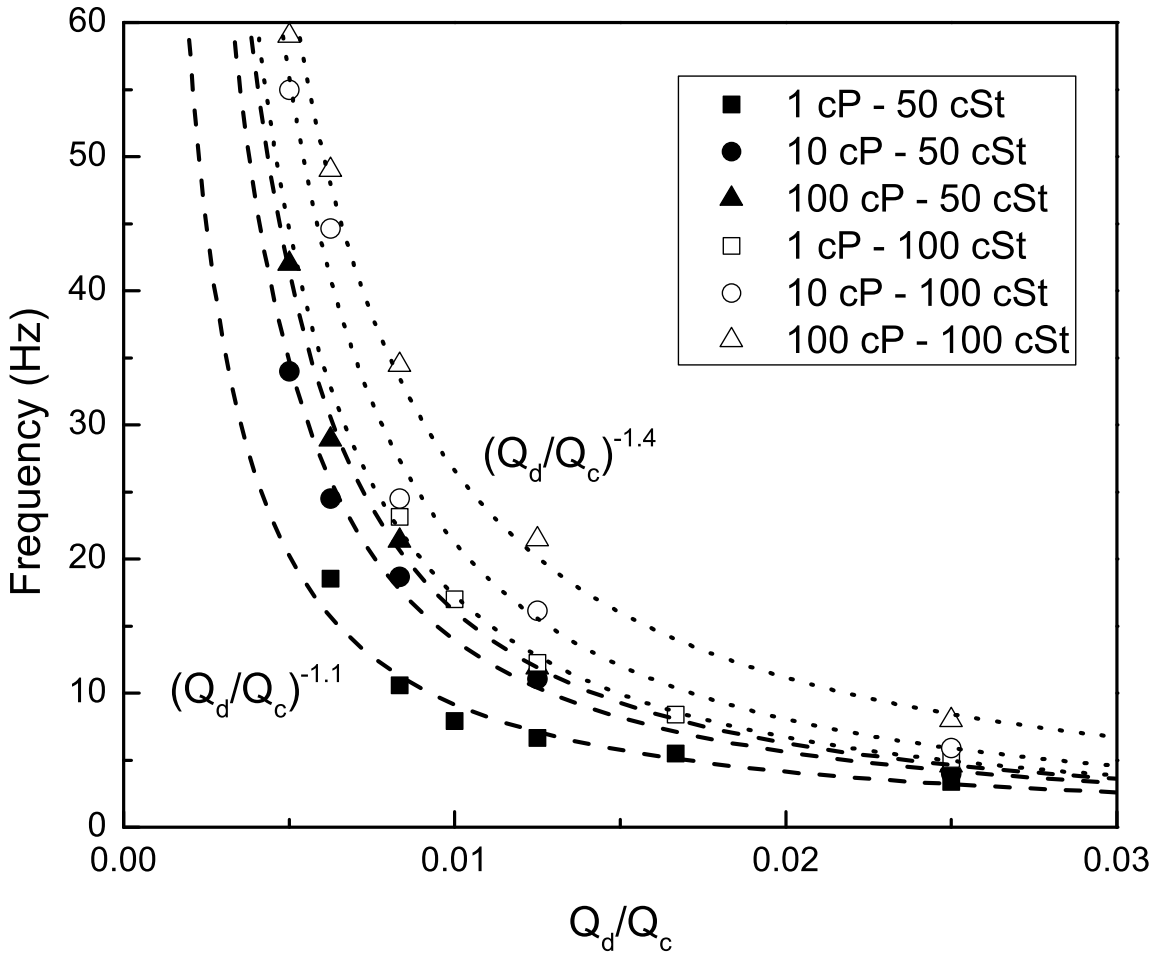

Figure 5.6: The frequency of droplet generation as a function of flow rate ratio with different viscosities of the dispersed and continuous phases. The curves are power-laws with exponents between -1.1 to -1.4.

5.3.5 Parallel droplet generation with different concentrations

The concentration of reagents is one of the most important parameters in chemical or biological libraries [181], but the ability to control and vary the concentration of reagents still remains a challenge in microfluidic research [182]. To vary the concentration usually requires complex fluid networks, but other functional structures also have to be integrated into the same layer of the chip, due to current planar fabrication methods. It is not possible to integrate too many channels in one layer. Thus, multi-layered chips have been needed to achieve multiple functions. However, the increased

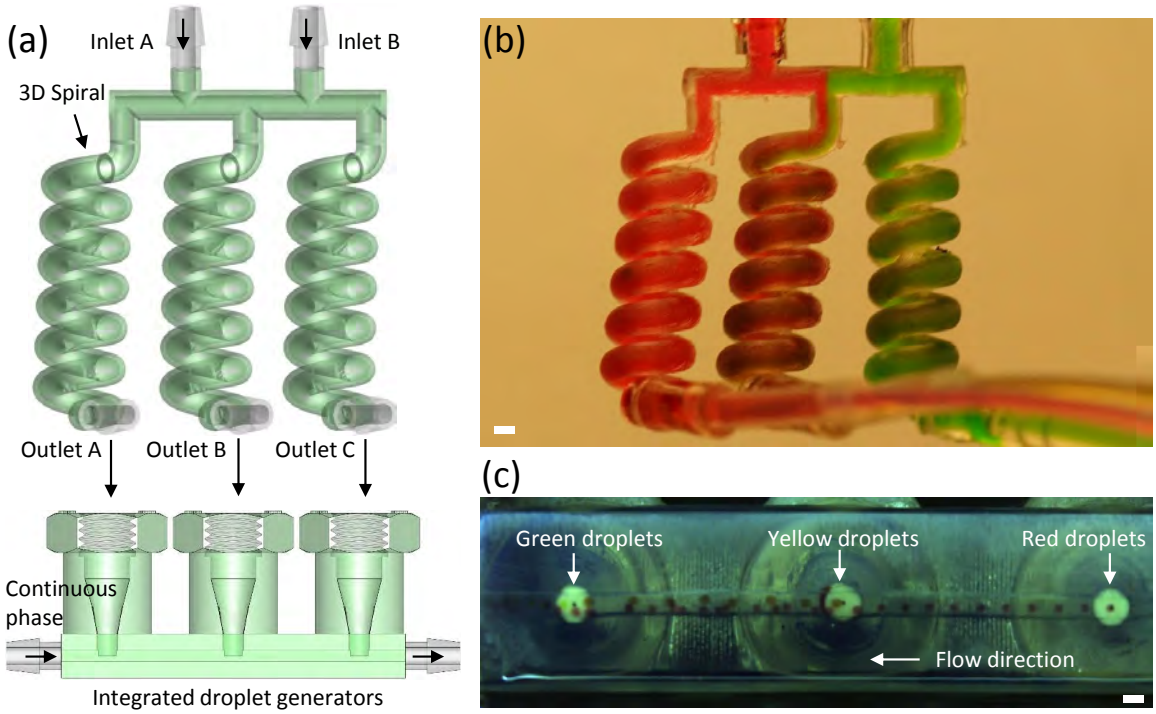

Figure 5.7: (a) Schematic of a 3D-printed gradient concentration generator. 3D spirals facilitate mixing. (b) The printed gradient concentration generator. 10 cP water/glycerin mixtures with red and green dyes were introduced through two inlets, respectively. (c) Photograph of droplet generation with different color (red, yellow and blue). All scale bar is 1 mm.

the complexity of fabrication introduces potential problems, as any single defective part can disable the whole chip.

Here we have designed and printed a simple 3D single-level gradient concentration generator as shown in Fig. 5.7. This generator is integrated with the droplet generator to demonstrate the feasibility of producing droplets with different concentrations, which is of a great potential for chemical reactions and drug testing [183, 184]. 3D spiral channels can enhance liquid mixing compared to planar strategies. 10 cP water/glycerin mixtures with red and green dyes were introduced through two separate inlets. The red and green liquids keep their concentration in both side spiral channels while the red and green liquids are mixed in a central spiral channel, resulting in a yellow liquid at the exit. Then these three liquid streams are used as the dispersed phases

in three parallel droplet generators to produce a stream of droplets with different concentrations here represented by three colors: Red, yellow and green. Multiple-level gradient concentration generator can also be printed for obtaining more complex gradients and gradient distribution. Since the generation of both concentration gradient and droplet is separated, it is convenient for researchers to integrate these two parts independently for producing droplets with various sizes and concentration differences between droplets.

5.3.6 Droplet merging

Coalescence and merging of droplets is an important subject in microfluidics due to its wide usage in chemical and biological analyses to control chemical reactions [185]. Several techniques have been reported to merge droplets [186]. Passive strategies of merging droplets primarily involve an expanding channel which facilitates the drainage of the continuous phase between neighboring droplets. But such expansions also introduce more freedom of droplet motion, which reduces control over the merging process. Here we have designed and printed a 3D coalescence device for merging droplets passively. As shown in Fig. 5.8, the height of the channel is 1 mm and the height of guide rail is 600 μm, which forms a gap to allow the continuous phase to flow through. And also, buffer areas were designed on both sides of the guide rail to form a expanding chamber for allowing the continuous phase flow. Therefore, the continuous phase between neighboring droplets was drainage in both horizontal and vertical directions. On the other hand, the guide rail limits the freedom of drop motion. Both extra drainage of the continuous phase and limited drop motion freedom greatly facilitates the droplet merging. As shown in Fig. 5.8(c), two droplets (one green and the other red) from two droplet generators move through the merging channel and they approach each other in the merging channel due to the drainage of the continuous phase in the expanded merging channel. Finally these droplets merged at

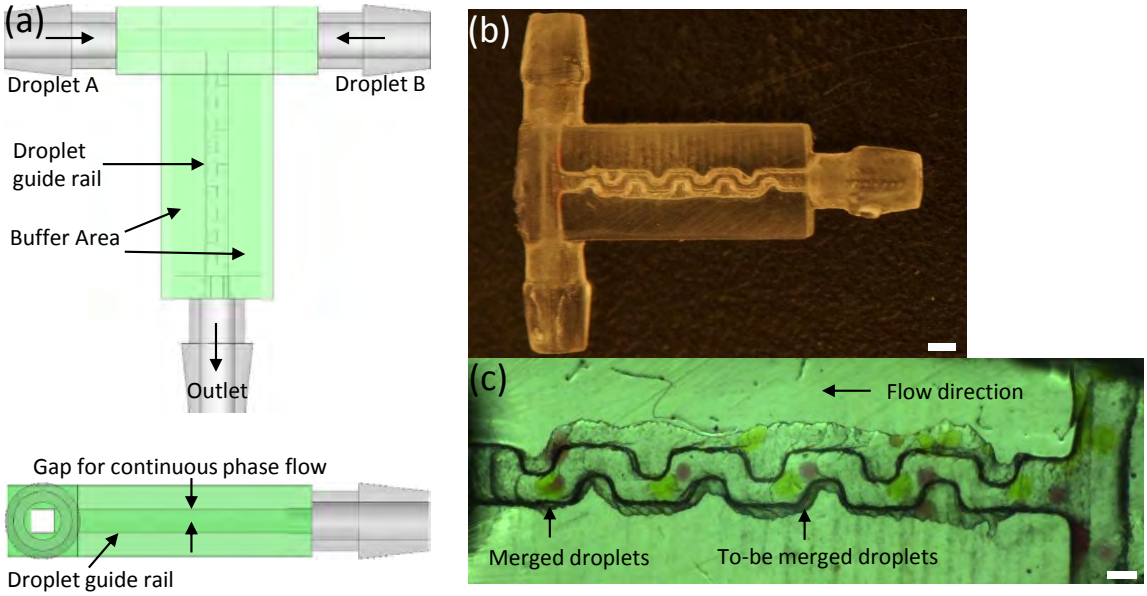

Figure 5.8: (a) Schematic of a 3D-printed droplet merging device. (b) The printed droplet merging device. Scale bar is 1 mm. (c) Photograph of droplet merging processes. Scale bar is 500 μm.

the end of the merging channel.

5.4 Conclusion

In the present chapter, we designed and 3D-printed a plug-and-play microfluidic droplet generator. Commercial tubings and fittings were used for the dispersed phase input channel. A screw thread was printed for connecting the tubing sufficiently tight for droplet generation without leakage. The tubing can be easily replaced with different tubing ID or surface wettabilities, to generate various sizes of droplets or different emulsions (W/O and O/W).

Subsequently we performed fluid analysis on the droplet sizes and generation frequencies in our devices, to guide other users using such devices to fulfill their requirements. We find that the droplet sizes depend on liquid flow rate ratio, Ca, and viscosity ratio, which is consistent with other studies in microfluidic T-junctions. But the scaling law is a little different due to differences in our geometry structures. And

also, the experimental results show that the viscosity of the dispersed phase can also influence the droplet sizes and frequency of generation.

Finally, we have designed and 3D-printed a gradient concentration generator for droplet with different concentration, which can be beneficial to chemical reactions and drug testing. In addition, we also made a droplet merging device for droplet coalescence and mixing, which can be useful in chemical and biological applications.

We demonstrate that not only droplet generators can be fabricated using 3D printing technology, but more complex devices can be made in a modular way and integrated with the droplet generator to achieve more complex functions based on droplet templates. More droplet-based applications can be developed using 3D printing technology in the future.

Chapter 6

Conclusion and Future Work

We have presented and fabricated several novel designs of microdroplet/microbubble generation microfluidic devices. First, a full-glass microfluidic device for multiple emulsion generation is introduced. The advantages of this method lies in a simple fabrication procedure, inexpensive processing equipment, and flexibility in the surface modification of the designed microfluidic devices. Double emulsions including W/O/W and O/W/O and even higher order of multiple emulsions including O/W/O/W and (Gas+W)/O/W can be easily generated in this simple glass microfluidic device, which can be fabricated in less than 30 minutes and the whole cost is below one US dollar. The advantages of glass microfluidic devices for generation of emulsions, especially the ability for generation of complex multiple emulsions are still unmatched.

Second, we propose a novel glass capillary microfluidic device to generate microbubbles as small as 3.5 μm, with high monodispersity. Currently reported methods for generation of such small microbubbles inevitably include a very narrow channel section comparable to the size of microbubble through which the gas/liquid must flow. This is required in order to acquire high shear stress to pinch off the gas flow for producing microbubbles with similar size. This small section is difficult to fabricate and can easily be clogged. The narrowest section along the liquid-phase path in our device has a dimension of 75 μm, much larger than those in other designs

($\sim 7\mu$m) [136], which greatly suppresses clogging problems and reduce the difficulty of fabrication.

Next, a fully 3D-printed microfluidic device for generation of double emulsions is reported. This approach has a bright future, especially in light of the rapid development of 3D printing technology, with the rapidly reducing cost of 3D printers over the last two years. Various low priced desktop 3D printers are available on the current market, which allows researchers to use 3D printing technology to fabricate microfluidic devices with fully 3D structure. Therefore, we designed a non-planar structure for generation of double emulsions in the same single chip without need for additional surface treatment. This device was printed using a low-cost desktop commercial 3D printer costing about $ 2000. The 3D printing of microfluidics offers the opportunity to shrink the time from design to realization of a functional device to an hour or less. This offers a true rapid-prototyping ability to positively disrupt the microfluidics development cycles.

Furthermore, we take a step forward on 3D-printed microfluidic devices for generation of emulsions. One of the limitations of 3D-printed microfluidic devices is the relatively large channel dimensions, due to the difficulty to removal of uncured resin in a small channel. We reported a novel design where the feature-size of the flow structure can be reduced to 100 μm, whereas the smallest feature size of currently available 3D-printed microfluidic devices is around 250 μm. The reduction of feature size of the flow structure reported here can result in smaller droplets generated by introducing more shear forces, which is comparable to the droplet sizes generated in soft lithography techniques. In addition, functional 3D-printed devices based on droplet templates have been developed, such as the generation of droplets with different concentrations and droplet-coalescence devices.

Finally, we investigate the scaling law for prediction of emulsion and microbubble sizes based on fluid parameters in all of the devices introduced in this disserta-

tion. This provides a good guide for other users to choose the appropriate device-characteristics for their desirable sizes of droplets and microbubbles for their individual purpose.

All of our efforts focus on design and fabrication of simple, rapid and low-cost microfluidic devices. Different types of devices have been tested and the experimental results demonstrated the feasibility of producing monodisperse emulsions and microbubbles in our reported microfluidic devices.

The future work should move forward to "downstream", which involves control and manipulation of droplets and microbubbles in emergent microfluidic devices, since we have already developed several novel devices for droplet and microbubble generation ("upstream"). For example, drop coalescence within 3D structure of 3D-printed devices, drop on-demand generation within 3D-printed devices integrated with other devices, and also, relentless efforts on producing smaller droplets and microbubbles with higher generation frequency to satisfy industrial requirements. In addition, synthesis of novel functional particles based on droplet templates should be another ongoing research topic in the future, which will develop more functional devices such as sensors and actuators based on these novel functional particles. Another area which we have applied the emulsion-generation devices is to study impact and splashing of composite drops. Fig. 6.1 shows an example.

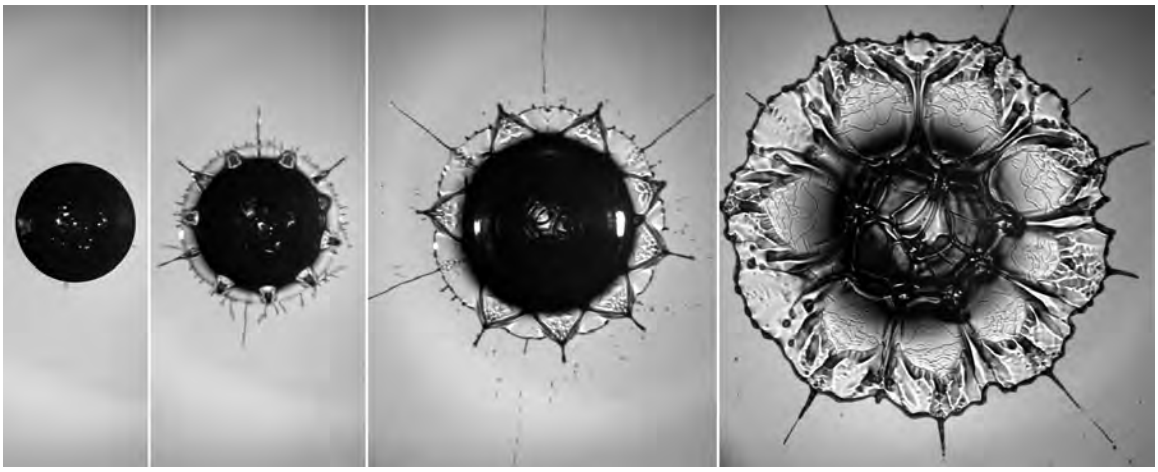

Figure 6.1: The impact of a compound drop, with outer drop of viscosity 2 cP and containing 20 inner PP1 droplets, for impact velocity V $\simeq$ 4 m/s, drop D $\simeq$ 4 mm. Frames are shown at $t = 0, 0.08, 0.25, and 0.8$ ms after first contact.

REFERENCES

[1] G. M. Whitesides, "The origins and the future of microfluidics." *Nature*, vol. 442, no. 7101, pp. 368–73, Jul. 2006.

[2] A. J. DeMello, "Control and detection of chemical reactions in microfluidic systems." *Nature*, vol. 442, no. 7101, pp. 394–402, Jul. 2006.

[3] D. B. Weibel and G. M. Whitesides, "Applications of microfluidics in chemical biology." *Current opinion in chemical biology*, vol. 10, no. 6, pp. 584–91, Dec. 2006.

[4] J. El-Ali, P. K. Sorger, and K. F. Jensen, "Cells on chips." *Nature*, vol. 442, no. 7101, pp. 403–11, Jul. 2006.

[5] P. S. Dittrich, K. Tachikawa, and A. Manz, "Micro total analysis systems. Latest advancements and trends." *Analytical chemistry*, vol. 78, no. 12, pp. 3887–908, Jun. 2006.

[6] J. Atencia and D. J. Beebe, "Controlled microfluidic interfaces." *Nature*, vol. 437, no. 7059, pp. 648–55, Sep. 2005.

[7] H. Stone, A. Stroock, and A. Ajdari, "Engineering Flows in Small Devices," *Annual Review of Fluid Mechanics*, vol. 36, no. 1, pp. 381–411, Jan. 2004.

[8] S. Neethirajan, I. Kobayashi, M. Nakajima, D. Wu, S. Nandagopal, and F. Lin, "Microfluidics for food, agriculture and biosystems industries." *Lab on a chip*, vol. 11, no. 9, pp. 1574–86, May 2011.

[9] D. J. Han, J. H. Jung, J. S. Choi, Y. T. Kim, and T. S. Seo, "Synthesis of a 3d graphite microball using a microfluidic droplet generator and its polymer

composite with core–shell structure," *Lab on a Chip*, vol. 13, no. 20, pp. 4006–4010, 2013.

[10] G. T. Vladisavljević, N. Khalid, M. A. Neves, T. Kuroiwa, M. Nakajima, K. Uemura, S. Ichikawa, and I. Kobayashi, "Industrial lab-on-a-chip: Design, applications and scale-up for drug discovery and delivery," *Advanced drug delivery reviews*, vol. 65, no. 11, pp. 1626–1663, 2013.

[11] E. M. Chan, A. P. Alivisatos, and R. A. Mathies, "High-temperature microfluidic synthesis of cdse nanocrystals in nanoliter droplets," *Journal of the American Chemical Society*, vol. 127, no. 40, pp. 13 854–13 861, 2005.

[12] R. B. Fair, "Digital microfluidics: Is a true lab-on-a-chip possible?" *Microfluidics and Nanofluidics*, vol. 3, no. 3, pp. 245–281, Mar. 2007.

[13] D. R. Link, E. Grasland-Mongrain, A. Duri, F. Sarrazin, Z. Cheng, G. Cristobal, M. Marquez, and D. A. Weitz, "Electric control of droplets in microfluidic devices." *Angewandte Chemie (International ed. in English)*, vol. 45, no. 16, pp. 2556–60, Apr. 2006.

[14] K. Churski, P. Korczyk, and P. Garstecki, "High-throughput automated droplet microfluidic system for screening of reaction conditions," *Lab Chip*, vol. 10, no. 7, pp. 816–818, 2010.

[15] D. N. Breslauer, P. J. Lee, and L. P. Lee, "Microfluidics-based systems biology," *Molecular BioSystems*, vol. 2, no. 2, pp. 97–112, 2006.

[16] J. Hong, J. B. Edel *et al.*, "Micro-and nanofluidic systems for high-throughput biological screening," *Drug discovery today*, vol. 14, no. 3, pp. 134–146, 2009.

[17] M. Seo, Z. Nie, S. Xu, M. Mok, P. C. Lewis, R. Graham, and E. Kumacheva, "Continuous microfluidic reactors for polymer particles," *Langmuir*, vol. 21, no. 25, pp. 11 614–11 622, 2005.

[18] J. I. Park, A. Saffari, S. Kumar, A. Günther, and E. Kumacheva, "Microfluidic synthesis of polymer and inorganic particulate materials," *Annual Review of Materials Research*, vol. 40, pp. 415–443, 2010.

[19] K.-S. Huang, K. Lu, C.-S. Yeh, S.-R. Chung, C.-H. Lin, C.-H. Yang, and Y.-S. Dong, "Microfluidic controlling monodisperse microdroplet for 5-fluorouracil loaded genipin-gelatin microcapsules," *Journal of Controlled Release*, vol. 137, no. 1, pp. 15–19, 2009.

[20] C.-H. Yang, K.-S. Huang, Y.-S. Lin, K. Lu, C.-C. Tzeng, E.-C. Wang, C.-H. Lin, W.-Y. Hsu, and J.-Y. Chang, "Microfluidic assisted synthesis of multi-functional polycaprolactone microcapsules: incorporation of cdte quantum dots, fe 3 o 4 superparamagnetic nanoparticles and tamoxifen anticancer drugs," *Lab on a Chip*, vol. 9, no. 7, pp. 961–965, 2009.

[21] S. A. Khan and S. Duraiswamy, "Controlling bubbles using bubblesmicrofluidic synthesis of ultra-small gold nanocrystals with gas-evolving reducing agents," *Lab on a Chip*, vol. 12, no. 10, pp. 1807–1812, 2012.

[22] S. Duraiswamy and S. A. Khan, "Droplet-based microfluidic synthesis of anisotropic metal nanocrystals," *Small*, vol. 5, no. 24, pp. 2828–2834, 2009.

[23] A. M. Nightingale, J. de Mello *et al.*, "Controlled synthesis of iii–v quantum dots in microfluidic reactors," *ChemPhysChem*, vol. 10, no. 15, pp. 2612–2614, 2009.

[24] Y. Zhao, H. C. Shum, H. Chen, L. L. Adams, Z. Gu, and D. A. Weitz, "Microfluidic generation of multifunctional quantum dot barcode particles," *Journal of the American Chemical Society*, vol. 133, no. 23, pp. 8790–8793, 2011.

[25] A. S. Utada, E. Lorenceau, D. R. Link, P. D. Kaplan, H. A. Stone, and D. A. Weitz, "Monodisperse double emulsions generated from a microcapillary device." *Science*, vol. 308, no. 5721, pp. 537–41, Apr. 2005.

[26] W. J. Duncanson, T. Lin, A. R. Abate, S. Seiffert, R. K. Shah, and D. A. Weitz, "Microfluidic synthesis of advanced microparticles for encapsulation and controlled release," *Lab on a Chip*, vol. 12, no. 12, pp. 2135–2145, 2012.

[27] P. Walstra, "Principles of emulsion formation," *Chemical Engineering Science*, vol. 48, no. 2, pp. 333–349, 1993.

[28] K. Heike and S. Helmar, "Developments in the continuous mechanical production of oil-in-water macro-emulsions," *Chemical Engineering and Processing*, vol. 34, pp. 205–211, May 1995.

[29] D. J. McClements, *Food emulsions: principles, practices, and techniques*. CRC press, 2015.

[30] A. Jillavenkatesa, S. J. Dapkunas, and L.-S. H. Lum, "Particle size characterization," *NIST Special publication*, 2001.

[31] S. M. Joscelyne and G. Trägårdh, "Membrane emulsificationa literature review," *Journal of Membrane Science*, vol. 169, no. 1, pp. 107–117, 2000.

[32] R. Williams, S. Peng, D. Wheeler, N. Morley, D. Taylor, M. Whalley, and D. Houldsworth, "Controlled production of emulsions using a crossflow membrane: part ii: industrial scale manufacture," *Chemical Engineering Research and Design*, vol. 76, no. 8, pp. 902–910, 1998.

[33] S. Peng and R. A. Williams, "Controlled production of emulsions using a crossflow membrane: Part i: Droplet formation from a single pore," *Chemical Engineering Research and Design*, vol. 76, no. 8, pp. 894–901, 1998.

[34] G. Vladisavljević, I. Kobayashi, and M. Nakajima, "Production of uniform droplets using membrane, microchannel and microfluidic emulsification devices," *Microfluidics and nanofluidics*, vol. 13, no. 1, pp. 151–178, 2012.

[35] I. Kobayashi, M. A. Neves, Y. Wada, K. Uemura, and M. Nakajima, "Large microchannel emulsification device for mass producing uniformly sized droplets on a liter per hour scale," *Green Processing and Synthesis*, vol. 1, no. 4, pp. 353–362, 2012.

[36] I. Kobayashi, Y. Wada, K. Uemura, and M. Nakajima, "Microchannel emulsification for mass production of uniform fine droplets: integration of microchannel arrays on a chip," *Microfluidics and Nanofluidics*, vol. 8, no. 2, pp. 255–262, 2010.

[37] R. Dangla, S. C. Kayi, and C. N. Baroud, "Droplet microfluidics driven by gradients of confinement," *Proceedings of the National Academy of Sciences*, vol. 110, no. 3, pp. 853–858, 2013.

[38] M. R. Böhmer, R. Schroeders, J. a.M. Steenbakkers, S. H. de Winter, P. A. Duineveld, J. Lub, W. P. Nijssen, J. A. Pikkemaat, and H. R. Stapert, "Preparation of monodisperse polymer particles and capsules by ink-jet printing," *Colloids and Surfaces A: Physicochemical and Engineering Aspects*, vol. 289, no. 1-3, pp. 96–104, Oct. 2006.

[39] S.-Y. Teh, R. Lin, L.-H. Hung, and A. P. Lee, "Droplet microfluidics." *Lab on a chip*, vol. 8, no. 2, pp. 198–220, Feb. 2008.

[40] L. Mazutis, J.-C. Baret, and A. D. Griffiths, "A fast and efficient microfluidic system for highly selective one-to-one droplet fusion," *Lab on a Chip*, vol. 9, no. 18, pp. 2665–2672, 2009.

[41] L. Mazutis and A. D. Griffiths, "Selective droplet coalescence using microfluidic systems," *Lab on a Chip*, vol. 12, no. 10, pp. 1800–1806, 2012.

[42] Y.-C. Tan, J. S. Fisher, A. I. Lee, V. Cristini, and A. P. Lee, "Design of microfluidic channel geometries for the control of droplet volume, chemical concentration, and sorting," *Lab on a Chip*, vol. 4, no. 4, pp. 292–298, 2004.

[43] Y.-C. Tan, Y. L. Ho, and A. P. Lee, "Microfluidic sorting of droplets by size," *Microfluidics and Nanofluidics*, vol. 4, no. 4, pp. 343–348, 2008.

[44] E. Brouzes, M. Medkova, N. Savenelli, D. Marran, M. Twardowski, J. B. Hutchison, J. M. Rothberg, D. R. Link, N. Perrimon, and M. L. Samuels, "Droplet microfluidic technology for single-cell high-throughput screening," *Proceedings of the National Academy of Sciences*, vol. 106, no. 34, pp. 14 195–14 200, 2009.

[45] X. Niu, F. Gielen, J. B. Edel *et al.*, "A microdroplet dilutor for high-throughput screening," *Nature chemistry*, vol. 3, no. 6, pp. 437–442, 2011.

[46] T. Thorsen, R. W. Roberts, F. H. Arnold, and S. R. Quake, "Dynamic Pattern Formation in a Vesicle-Generating Microfluidic Device," *Physical Review Letters*, vol. 86, no. 18, pp. 4163–4166, Apr. 2001.

[47] D. Link, S. Anna, D. Weitz, and H. Stone, "Geometrically Mediated Breakup of Drops in Microfluidic Devices," *Physical Review Letters*, vol. 92, no. 5, pp. 1–4, Feb. 2004.

[48] G.-R. Yi, T. Thorsen, V. Manoharan, M.-J. Hwang, S.-J. Jeon, D. Pine, S. Quake, and S.-M. Yang, "Generation of Uniform Colloidal Assemblies in Soft Microfluidic Devices," *Advanced Materials*, vol. 15, no. 15, pp. 1300–1304, Aug. 2003.

[49] M. He, J. S. Edgar, G. D. M. Jeffries, R. M. Lorenz, J. P. Shelby, and D. T. Chiu, "Selective encapsulation of single cells and subcellular organelles into picoliter- and femtoliter-volume droplets." *Analytical chemistry*, vol. 77, no. 6, pp. 1539–44, Mar. 2005.

[50] S. van der Graaf, M. Steegmans, R. van der Sman, C. Schroën, and R. Boom, "Droplet formation in a T-shaped microchannel junction: A model system for membrane emulsification," *Colloids and Surfaces A: Physicochemical and Engineering Aspects*, vol. 266, no. 1-3, pp. 106–116, Sep. 2005.

[51] D. Dendukuri, K. Tsoi, T. A. Hatton, and P. S. Doyle, "Controlled synthesis of nonspherical microparticles using microfluidics." *Langmuir : the ACS journal of surfaces and colloids*, vol. 21, no. 6, pp. 2113–6, Mar. 2005.

[52] C.-X. Zhao and A. P. Middelberg, "Two-phase microfluidic flows," *Chemical Engineering Science*, vol. 66, no. 7, pp. 1394–1411, Apr. 2011.

[53] k. Wang, Y. C. Lu, J. H. Xu, J. Tan, and G. S. Luo, "Generation of Micromonodispersed Droplets and Bubbles in the Capillary Embedded T-Junction Microfluidic Devices," *AIChE Journal*, vol. 57, pp. 299–306, May 2011.

[54] J. Tan, J. Xu, S. Li, and G. Luo, "Drop dispenser in a cross-junction microfluidic device: Scaling and mechanism of break-up," *Chemical Engineering Journal*, vol. 136, no. 2-3, pp. 306–311, Mar. 2008.

[55] Y.-C. Tan, V. Cristini, and A. P. Lee, "Monodispersed microfluidic droplet generation by shear focusing microfluidic device," *Sensors and Actuators B: Chemical*, vol. 114, no. 1, pp. 350–356, Mar. 2006.

[56] L.-H. Hung, K. M. Choi, W.-Y. Tseng, Y.-C. Tan, K. J. Shea, and A. P. Lee, "Alternating droplet generation and controlled dynamic droplet fusion in microfluidic device for CdS nanoparticle synthesis." *Lab on a chip*, vol. 6, no. 2, pp. 174–8, Feb. 2006.

[57] B. Zheng, J. D. Tice, and R. F. Ismagilov, "Formation of droplets of alternating composition in microfluidic channels and applications to indexing of concentrations in droplet-based assays." *Analytical chemistry*, vol. 76, no. 17, pp. 4977–82, Sep. 2004.

[58] M. L. J. Steegmans, K. G. P. H. Schroën, and R. M. Boom, "Characterization of emulsification at flat microchannel Y junctions." *Langmuir : the ACS journal of surfaces and colloids*, vol. 25, no. 6, pp. 3396–401, Apr. 2009.

[59] S. L. Anna, N. Bontoux, and H. A. Stone, "Formation of dispersions using flow focusing in microchannels," *Applied Physics Letters*, vol. 82, no. 3, pp. 364–366, 2003.

[60] Q. Xu and M. Nakajima, "The generation of highly monodisperse droplets through the breakup of hydrodynamically focused microthread in a microfluidic device," *Applied Physics Letters*, vol. 85, no. 17, pp. 3726–3728, 2004.

[61] C. Zhou, P. Yue, and J. J. Feng, "Formation of simple and compound drops in microfluidic devices," *Physics of Fluids*, vol. 18, no. 9, p. 092105, 2006.

[62] P. Garstecki, H. Stone, and G. Whitesides, "Mechanism for Flow-Rate Controlled Breakup in Confined Geometries: A Route to Monodisperse Emulsions," *Physical Review Letters*, vol. 94, no. 16, pp. 1–4, Apr. 2005.

[63] S. L. Anna and H. C. Mayer, "Microscale tipstreaming in a microfluidic flow focusing device," *Physics of Fluids*, vol. 18, no. 12, p. 121512, 2006.

[64] C. L. Patrick, R. G. Robert, N. Zhihong, X. Shengqing, S. Minseok, and K. Eugenia, "Continuous Synthesis of Copolymer Particles in Microfluidic Reactors," *Macromolecules*, vol. 38, pp. 4536–4538, Jan. 2005.

[65] S. Takeuchi, P. Garstecki, D. B. Weibel, and G. M. Whitesides, "An Axisymmetric Flow-Focusing Microfluidic Device," *Advanced Materials*, vol. 17, no. 8, pp. 1067–1072, Apr. 2005.

[66] A. Utada, A. Fernandez-Nieves, J. Gordillo, and D. Weitz, "Absolute Instability of a Liquid Jet in a Coflowing Stream," *Physical Review Letters*, vol. 100, no. 1, p. 014502, Jan. 2008.

[67] J. V. Henry, W. J. Duncanson, H. C. Shum, D. A. Weitz, and G. T. Vladisavljevic, "Fabrication of Biodegradable Poly(Lactic Acid) Particles in Flow-Focusing Glass Capillary Devices," *Progress in Colloid and Polymer Science*, pp. 111–114, 2012.

[68] M. Abdelgawad, C. Wu, W.-Y. Chien, W. R. Geddie, M. a. S. Jewett, and Y. Sun, "A fast and simple method to fabricate circular microchannels in polydimethylsiloxane (PDMS)." *Lab on a chip*, vol. 11, no. 3, pp. 545–51, Feb. 2011.

[69] M. E. Wilson, N. Kota, Y. Kim, Y. Wang, D. B. Stolz, P. R. LeDuc, and O. B. Ozdoganlar, "Fabrication of circular microfluidic channels by combining mechanical micromilling and soft lithography." *Lab on a chip*, vol. 11, no. 8, pp. 1550–5, Apr. 2011.

[70] D. N. Breslauer, S. J. Muller, and L. P. Lee, "Generation of monodisperse silk microspheres prepared with microfluidics." *Biomacromolecules*, vol. 11, no. 3, pp. 643–7, Mar. 2010.

[71] P. B. Umbanhowar, V. Prasad, and D. a. Weitz, "Monodisperse Emulsion Generation via Drop Break Off in a Coflowing Stream," *Langmuir*, vol. 16, no. 2, pp. 347–351, Jan. 2000.

[72] K. Ferrara, R. Pollard, and M. Borden, "Ultrasound microbubble contrast agents: fundamentals and application to gene and drug delivery," *Biomedical Engineering*, vol. 9, 2007.

[73] S. Hernot and A. L. Klibanov, "Microbubbles in ultrasound-triggered drug and gene delivery," *Advanced drug delivery reviews*, vol. 60, no. 10, pp. 1153–1166, 2008.

[74] M. Lee, E. Y. Lee, D. Lee, and B. J. Park, "Stabilization and fabrication of microbubbles: applications for medical purposes and functional materials," *Soft matter*, vol. 11, no. 11, pp. 2067–2079, 2015.

[75] P. Deng, Y.-K. Lee, and P. Cheng, "Two-dimensional micro-bubble actuator array to enhance the efficiency of molecular beacon based dna micro-biosensors," *Biosensors and Bioelectronics*, vol. 21, no. 8, pp. 1443–1450, 2006.

[76] J. Rodríguez-Rodríguez, A. Sevilla, C. Martínez-Bazán, and J. M. Gordillo, "Generation of microbubbles with applications to industry and medicine," *Annual Review of Fluid Mechanics*, vol. 47, pp. 405–429, 2015.

[77] A. L. Klibanov, "Targeted delivery of gas-filled microspheres, contrast agents for ultrasound imaging," *Advanced drug delivery reviews*, vol. 37, no. 1, pp. 139–157, 1999.

[78] E. Quaia, "Microbubble ultrasound contrast agents: an update," *European radiology*, vol. 17, no. 8, pp. 1995–2008, 2007.

[79] E. C. Unger, T. P. McCREERY, R. H. SWEITZER, V. E. CALDWELL, and Y. WU, "Acoustically Active Lipospheres Containing Paclitaxel: A New Therapeutic Ultrasound Contrast Agent." *Investigative Radiology*, vol. 33, pp. 886–892, Dec. 1998.

[80] Z. Ying-Zheng, L. Hai-Dong, M. Xing-Guo, and H. Michael, "Preparation, characterization and in vivo observation of phospholipid-based gas-filled microbubbles containing hirudin," *Ultrasound in Medicine and Biology*, vol. 31, pp. 1237–1243, Apr. 2005.

[81] K. Bjerknes, K. Dyrstad, G. Smistad, and I. Agerkvist, "Preparation of polymeric microcapsules: formulation studies." *Drug development and industrial pharmacy*, vol. 26, no. 8, pp. 847–56, Aug. 2000.

[82] B. Jiang, C. Gao, and J. Shen, "Polylactide hollow spheres fabricated by interfacial polymerization in an oil-in-water emulsion system," *Colloid and Polymer Science*, vol. 284, no. 5, pp. 513–519, Dec. 2005.

[83] S. Khirani, P. Kunwapanitchakul, F. Augier, C. Guigui, P. Guiraud, and G. Hébrard, "Microbubble Generation through Porous Membrane under Aqueous or Organic Liquid Shear Flow," *Industrial & Engineering Chemistry Research*, vol. 51, no. 4, pp. 1997–2009, Feb. 2012.

[84] M. Kukizaki and M. Goto, "Spontaneous formation behavior of uniform-sized microbubbles from Shirasu porous glass (SPG) membranes in the absence of water-phase flow," *Colloids and Surfaces A: Physicochemical and Engineering Aspects*, vol. 296, no. 1-3, pp. 174–181, Mar. 2007.

[85] P. Garstecki, I. Gitlin, W. DiLuzio, G. M. Whitesides, E. Kumacheva, and H. A. Stone, "Formation of monodisperse bubbles in a microfluidic flow-focusing device," *Applied Physics Letters*, vol. 85, no. 13, pp. 2649–2651, 2004.

[86] J. Xu, S. Li, G. Chen, and G. Luo, "Formation of monodisperse microbubbles in a microfluidic device," *AIChE journal*, vol. 52, no. 6, pp. 2254–2259, 2006.

[87] E. Lorenceau, Y. Y. C. Sang, R. Hohler, and S. Cohen-Addad, "A high rate flow-focusing foam generator," *Physics of Fluids*, vol. 18, no. 9, p. 097103, 2006.

[88] a.G. Marín, F. Campo-Cortés, and J. Gordillo, "Generation of micron-sized drops and bubbles through viscous coflows," *Colloids and Surfaces A: Physicochemical and Engineering Aspects*, vol. 344, no. 1-3, pp. 2–7, Jul. 2009.

[89] J. M. Gordillo, Z. Cheng, A. M. Ganan-Calvo, M. Marquez, and D. A. Weitz, "A new device for the generation of microbubbles," *Physics of Fluids*, vol. 16, no. 8, pp. 2828–2834, 2004.

[90] J. Wan and H. A. Stone, "Microfluidic generation of a high volume fraction of bubbles in droplets," *Soft Matter*, vol. 6, no. 19, pp. 4677–4680, 2010.

[91] W. Jiandi and A. S. Howard, "Coated Gas Bubbles for the Continuous Synthesis of Hollow Inorganic Particles," *Langmuir*, vol. 28, pp. 37–41, Nov. 2012.

[92] J. Wan, A. Bick, M. Sullivan, and H. A. Stone, "Controllable Microfluidic Production of Microbubbles in Water-in-Oil Emulsions and the Formation of Porous Microparticles," *Advanced Materials*, vol. 20, no. 17, pp. 3314–3318, Sep. 2008.

[93] T. Fu, Y. Ma, D. Funfschilling, and H. Z. Li, "Bubble formation in non-Newtonian fluids in a microfluidic T-junction," *Chemical Engineering and Processing: Process Intensification*, vol. 50, no. 4, pp. 438–442, Apr. 2011.

[94] V. van Steijn, C. R. Kleijn, and M. T. Kreutzer, "Flows around Confined Bubbles and Their Importance in Triggering Pinch-Off," *Physical Review Letters*, vol. 103, no. 21, p. 214501, Nov. 2009.

[95] A. M. Gañán Calvo and J. M. Gordillo, "Perfectly Monodisperse Microbubbling by Capillary Flow Focusing," *Physical Review Letters*, vol. 87, no. 27, p. 274501, Dec. 2001.

[96] C. Chen, Y. Zhu, P. W. Leech, and R. Manasseh, "Production of monodispersed micron-sized bubbles at high rates in a microfluidic device," *Applied Physics Letters*, vol. 95, no. 14, p. 144101, 2009.

[97] J. M. Gordillo, A. Sevilla, and C. Martinez-Bazan, "Bubbling in a co-flow at high Reynolds numbers," *Physics of Fluids*, vol. 19, no. 7, p. 077102, 2007.

[98] G. T. Kovacs, K. Petersen, and M. Albin, "Peer reviewed: Silicon micromachining: Sensors to systems," *Analytical Chemistry*, vol. 68, no. 13, pp. 407A–412A, 1996.

[99] P. Clerc, L. Dellmann, F. Gretillat, M. Gretillat, P. Indermühle, S. Jeanneret, P. Luginbuhl, C. Marxer, T. Pfeffer, G. Racine *et al.*, "Advanced deep reactive ion etching: a versatile tool for microelectromechanical systems," *Journal of Micromechanics and Microengineering*, vol. 8, no. 4, p. 272, 1998.

[100] A. Dodge, K. Fluri, E. Verpoorte, and N. F. de Rooij, "Electrokinetically driven microfluidic chips with surface-modified chambers for heterogeneous immunoassays," *Analytical chemistry*, vol. 73, no. 14, pp. 3400–3409, 2001.

[101] J. Lichtenberg, E. Verpoorte, and N. F. de Rooij, "Sample preconcentration by field amplification stacking for microchip-based capillary electrophoresis," *Electrophoresis*, vol. 22, no. 2, pp. 258–271, 2001.

[102] G. S. Fiorini and D. T. Chiu, "Disposable microfluidic devices: fabrication, function, and application," *BioTechniques*, vol. 38, no. 3, pp. 429–446, 2005.

[103] Y. Xia and G. M. Whitesides, "Soft lithography," *Annual review of materials science*, vol. 28, no. 1, pp. 153–184, 1998.

[104] H. Becker and U. Heim, "Hot embossing as a method for the fabrication of polymer high aspect ratio structures," *Sensors and Actuators A: Physical*, vol. 83, no. 1, pp. 130–135, 2000.

[105] D. Pugmire, E. Waddell, R. Haasch, M. Tarlov, and L. E. Locascio, "Surface characterization of laser-ablated polymers used for microfluidics," *Analytical chemistry*, vol. 74, no. 4, pp. 871–878, 2002.

[106] D. Snakenborg, H. Klank, and J. P. Kutter, "Microstructure fabrication with a co2 laser system," *Journal of Micromechanics and microengineering*, vol. 14, no. 2, p. 182, 2003.

[107] F. P. Melchels, J. Feijen, and D. W. Grijpma, "A review on stereolithography and its applications in biomedical engineering," *Biomaterials*, vol. 31, no. 24, pp. 6121–6130, 2010.

[108] J. Korpela, A. Kokkari, H. Korhonen, M. Malin, T. Närhi, and J. Seppälä, "Biodegradable and bioactive porous scaffold structures prepared using fused deposition modeling," *Journal of Biomedical Materials Research Part B: Applied Biomaterials*, vol. 101, no. 4, pp. 610–619, 2013.

[109] C. M. B. Ho, S. H. Ng, K. H. H. Li, and Y.-J. Yoon, "3d printed microfluidics for biological applications," *Lab on a Chip*, vol. 15, no. 18, pp. 3627–3637, 2015.

[110] B. Dhariwala, E. Hunt, and T. Boland, "Rapid prototyping of tissue-engineering constructs, using photopolymerizable hydrogels and stereolithography," *Tissue engineering*, vol. 10, no. 9-10, pp. 1316–1322, 2004.

[111] Y. Lu and S. Chen, "Direct write of microlens array using digital projection photopolymerization," *Applied Physics Letters*, vol. 92, no. 4, p. 041109, 2008.

[112] R. Singh, "Process capability study of polyjet printing for plastic components," *Journal of mechanical science and technology*, vol. 25, no. 4, pp. 1011–1015, 2011.

[113] N. Bhattacharjee, A. Urrios, S. Kang, and A. Folch, "The upcoming 3d-printing revolution in microfluidics," *Lab. Chip*, 2016.

[114] T. Nisisako, S. Okushima, and T. Torii, "Controlled formulation of monodisperse double emulsions in a multiple-phase microfluidic system," *Soft Matter*, vol. 1, no. 1, pp. 23–27, 2005.

[115] S. Okushima, T. Nisisako, T. Torii, and T. Higuchi, "Controlled production of monodisperse double emulsions by two-step droplet breakup in microfluidic devices." *Langmuir : the ACS journal of surfaces and colloids*, vol. 20, no. 23, pp. 9905–8, Nov. 2004.

[116] Z. Nie, S. Xu, M. Seo, P. C. Lewis, and E. Kumacheva, "Polymer particles with various shapes and morphologies produced in continuous microfluidic reactors." *Journal of the American Chemical Society*, vol. 127, no. 22, pp. 8058–63, Jun. 2005.

[117] M. Seo, C. Paquet, Z. Nie, S. Xu, and E. Kumacheva, "Microfluidic consecutive flow-focusing droplet generators," *Soft Matter*, vol. 3, no. 8, pp. 986–992, 2007.

[118] A. A. R and W. D. A, "High-Order Multiple Emulsions Formed in Poly(dimethylsiloxane) Microfluidics," *Small*, vol. 18, pp. 2030–2032, May 2009.

[119] A. R. Abate, J. Thiele, and D. A. Weitz, "One-step formation of multiple emulsions in microfluidics." *Lab on a chip*, vol. 11, no. 2, pp. 253–8, Jan. 2011.

[120] H. C. Shum, A. Bandyopadhyay, S. Bose, and D. A. Weitz, "Double Emulsion Droplets as Microreactors for Synthesis of Mesoporous Hydroxyapatite," *Chemistry of Materials*, vol. 21, no. 22, pp. 5548–5555, Nov. 2009.

[121] H. C. Shum, D. Lee, I. Yoon, T. Kodger, and D. A. Weitz, "Double emulsion templated monodisperse phospholipid vesicles." *Langmuir : the ACS journal of surfaces and colloids*, vol. 24, no. 15, pp. 7651–3, Aug. 2008.

[122] L. Daeyeon and A. W. David, "Double Emulsion-Templated Nanoparticle Colloidosomes with Selective Permeability," *Advanced Material*, vol. 20, pp. 3498–3053, Sep. 2008.

[123] K. Jin-Woong, S. U. Andrew, F.-N. Alberto, H. Zhibing, and A. David, "Fabrication of Monodisperse Gel Shells and Functional Microgels in Microfluidic Devices," *Angewandte Chemie (International ed. in English)*, vol. 46, pp. 1819–1822, Apr. 2007.

[124] W. Wang, R. Xie, X.-J. Ju, T. Luo, L. Liu, D. A. Weitz, and L.-Y. Chu, "Controllable microfluidic production of multicomponent multiple emulsions." *Lab on a chip*, vol. 11, no. 9, pp. 1587–92, May 2011.

[125] C. Liang-Yin, S. U. Andrew, K. S. Rhutesh, K. Jin-Woong, and A. W. David, "Controllable Monodisperse Multiple Emulsions," *Angewandte Chemie*, vol. 119, pp. 9128–9132, May 2007.

[126] B. J. Sun, H. C. Shum, C. Holtze, and D. A. Weitz, "Microfluidic melt emulsification for encapsulation and release of actives." *ACS applied materials & interfaces*, vol. 2, no. 12, pp. 3411–6, Dec. 2010.

[127] H. C. Shum, Y.-j. Zhao, S.-H. Kim, and D. A. Weitz, "Multicompartment polymersomes from double emulsions." *Angewandte Chemie (International ed. in English)*, vol. 50, no. 7, pp. 1648–51, Feb. 2011.

[128] I. U. Vakarelski, N. A. Patankar, J. O. Marston, D. Y. Chan, and S. T. Thoroddsen, "Stabilization of leidenfrost vapour layer by textured superhydrophobic surfaces," *Nature*, vol. 489, no. 7415, pp. 274–277, 2012.

[129] T. Cubaud and T. G. Mason, "Capillary threads and viscous droplets in square microchannels," *Physics of Fluids*, vol. 20, no. 5, p. 053302, 2008.

[130] R. M. Erb, D. Obrist, P. W. Chen, J. Studer, and A. R. Studart, "Predicting sizes of droplets made by microfluidic flow-induced dripping," *Soft Matter*, vol. 7, no. 19, pp. 8757–8761, 2011.

[131] S. Tomotika, "On the instability of a cylindrical thread of a viscous liquid surrounded by another viscous fluid," in *Proc. R. Soc. London, Ser. A*, vol. 150, no. 870, 1935, pp. 322–337.

[132] A. S. Utada, A. Fernandez-Nieves, H. A. Stone, and D. A. Weitz, "Dripping to jetting transitions in coflowing liquid streams," *Physical review letters*, vol. 99, no. 9, p. 094502, 2007.

[133] T. Cubaud and T. G. Mason, "Capillary threads and viscous droplets in square microchannels," *Physics of Fluids (1994-present)*, vol. 20, no. 5, p. 053302, 2008.

[134] J.-H. Xu, R. Chen, Y.-D. Wang, and G.-S. Luo, "Controllable gas/liquid/liquid double emulsions in a dual-coaxial microfluidic device," *Lab on a Chip*, vol. 12, no. 11, pp. 2029–2036, 2012.

[135] J. R. Lindner, "Microbubbles in medical imaging: current applications and future directions," *Nature Reviews Drug Discovery*, vol. 3, no. 6, pp. 527–533, 2004.

[136] K. Hettiarachchi, E. Talu, M. L. Longo, P. A. Dayton, and A. P. Lee, "On-chip generation of microbubbles as a practical technology for manufacturing contrast agents for ultrasonic imaging," *Lab Chip*, vol. 7, no. 4, pp. 463–468, 2007.

[137] P. A. Grayburn, "Current and future contrast agents," *Echocardiography*, vol. 19, no. 3, pp. 259–265, 2002.

[138] F. S. Villanueva, R. J. Jankowski, S. Klibanov, M. L. Pina, S. M. Alber, S. C. Watkins, G. H. Brandenburger, and W. R. Wagner, "Microbubbles targeted to intercellular adhesion molecule-1 bind to activated coronary artery endothelial cells," *Circulation*, vol. 98, no. 1, pp. 1–5, 1998.

[139] T. R. Porter, F. Xie, D. Knapp, P. Iversen, L. a. Marky, J. M. Tsutsui, S. Maiti, J. Lof, S. J. Radio, and N. Kipshidze, "Targeted vascular delivery of antisense molecules using intravenous microbubbles." *Cardiovascular revascularization medicine : including molecular interventions*, vol. 7, no. 1, pp. 25–33, 2006.

[140] E. Talu, K. Hettiarachchi, R. L. Powell, A. P. Lee, P. a. Dayton, and M. L. Longo, "Maintaining monodispersity in a microbubble population formed by flow-focusing." *Langmuir : the ACS journal of surfaces and colloids*, vol. 24, no. 5, pp. 1745–9, Mar. 2008.

[141] M. Seo, I. Gorelikov, R. Williams, and N. Matsuura, "Microfluidic assembly of monodisperse, nanoparticle-incorporated perfluorocarbon microbubbles for medical imaging and therapy." *Langmuir : the ACS journal of surfaces and colloids*, vol. 26, no. 17, pp. 13 855–60, Sep. 2010.

[142] S. a. Peyman, R. H. Abou-Saleh, J. R. McLaughlan, N. Ingram, B. R. G. Johnson, K. Critchley, S. Freear, J. A. Evans, A. F. Markham, P. L. Coletta, and S. D. Evans, "Expanding 3D geometry for enhanced on-chip microbubble production and single step formation of liposome modified microbubbles." *Lab on a chip*, vol. 12, no. 21, pp. 4544–52, Nov. 2012.

[143] E. Castro-Hernández, W. Van Hoeve, D. Lohse, and J. M. Gordillo, "Microbubble generation in a co-flow device operated in a new regime." *Lab on a chip*, vol. 11, no. 12, pp. 2023–9, Jun. 2011.

[144] J. I. Park, Z. Nie, A. Kumachev, and E. Kumacheva, "A microfluidic route to small CO2 microbubbles with narrow size distribution," *Soft Matter*, vol. 6, no. 3, p. 630, 2010.

[145] J. I. Park, E. Tumarkin, and E. Kumacheva, "Small, stable, and monodispersed bubbles encapsulated with biopolymers." *Macromolecular rapid communications*, vol. 31, no. 2, pp. 222–7, Jan. 2010.

[146] F. Campo-Cortés, G. Riboux, and J. M. Gordillo, "The effect of contact line pinning favors the mass production of monodisperse microbubbles," *Microfluidics and Nanofluidics*, vol. 20, no. 1, pp. 1–8, 2016.

[147] U. Farook, E. Stride, M. J. Edirisinghe, and R. Moaleji, "Microbubbling by co-axial electrohydrodynamic atomization." *Medical & biological engineering & computing*, vol. 45, no. 8, pp. 781–9, Aug. 2007.

[148] U. Farook, H. B. Zhang, M. J. Edirisinghe, E. Stride, and N. Saffari, "Preparation of microbubble suspensions by co-axial electrohydrodynamic atomization." *Medical engineering & physics*, vol. 29, no. 7, pp. 749–54, Sep. 2007.

[149] A. M. Ganán-Calvo and J. M. Gordillo, "Perfectly monodisperse microbubbling by capillary flow focusing," *Physical review letters*, vol. 87, no. 27, p. 274501, 2001.

[150] E. Q. Li, J. M. Zhang, and S. T. Thoroddsen, "Simple and inexpensive microfluidic devices for the generation of monodisperse multiple emulsions," *Journal of Micromechanics and Microengineering*, vol. 24, no. 1, p. 015019, 2013.

[151] A. M. Ganán-Calvo, "Perfectly monodisperse microbubbling by capillary flow focusing: An alternate physical description and universal scaling," *Physical Review E*, vol. 69, no. 2, p. 027301, 2004.

[152] A. Utada, A. Fernandez-Nieves, H. Stone, and D. Weitz, "Dripping to Jetting Transitions in Coflowing Liquid Streams," *Physical Review Letters*, vol. 99, no. 9, pp. 1–4, Aug. 2007.

[153] A. Utada, A. Fernandez-Nieves, J. Gordillo, and D. Weitz, "Absolute Instability of a Liquid Jet in a Coflowing Stream," *Physical Review Letters*, vol. 100, no. 1, p. 014502, Jan. 2008.

[154] J. M. Gordillo, A. M. Gañán-Calvo, and M. Pérez-Saborid, "Monodisperse microbubbling: Absolute instabilities in coflowing gas–liquid jets," *Physics of Fluids (1994-present)*, vol. 13, no. 12, pp. 3839–3842, 2001.

[155] A. M. Gañán-Calvo, M. A. Herrada, and P. Garstecki, "Bubbling in unbounded coflowing liquids," *Physical review letters*, vol. 96, no. 12, p. 124504, 2006.

[156] A. Sevilla, J. Gordillo, and C. Martínez-Bazán, "Transition from bubbling to jetting in a coaxial air–water jet," *Physics of Fluids (1994-present)*, vol. 17, no. 1, p. 018105, 2005.

[157] K. Sun, T.-S. Wei, B. Y. Ahn, J. Y. Seo, S. J. Dillon, and J. A. Lewis, "3d printing of interdigitated li-ion microbattery architectures," *Adv. Mater.*, vol. 25, no. 33, pp. 4539–4543, 2013.

[158] J. N. Hanson Shepherd, S. T. Parker, R. F. Shepherd, M. U. Gillette, J. A. Lewis, and R. G. Nuzzo, "3d microperiodic hydrogel scaffolds for robust neuronal cultures," *Adv. Funct. Mater.*, vol. 21, no. 1, pp. 47–54, 2011.

[159] D. Therriault, S. R. White, and J. A. Lewis, "Chaotic mixing in three-dimensional microvascular networks fabricated by direct-write assembly," *Nat. Mater.*, vol. 2, no. 4, pp. 265–271, 2003.

[160] M. D. Symes, P. J. Kitson, J. Yan, C. J. Richmond, G. J. Cooper, R. W. Bowman, T. Vilbrandt, and L. Cronin, "Integrated 3d-printed reactionware for chemical synthesis and analysis," *Nat. Chem.*, vol. 4, no. 5, pp. 349–354, 2012.

[161] E. Li, Q. Xu, J. Sun, J. Fuh, Y. Wong, and S. Thoroddsen, "Design and fabrication of a pet/ptfe-based piezoelectric squeeze mode drop-on-demand inkjet printhead with interchangeable nozzle," *Sens. Actuators A*, vol. 163, no. 1, pp. 315–322, 2010.

[162] P. J. Kitson, M. H. Rosnes, V. Sans, V. Dragone, and L. Cronin, "Configurable 3d-printed millifluidic and microfluidic lab on a chipreactionware devices," *Lab. Chip*, vol. 12, no. 18, pp. 3267–3271, 2012.

[163] K. G. Lee, K. J. Park, S. Seok, S. Shin, J. Y. Park, Y. S. Heo, S. J. Lee, T. J. Lee *et al.*, "3d printed modules for integrated microfluidic devices," *RSC Advances*, vol. 4, no. 62, pp. 32 876–32 880, 2014.

[164] A. K. Au, W. Lee, and A. Folch, "Mail-order microfluidics: evaluation of stereolithography for the production of microfluidic devices," *Lab. Chip*, vol. 14, no. 7, pp. 1294–1301, 2014.

[165] G. Comina, A. Suska, and D. Filippini, "Low cost lab-on-a-chip prototyping with a consumer grade 3d printer," *Lab. Chip*, vol. 14, no. 16, pp. 2978–2982, 2014.

[166] W. Lee, D. Kwon, W. Choi, G. Y. Jung, and S. Jeon, "3d-printed microfluidic device for the detection of pathogenic bacteria using size-based separation in helical channel with trapezoid cross-section," *Sci. Rep.*, vol. 5, p. 7717, 2015.

[167] L. Donvito, L. Galluccio, A. Lombardo, G. Morabito, A. Nicolosi, and M. Reno, "Experimental validation of a simple, low-cost, t-junction droplet generator fabricated through 3d printing," *J. Micromech. Microeng.*, vol. 25, no. 3, p. 035013, 2015.

[168] A. I. Shallan, P. Smejkal, M. Corban, R. M. Guijt, and M. C. Breadmore, "Cost-effective three-dimensional printing of visibly transparent microchips within minutes," *Analytical chemistry*, vol. 86, no. 6, pp. 3124–3130, 2014.

[169] K. C. Bhargava, B. Thompson, and N. Malmstadt, "Discrete elements for 3d microfluidics," *Proc. Natl. Acad. Sci. USA*, vol. 111, no. 42, pp. 15 013–15 018, 2014.

[170] A. Rotem, A. R. Abate, A. S. Utada, V. Van Steijn, and D. A. Weitz, "Drop formation in non-planar microfluidic devices," *Lab. Chip*, vol. 12, no. 21, pp. 4263–4268, 2012.

[171] B. Wendel, D. Rietzel, F. Kühnlein, R. Feulner, G. Hülder, and E. Schmachtenberg, "Additive processing of polymers," *Macromol. Mater. Eng.*, vol. 293, no. 10, pp. 799–809, 2008.

[172] A. S. Utada, A. Fernandez-Nieves, H. A. Stone, and D. A. Weitz, "Dripping to jetting transitions in coflowing liquid streams," *Phys. Rev. Lett.*, vol. 99, no. 9, p. 094502, 2007.

[173] T. Cubaud and T. G. Mason, "Capillary threads and viscous droplets in square microchannels," *Phys. Fluids*, vol. 20, no. 5, p. 053302, 2008.

[174] J.-T. Wang, J. Wang, and J.-J. Han, "Fabrication of advanced particles and particle-based materials assisted by droplet-based microfluidics," *Small*, vol. 7, no. 13, pp. 1728–1754, 2011.

[175] S. L. Anna, "Droplets and bubbles in microfluidic devices," *Annual Review of Fluid Mechanics*, vol. 48, pp. 285–309, 2016.

[176] B. Wendel, D. Rietzel, F. Kühnlein, R. Feulner, G. Hülder, and E. Schmachtenberg, "Additive processing of polymers," *Macromolecular materials and engineering*, vol. 293, no. 10, pp. 799–809, 2008.

[177] M. De Menech, P. Garstecki, F. Jousse, and H. Stone, "Transition from squeezing to dripping in a microfluidic t-shaped junction," *journal of fluid mechanics*, vol. 595, pp. 141–161, 2008.

[178] P. Garstecki, M. J. Fuerstman, H. A. Stone, and G. M. Whitesides, "Formation of droplets and bubbles in a microfluidic t-junctionscaling and mechanism of break-up," *Lab on a Chip*, vol. 6, no. 3, pp. 437–446, 2006.

[179] K. Wang, Y. Lu, J. Xu, J. Tan, and G. Luo, "Generation of micromonodispersed droplets and bubbles in the capillary embedded t-junction microfluidic devices," *AIChE journal*, vol. 57, no. 2, pp. 299–306, 2011.

[180] G. F. Christopher, N. N. Noharuddin, J. A. Taylor, and S. L. Anna, "Experimental observations of the squeezing-to-dripping transition in t-shaped microfluidic junctions," *Physical Review E*, vol. 78, no. 3, p. 036317, 2008.

[181] A. J. deMello, "Control and detection of chemical reactions in microfluidic systems," *Nature*, vol. 442, no. 7101, pp. 394–402, Jul. 2006.

[182] D.-K. Kang, X. Gong, S. Cho, J.-y. Kim, J. B. Edel, S.-I. Chang, J. Choo, and A. J. deMello, "3d droplet microfluidic systems for high-throughput biological experimentation," *Analytical chemistry*, vol. 87, no. 21, pp. 10 770–10 778, 2015.

[183] N. Damean, L. F. Olguin, F. Hollfelder, C. Abell, and W. T. Huck, "Simultaneous measurement of reactions in microdroplets filled by concentration gradients," *Lab on a Chip*, vol. 9, no. 12, pp. 1707–1713, 2009.

[184] P. Eribol, A. Uguz, and K. Ulgen, "Screening applications in drug discovery based on microfluidic technology," *Biomicrofluidics*, vol. 10, no. 1, p. 011502, 2016.

[185] I. Shestopalov, J. D. Tice, and R. F. Ismagilov, "Multi-step synthesis of nanoparticles performed on millisecond time scale in a microfluidic droplet-based system," *Lab on a Chip*, vol. 4, no. 4, pp. 316–321, 2004.

[186] H. Gu, M. H. Duits, and F. Mugele, "Droplets formation and merging in two-phase flow microfluidics," *International journal of molecular sciences*, vol. 12, no. 4, pp. 2572–2597, 2011.